Spring 5-12-2022

Copolymer microphase separation, properties, and applications

Daniel Weller

COPOLYMER MICROPHASE SEPARATION, PROPERTIES, AND APPLICATIONS

by

Daniel Weller

A Dissertation
Submitted to the Graduate School,
the College of Arts and Sciences
and the School of Polymer Science and Engineering
at The University of Southern Mississippi
in Partial Fulfillment of the Requirements
for the Degree of Doctor of Philosophy

Approved by:

Dr. Xiaodan Gu, Committee Chair
Dr. Derek L. Patton
Dr. Sarah E. Morgan
Dr. Sergei Nazarenko
Dr. Jeffery S. Wiggins

May 2022

Published by the Graduate School

ABSTRACT

Copolymers represent a broad, but critically important class of materials. Often having properties superior to either of its constituents, copolymers are used in virtually all industries including automotive, aerospace, coatings, packaging, and cosmetics. Certain copolymers microphase separate to form nanosized domains that improve the physical properties of the copolymer. The polymer community already has a thorough understanding of how phase separation occurs, but the commercialization of phase separating copolymers lags significantly behind academia. Many of the copolymers that exist that have been undercharacterized and underutilized. This dissertation examines two such polymers. The first, a hard polystyrene material with soft nanodomains. The second, a soft polypentenamer rubber with hard nanodomains. These copolymers have very different physical properties, and thus very different intended applications. The common thread connecting the works in this dissertation is an effort to harness microphase separation to enable new applications.

The first chapter gives an overview of copolymer architectures, properties, and their applications. Special attention is given to linear diblock copolymers as well as thermoplastic elastomers as these are most relevant to Chapters II-III and IV-V respectively. Chapter II explores the use of self-assembling diblock copolymers for use as ultrafiltration membranes. In this chapter a new membrane manufacturing process is described that quickly turns dense block copolymer films into porous membranes. Chapter III expands on this work by demonstrating a novel BCP annealing method that reduces domain size variation and is roll-to-roll printing compatible.

In Chapters IV and V, we shift gears from studying glassy diblock copolymers, to soft multiblock elastomers. Chapter IV explores the effect of incorporating a glassy monomer into a crosslinked elastomer in a search for a natural rubber replacement. It was found that modest glassy block incorporation could greatly increase tensile strength. Chapter V then clarifies the strengthening mechanism observed in Chapter IV by looking at the effect of the glassy monomer before chemically crosslinking the elastomer. This work showed that phase separation of the glassy domains created physical crosslinks demonstrating thermoplastic elastic behavior.

Finally, in Chapter VI some general conclusions about the research are recapped and put into a broader perspective. Suggestions for future work are then provided that would further the knowledge in both of the research directions. I hope you enjoy.

ACKNOWLEDGMENTS

First and foremost, I must thank my advisor Dr. Xiaodan Gu for his contributions to this work but also to my development as a scientist. Without his unyielding optimism and pinpoint focus, the work I present herein would have not been possible. I have grown tremendously in these areas under his mentorship and for that I am eternally grateful.

Next let me thank all of my Gu group research groupmates. Dr. Song Zhang, Luke Galuska, Zhiqiang Cao, Guorong Ma, Yunfei Wang, Dr. Zhiyuan Qian, Sonia Stanciu, and Kundu Thapa. Without your company it would have been a lonely, and far less successful endeavor.

I had the privilege of mentoring three undergrads I would like to acknowledge: Zach Rodgers, Garrett Stringer, and Sophie Aracri. They did a lot of the gritty, undesirable, work that I was thankful to avoid.

A huge thanks goes to Exxon Mobil for not only financing part of my work, but also for contributing time, materials, and data that greatly accelerated my project. I want to especially thank Dr. Carlos Lopez-Barron. He was my primary collaborator at Exxon and acted as a second mentor. Under his guidance I learned a great deal about elastomers. I would like to thank include Joe Throckmorton, who taught me how to run the in situ WAXS experiments and Alex Zabula who synthesized many of the elastomeric polymers we tested.

I also want to thank my USM collaborators on the Exxon project. Dr. Sumant Dwivedi and Kyle Mehringer for your synthetic work, Dr. Rahul Shankar for your characterization work, and Dr. Sarah Morgan / Dr. Robson Storey for your guidance.

Thank you to my collaborators on the membrane project. Dr. Kunlun Hong, from Oak Ridge National Lab, for providing us with ample amounts of block copolymer. Dr. Mohamad Hassan from Qatar University for helping us find funding. And to my collaborators from the University of Southern Mississippi Dr. Sergei Nazarenko and his student Mustafa Zagho.

Thank you, Dr. James Rawlins, for providing me access to your SEM. The instrument was vital to my research. Also thank you to Michael Blanton who always made sure it was running smoothly and was happy to help when it wasn't.

I would also like to thank the entire staff of the School of Polymer Science and Engineering. Your friendly, helpful, and welcoming demeanor made the experience so much more enjoyable.

Finally, I appreciate the funding support from the National Science Foundation, Army Corps of Engineering, and Qatar National Science Foundation.

DEDICATION

To my mom Susie,

for never giving up on me, even when I was difficult

To my dad Mark,

for teaching me to take pride in my work

To my sister Katie,

for inspiring me to set audacious goals, and achieve them

TABLE OF CONTENTS

LIST OF TABLES

LIST OF ILLUSTRATIONS

LIST OF ABBREVIATIONS

$A_{f\,am}$	amorphous alignment factor
$A_{f\,\chi}$	crystalline alignment factor
AuNP	gold nanoparticle
ABS	acrylonitrile butadiene styrene
AFM	atomic force microscopy
BCP	block copolymer
BSA	bovine serum albumin
CDCl3	deuterated chloroform
CN	chloronaphthalene
CP	cyclopentene
Đ	dispersity
DBPth	dibutyl phthalate
DCPD	dicyclopentadiene
DFS	dynamic frequency sweep
DMTA	dynamic mechanical thermal analysis
DSC	differential scanning calorimetry
FWHM	full width at half maximum
G*	complex modulus
g’	branching index
G’	storage modulus
G’’	loss modulus

GISAXS	grazing-incidence small-angle X-ray scattering
GPC	gel permeation chromatography
HBP	high boiling point
HDPE	high density polyethylene
LCB	long-chain branched
LDPE	low density polyethylene
LS	light scattering
M_n	number average molecular weight
MN	methylnaphthalene
MW	molecular weight (general)
M_w	weight average molecular weight
N	degree of polymerization
NIPS	nonsolvent-induced phase separation
NMR	nuclear magnetic resonance
NR	natural rubber
NVASA	non-volatile additive solvent annealing
PASA	plasticizer additive solvent annealing
PE	polyethylene
PES	polyethersulfone
PET	polyethylene terephthalate
phr	parts per hundred rubber
PID	proportional–integral–derivative

PPR	polypentenamer rubber
PS-b-P2VP	polystyrene-block-poly(2-vinylpyridine)
PS-b-PEO	polystyrene-block-polyethylene oxide
PTFE	polytetrafluoroethylene
ROMP	ring-opening metathesis polymerization
SAXS	small-angle X-ray scattering
SBS	styrene butadiene styrene
SDD	sample to detector distance
SDZ	shear deformation zone
SEM	scanning electron microscope
SIC	strain induced crystallization
SNIPS	self-assembly and non-solvent induced phase separation
SR	swell ratio
SVA	solvent vapor annealing
T_c	crystallization temperature
T_g	glass transition temperature
T_m	melting temperature
TPE	thermoplastic elastomer
V_f	volume fraction
vGP	van Gurp-Palmen
WAXS	wide-angle X-ray scattering
χ	Flory-Huggins interaction parameter (chi)

CHAPTER I – COPOLYMER CHEMISTRY, PHYSICS, and APPLICATIONS

1.1 Copolymer Overview

Copolymers are polymers synthesized from two or more distinct monomer units. Often, copolymers have properties intermediate of the monomers that make them up. However, certain copolymers have better properties than the homopolymers they are composed of. Typically, these synergistic effects are observed in copolymers that microphase separate. This dissertation explores different microphase separating copolymer systems by altering their morphology, characterizing their behavior, and applying them to real-world applications.

The first recorded copolymerization was performed over 100 years ago in 1914.[1] Since then, countless combinations of monomers have been polymerized in hopes of producing materials with unique and useful properties. At first, copolymerization was primarily used to tune the thermal properties of the material. It was later discovered that copolymers could also affect the materials tensile strength, modulus, and elasticity depending on the structures the copolymers form when they aggregate.[2]

One of the most successful copolymers to date is acrylonitrile butadiene styrene (ABS), named after the three monomers used to polymerize it. ABS is preferred in many situations because it uniquely rigid *and* impact resistant. The unique mechanical properties of ABS can be explained by its phase separated morphology (Figure 1.1). The material is primarily made up of rigid components (styrene and acrylonitrile) that contain dispersions of soft rubbery material (butadiene).[3] Cracks propagate quickly in rigid materials, but in ABS the small rubbery domains arrest cracks, greatly increasing the

material's strength and toughness. It is believed that the soft domains strengthen glassy matrices by two methods. Firstly, they create a tortuous path for the crack to propagate, and secondly, they initiate crazes which dissipate energy.[4] Copolymer morphology greatly impacts performance, and therefore deserves significant attention. Many factors influence the phase separated morphology of a copolymer, but none more than chain architecture.

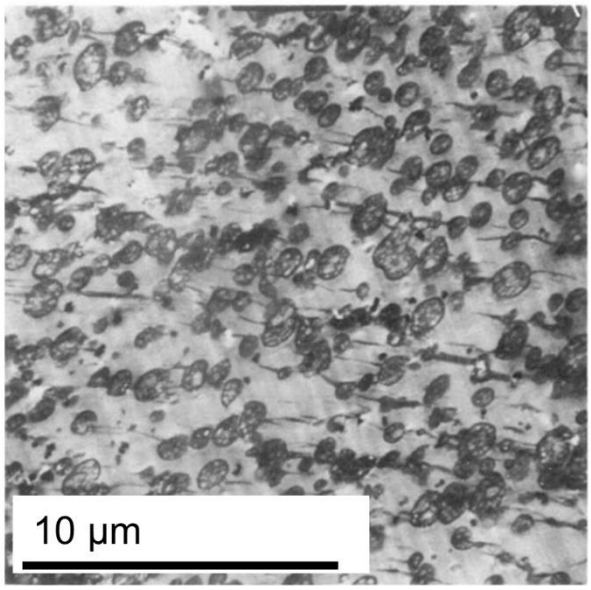

Figure 1.1 *ABS microphase separation*

SEM image of ABS after tensile strain. Dark regions of soft butadiene phase stop crack propagation. Figure adopted from Ref. [3].

Five major copolymer architectures exist: Statistical, alternating, block, gradient, and graft.[5] The basic structure of each architecture can be seen in Figure 1.2. Copolymers composed of the same monomers A and B, can form any one of these structures under various polymerization conditions. The resulting polymers may have wildly different thermal and mechanical properties depending on which architecture is achieved despite being composed of the same monomers.

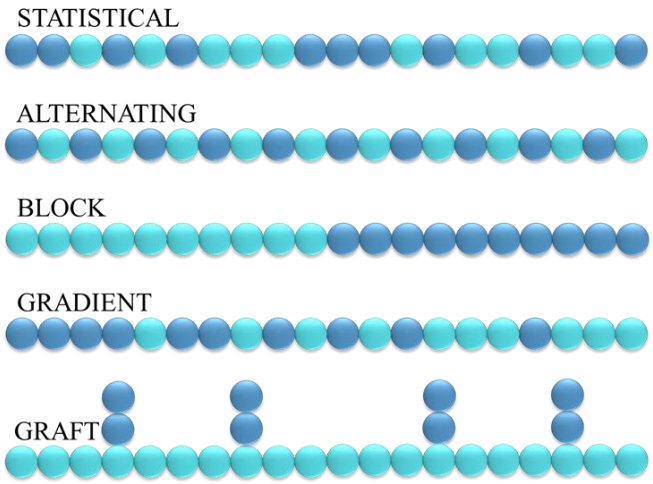

Figure 1.2 *Common copolymer architectures*

The simplest copolymer is the statistical copolymer. Statistical copolymers, often referred to inaccurately as "random" copolymers, are copolymers whose structure was determined by the reaction kinetics of each monomer to the growing chain. Statistical polymerization rates are described by the Mayo-Lewis equation (Equation 1.1) where relative monomer addition rates are shown as a function of monomer concentration ($[M_x]$) and relative reaction rates r_x. In this case $r_1 = \frac{k_{AA}}{k_{AB}}$ and $r_2 = \frac{k_{BA}}{k_{BB}}$ where k_{AA} represents the rate monomer A adds to a growing chain whose propagating unit is also monomer A.

$$\frac{d[M_A]}{d[M_B]} = \frac{[M_A](r_1[M_A] + [M_B])}{[M_B]([M_A] + r_2[M_B])} \tag{1.1}$$

Alternating copolymers are a specific kind of statistical copolymer where the reaction of AB is much faster than either AA or BB such that the polymer forms an alternating pattern. Because of its step-growth nature, polyethylene terephthalate (PET) is an example of a perfectly alternating copolymer of ethylene glycol and terephthalic acid. Like ABS, PET is also composed of hard and soft monomers, but PET does not have phase separated rubbery domains. PET has a homogenous morphology because the alternating structure of soft and hard monomers are in such intimate contact that phase separation cannot occur. PET is so homogenous that it only has one glass transition temperature (T_g) and one melting temperature (T_m) that is an intermediate between either homopolymer its monomers would produce.

Block copolymers (BCPs) are distinguished from other copolymers by having long runs of a single monomer. The first block copolymers were made following the discovery of anionic polymerization which allowed the sequential addition of monomer to "living" polymer chains.[6,7] With this technique blocks are built one block at a time. A two-step synthesis is used to form diblock copolymers, a three-step synthesis to form triblock and so on. This strategy creates large, well-defined blocks, but the multiple reaction and purification steps make them more difficult and expensive to synthesize. Multiblock copolymers are composed of many smaller blocks made in a one-step reaction. Multiblock polymers contain between 10-100 blocks per chain, and have an ill-defined structure making them difficult to study, but due to simple synthesis remain commercially relevant.[8] Various strategies are used to create a multiblock structure, but one common method is the copolymerization of oligomers and monomer.

The properties of BCPs are superior to those of random copolymers because they are able to phase separate and act as a composite material.[2] How effective phase separation occurs is dependent on the nature of the BCP including its composition, block length, number of blocks, and sequence of blocks.[2]

1.2 Linear Diblock Copolymers

Linear diblock copolymers have been widely studied and provide a useful understanding of the physics that govern microphase separation.[9] BCPs with a thermodynamic drive to phase separate, cannot macroscopically phase separate like oil and water because the two domains are covalent bound together. Instead, these polymers microphase separate, forming nanometer sized domains that minimize the free energy of the system. The structure that is most thermodynamically stable changes depending on the degree of polymerization (N), volume fraction (V_f), and the Flory-Huggins interaction parameter (χ) between the two monomers. The longer the block length, and the larger the χ value between the blocks, the more favorable it is for the system to phase separate. Studies have shown that when $\chi N < 10.5$ the enthalpic benefit of phase separation is not large enough to offset the loss of configurational entropy and the system will remain disordered. When $\chi N > 10.5$ however the entropic penalty for demixing is overcome and phase separation will occur.[10] Phase separated BCPs assemble into structures that minimize the contact between blocks. Their preferred geometry changes with increasing V_f between spherical, cylindrical, gyroidal or lamellar, as seen in Figure 1.3.[11]

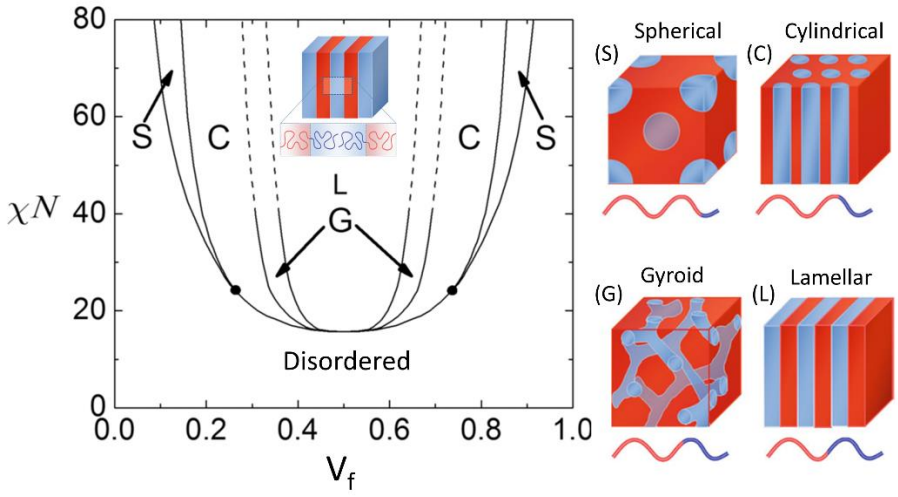

Figure 1.3 *Phase diagram of linear diblock copolymers*

Self-assembly structures accessible to linear diblock copolymers. Figure adopted from Ref. [11].

Before realizing their pristine, highly ordered structure, BCPs usually must undergo an annealing procedure. While polymer characteristics such as χ, N, and V_f, determine the thermodynamically preferred structure, often times the polymer is kinetically trapped in a nonequilibrium state. Annealing gives the chains enough mobility so they can rearrange themselves to reduce the free energy in the system. Two major annealing strategies exist. Thermal annealing, which raises the temperature of the material above its T_g. And solvent annealing, which lowers the T_g of the material below room temperature. Solvent annealing is much faster taking just 10's of minutes while thermal annealing takes hours or even days. Thermal annealing however is simpler because heating does not significantly change the V_f of the blocks. For solvent annealing, changes in V_f will occur unless the solvent equally swells each block.

After proper annealing, linear diblock copolymers form features similar in size to the radius of the gyration of each block.[12] Typical BCPs domains range from 5-100 nm

although using especially high χ polymers, features have been made smaller than 3 nm.[13] Their ability to self-assemble into small, densely packed structures, with relative ease has attracted research in many fields such as lithography,[14] drug delivery,[15] and filtration.[16–18]

1.3 BCP Membranes

Part of my dissertation work focuses on using the self-assembly behavior of linear diblock copolymers to create better ultrafiltration membranes. Ultrafiltration membranes reject species between 2-100 nm diameter and are widely used to filter proteins, bacteria, and viruses.[19] Most ultrafiltration membranes manufactured using the nonsolvent induced phase separation (NIPS) technique invented in the 1960's.[20] Pores are made in this process during the rapid exchange of solvent and nonsolvent that takes place as a slurry of homopolymer submerged in water (nonsolvent). As solvent is replaced by water, the T_g of the polymer rapidly drops solidifying into a random, porous, structure (Figure 1.4). NIPS membranes are most widely used because they have decent performance, low material cost, and mature processing techniques. Their major drawback is the large variation in pore size hinders size selectivity. Most NIPS membranes can only separate species that differ in size by at least an order of magnitude.[21]

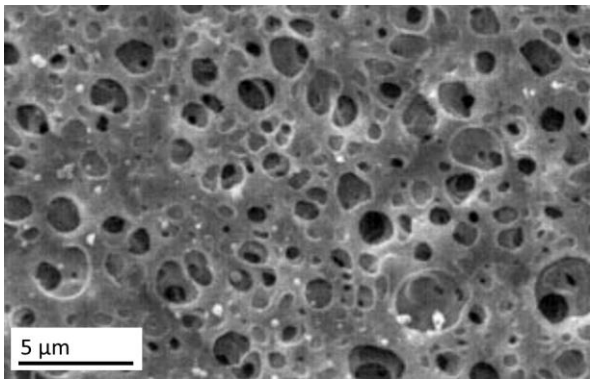

Figure 1.4 *Random pore structure of NIPS membrane.*

SEM image of top surface of a porous membrane made using the NIPS process. Figure adopted from Ref. [22].

In the last couple of decades block copolymers have been adopted to the NIPS process in a technique called SNIPS (block copolymer self-assembly and nonsolvent induced phase separation). SNIPS membranes self-assemble into an ordered porous structure during the solvent-nonsolvent exchange as can be seen in Figure 1.5. However, despite using the same equipment as the widely used NIPS process, SNIPS membranes were never adopted commercially because the cost of BCP far exceeded the cost of homopolymer.

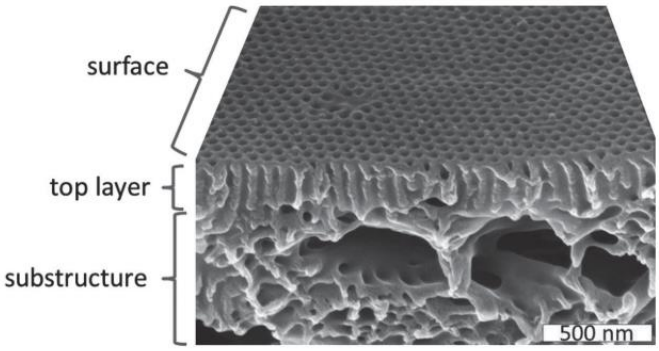

Figure 1.5 *Morphology of SNIPS membrane.*

SEM image of SNIPS membrane. Top surface is ordered, isoporous BCP, that transitions into a macroporous BCP support. Figure adopted from Ref. [23].

To reduce the cost of BCP membranes, a composite membrane approach has been proposed.[24,25] Previous work demonstrated that a thin BCP selective layer less than 1 μm in thickness could be supported by a thick, homopolymer, membrane. This approach solved the material cost issue but created a new one, manufacturability. These handmade membranes require time and labor-intensive steps that hinder mass production. In this work, we develop techniques that overcome two major hurdles facing the scalable production of composite BCP membranes. Firstly, we develop a method to anneal BCPs during casting process by controlling their drying speed. And secondly, we develop a technique to rapidly produce pores in a dense BCP skin by stretching the composite membrane. These strategies help enable the continuous production of inexpensive BCP membranes, making them more economically viable competitors to traditional homopolymer membranes.

1.4 Thermoplastic Elastomers

Thermoplastic elastomers (TPEs) are a commercially successful application of BCPs. They are made from linear triblock and multiblock copolymers whose minor hard domains aggregate giving elasticity to the material. But before going into TPEs in detail, let us start by introducing elastomers.

Elastomers are a broad class of materials characterized by their soft, resilient, mechanical behavior. They can withstand large strains and return to their original shape when unloaded. Elastomers are soft and pliable because they are composed of polymer chains with a low melting point. Typically, the melt temperature (T_m) of elastomers is below room temperature. Because elastomers are used in their melt state, they are soft to the touch, have great dampening properties, and are easily deformed. Without further processing, the polymers which constitute elastomers would behave like a viscus liquid. They would not be able to hold their shape nor recover from large strains. To provide dimensional stability and elasticity to these low T_m materials the polymers are crosslinked. Once crosslinked the material is classified as an elastomer.

Crosslinking binds the polymer chains with one another to form an interconnected network. This network of chains is unable to undergo large-scale chain rearrangement the way millions of discreet chains could. The result is that when deformed, the chains have a energetic preference to return to the chain configuration when they were crosslinked. When stretched, the polymer chains between crosslinks uncoil and align to accommodate the strain as shown in Figure 1.6. This extended conformation is entropically unfavorable and when the stress is released, the elastomer will return to its equilibrium network structure.

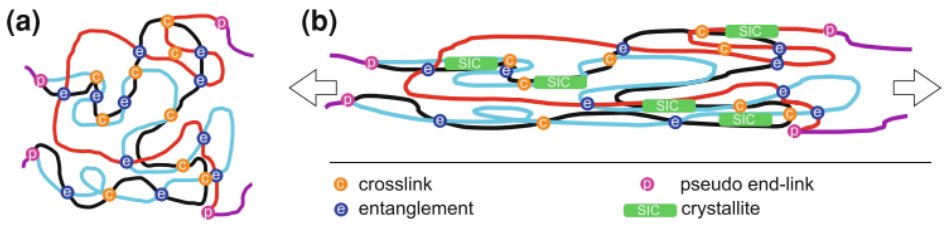

Figure 1.6 *How elastomers chains react to strain*

Representation of a network of elastomer chains (a) before stretch and (b) after stretch. Figure adopted from Ref. [26].

The stress required to deform an elastomer increases the more crosslinked its chains. Crosslinking can be accomplished by either chemical or physical means. Chemically crosslinked elastomers, i.e. rubbers, use covalent bonds to connect the chains. The permanent crosslinks made by this process impart thermal and chemical stability, but also prevent melt processing and recycling of the elastomer. Alternatively, physically crosslinked materials can be recycled because the bonds that form the interconnected network can be broken when exposed to an external stimulus such as heat or solvent. Physical crosslinks can be formed the formation of small crystallites, the aggregation of glassy blocks, or adsorption of chains onto filler. Elastomers that are linked by physical crosslinks are called thermoplastic elastomers (TPEs).

To understand how TPEs work, let us consider the triblock copolymer styrene-butadiene-styrene (SBS). Short styrene blocks at either end of the chain phase separate to form small glassy domains within the soft butadiene matrix (Figure 1.7). At room temperature, each styrene domain functions as crosslinking sites, linking neighboring chains together. The styrene blocks at either end of the chain may phase separate into different hard domains, creating a tie chain between them. Diblock copolymers, which

cannot form tie chains, are considerably weaker. When heated above the T_m of styrene however, the glassy domains disassemble, and the chains are free to flow and rearrange. Many styrene based TPEs exist with various middle blocks, but are functionally very similar.

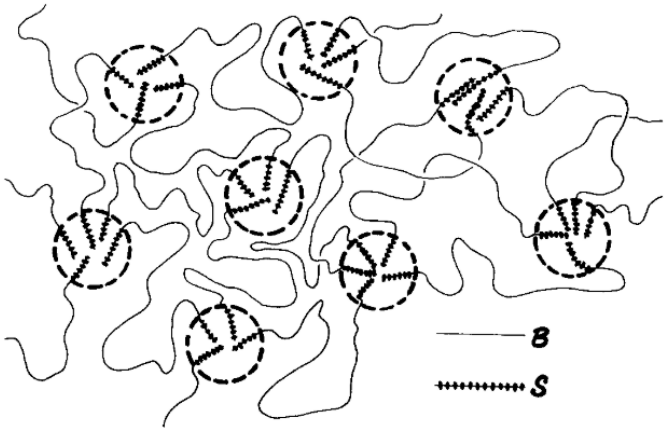

Figure 1.7 *Morphology of SBS triblock copolymer*

Glassy styrene blocks at either chain end form aggregates with other chains to form a network of physical crosslinks. Figure adopted from Ref. [27]

Multiblock TPEs are composed of many hard blocks within a single soft chain. The hard domains are typically polyurethanes, polyesters, or polyamides. The shorter, more numerous, blocks in a segmented TPEs still provide physical crosslinks that give the material elasticity, but do not form ordered structures like triblock copolymers.

TPEs are preferred to rubbers for their recyclability and melt processability. This means faster cycle times, lower energy costs, and better part reproducibility. Rubbers, however, are better in applications that require either low modulus, high temperature/solvent resistance, or low material costs.[28]

1.5 Conclusion

Copolymers often exhibit a variety of properties inaccessible to traditional homopolymers. The most successful copolymers are those which microphase separate. Microphase separation is thermodynamically favorable when the enthalpic benefit outweighs the entropic penalty to demix. This critical point, where enthalpy outweighs entropy, only occurs in materials with a sufficiently blocky architecture. Often these polymers are kinetically trapped in a non-equilibrium state and require an annealing step to reach their thermodynamically stable state.

Linear block copolymers undergo a very ordered microphase separation termed "self-assembly". Self-assembling diblock copolymers contain highly ordered, densely packed, nanometer sized features that are attractive for filtration applications. BCP membranes have been shown in literature to produce high performing membranes but have not yet been adopted commercially. Two challenges facing BCP membrane commercialization that this dissertation addresses are high material cost and insufficient continuous manufacturing techniques.

Tri/multiblock copolymers typically phase separate into less ordered structures. However, because each chain can undergos phase separation at two or more sites, a network of chains is created. TPEs are commercially relevant tri/multiblock copolymers with a soft major phase and a hard minor phase. Unlike traditional elastomers, TPEs can be melt processed making them more suitable for injection molding processes and recycling. This dissertation characterizes the properties of novel polypentenamer based TPEs as possible tire rubber replacements.

Countless unique copolymers can be made by varying monomer combination and chain architecture, each with their own properties. Thus, endless polymer properties are accessible to the polymer chemist to tune a polymer for a given application. The work herein focuses on characterizing copolymers and developing processing techniques that make them more commercially relevant.

CHAPTER II – STRAIN-INDUCED NANOCAVITATION IN BLOCK COPOLYMER THIN FILMS FOR HIGH PERFORMANCE FILTRATION MEMBRANES

Portions of the text in this chapter have been reprinted with permission from:

Weller D.W., Ma G., Galuska L.A., Zhang S., Stringer M., Aracri S., Wang W., Hong K., Gu X., ACS Applied Polymer Materials, **2021**, doi.org/10.1021/acsapm.1c00963

2.1 Abstract

A new pore formation process was investigated for the manufacture of composite ultrafiltration membranes. Phase separated block copolymer (BCP) thin films supported on a compliant macroporous polyethersulfone (PES) support, craze under tensile strain leaving behind pores of predictable size based on the self-assembled nanoscopic domains. The high aspect ratio pores formed in this process were used to create membranes that were highly permeable (959 L/(m^2·h·bar) with near complete rejection of 40 nm diameter gold nanoparticles (AuNP). Using BCPs inherent ability to cavitate under strain, tedious block removal steps are avoided. Membranes can thus be prepared in a simple, roll-to-roll ready, one-step process. In this initial study, BCP craze formation and filtration performance were characterized for various polymer types, molecular weights, and thicknesses. All these factors influenced the BCPs thin film morphology, mechanical performance, deformation mechanism, and ultimately filtration performance. This work demonstrates a possible new path towards achieving scalable, BCP based ultrafiltration membranes.

2.2 Introduction

The ever increasing demand for clean water requires improvements to current water filtration technologies to keep up with demand.[29,30] Ultrafiltration membranes are particularly useful in this field because their pores are appropriately sized to remove bacteria and viruses making them valuable for drinking water purification, as well as waste-water reclaimation.[31] Differing from dense membranes that follow the solution-diffusion model, ultrafiltration membranes rely on a size-selective sieving mechanism. As such, pore structure is the primary influence on ultrafiltration performance. Reducing pore size distribution has been shown to increase selectivity, while increasing porosity and reducing thickness has been shown to increase permeability.[24,32,33] Block-copolymers (BCP) have gained considerable attention based on these criteria due to their ability to rapidly self-assemble into densely packed isoporous structures.[18,34–36]

Initial BCP membranes were thick and suffered from low permeability.[24] To address this challenge, changes to the manufacturing process were made to create asymmetric BCP membranes consisting of a thin isoporous selective layer that transitioned into a macroporous support.[37] The selective layer thickness was reduced to just a few microns and permeabilities were greatly improved. However, the high cost of BCPs decrease the economic viability of these membranes. Composite membranes have been proposed as a solution to this problem.[38–45] By using a thin layer of BCP on top of an inexpensive support, material cost can be dramatically reduced. Composite membranes were initially made by casting BCP onto a sacrificial substrate and then transferring the BCP onto a macroporous support.[33] While this approach showed that thin composite membranes could be made with desirable filtration properties, their

manufacture remained laborious and not scalable. Thus, various new techniques to simplify the manufacturing process were proposed. Phillip *et al.* demonstrated that BCP films could be formed on the surface of a water filled support by using hydrophobic solvent.[24] Hillmyer *et al.* expanded on this process demonstrating that thin (< 100 nm), robust, selective layers could be made with the incorporation of a soft block.[32] Lately there has been a push to develop roll-to-roll manufacturing techniques for BCP membranes.[46–48] One of the challenging aspects of roll-to-roll BCP membrane manufacture is rapid and repeatable pore formation. Many of the common pore forming strategies such as minor block removal[49,50] or selective swelling[51–53] can be slow, and membranes made by phase inversion require large amounts of costly BCP.[54,55] In summary, BCP ultrafiltration membranes can outperform traditional homopolymer membranes, although high material costs and batch process manufacturing methods have prohibited its industrial adaptation.

Herein, we present a method to rapidly create thin BCP membranes that avoid the need for any block removal or selective swelling steps. Polystyrene-*block*-poly(ethylene oxide) (PS-*b*-PEO) diblock copolymer was spun cast onto a water filled polyethersulfone (PES) macroporous support. After tensile strain was applied, the soft minor block domains cavitated and elongated creating a mesoporous structure. We further investigate how polymer characteristics such as minor block type, number average molecular weight (M_n), and block copolymer film thickness, effect membrane robustness by relating thin film mechanical properties to crack formation and filtration properties. This rapid pore forming strategy is a step towards economical, roll-to-roll prepared, BCP membranes.

2.3 Experimental

2.3.1 Materials

PS-*b*-PEO number average molecular weight (M_n) = 80-*b*-30 (110 kDa), PS-*b*-PEO M_n = 58-*b*-22 (80 kDa) were synthesized by anionic polymerization via high vacuum living anionic polymerization of styrene in benzene using sec-BuLi as the initiator at RT for 6 hrs followed by polymerization of ethylene oxide in the presence of *t*-BuP_4 at 45 °C for 48 hrs.[56,57] All other polymers used in this study; PS-*b*-PEO M_n = 102-*b*-34 (136 kDa), PS-*b*-PEO M_n = 480-*b*-227 (707 kDa), Polystyrene-*block*-poly(2-vinylpyridine) (PS-*b*-P2VP) M_n = 79-*b*-36 (115 kDa), PS M_n = 35 kDa, PS M_n = 113 kDa, and PS M_n = 173 kDa, were purchased from Polymer Source Inc. and used as received. All solvents and additives were purchased from Sigma Aldrich and used as received. All PES supports came from a single, 0.45 μm pore size membrane sheet (30 x 300 cm), purchased from Sterlitech corporation and cut as needed. 40 nm Gold nanoparticle (AuNP) solutions were purchased from BBI solutions and diluted with deionized water to a ratio of 1:14 (AuNP solution:water) before filtration.

2.3.2 Membrane manufacture

BCPs were dissolved overnight in toluene to form 1~3 wt% solutions and then heated to 50 °C until solution became clear (≈ 20 min.). After returning to room temperature solutions were passed through a 0.20 μm polytetrafluoroethylene (PTFE) filter at least 2 times. BCP solution (1 mL) was then deposited onto water filled PES (40 x 50 mm) and immediately spun cast. PES rectangles were submerged in water for no less than 1 minute to ensure complete saturation. After removing excess water, the PES

was placed on a silicon wafer to support it. Cohesion forces between the water and silicon held the PES in place during spinning. Spin coating was performed at 2000 rpm (1000 rpm acceleration) for 45 seconds after which samples were further dried overnight in ambient conditions before stretching. Stretching was performed using a custom-built, computer controlled, linear extension stage. Membranes were clamped on either end leaving a 30 mm initial length. Membranes were stretched at 1 mm/s to the desired strain before being removed and punched out with a 25 mm die for subsequent morphology and filtration tests.

2.3.3 Characterization of BCP thin films

Surface topography of the BCP thin films was characterized by a scanning electron microscopy (SEM) (Zeiss Ultra 60 field emission SEM). Prior to SEM imaging, samples were coated with carbon (Cressington 208Carbon) at 100 mv for 10 seconds to reduce charge build up. Cross sectional SEMs were performed after cryofracture. Samples were soaked in ethanol and then immersed 30 seconds in liquid nitrogen. Frozen samples broke upon bending. White light interferometry (Filmetric F-20 UVX) as well as profilometry (Bruker DektakXT) were used to measure film thickness. All thin film mechanical data was collected using our custom-built film-on-water tensile tester at 0.004 mm/s extension speed, corresponding to a strain rate of 5×10^{-4} s^{-1} using a standard 8 mm gauge length dogbone geometry. The details of this experimental setup was previously reported.[58] Representative curves were reported although each test was performed at least three times and are included in the supporting information (Figure A.1). All stress-strain data are reported as engineering stress and engineering strain.

Atomic force microscopy (AFM) (Asylum Research Cypher S) was performed in tapping mode in air. To view the BCP morphology at different depths using AFM, films were oxygen plasma etched (Diener Inc.) for various durations to remove material at a rate of approximately a 1 nm/sec.

2.3.4 Membrane permeability and selectivity testing

A dead-end stirred filtration cell, Advantec MFS Inc. UHP 25 (10 mL), was used for testing membrane performance. The cell receives a 25 mm diameter membrane. Deionized water (18.2 MΩ/cm) was pressurized at 0.2 bar and collected on a scale that recorded its weight every 10 seconds. After an initialization period flux was constant and the slope of weight vs. time was used to calculate permeability (Figure A.2). Similar conditions were used for selectivity studies with the AuNP solutions. Rejection rates were determined by comparing AuNP absorption peak intensity before and after filtration using UV-Vis spectroscopy (Agilent Technologies Cary Series 6000i). An example of how rejection was calculated can be found in Figure A.3. For simplicity, this calculation does not consider effects of concentration polarization.

2.4 Results

2.4.1 Composite membrane manufacture

Figure 2.1 shows the manufacturing process and membrane architecture created in this work. BCPs dissolved in toluene were spun onto a water filled PES support (Figure 2.1a) before being dried and uniaxially stretched using a computer controlled linear extension stage (Figure 2.1b). A water immiscible solvent was necessary to cast a film on

top of the water surface. The final membrane consists of a thin BCP selective layer roughly 100 nm in thickness resting on top of a macroporous support (Figure A.4). The thin BCP selective layer ultimately defines the permeability and selectivity of a membrane while the macroporous PES support provides mechanical robustness. After deposition a self-assembled surface structure of densely packed, circular depressions is evident (Figure 2.1c). After stretching (Figure 2.1d), the minor BCP domains elongated creating a highly permeable porous structure from a previously dense and impermeable membrane. Based on the volume fraction of our BCPs ($V_{f\,PEO} \approx 0.3$), as well as AFM images taken throughout the thickness of our polymer (Figure A.5), we believe that our PS-*b*-PEO samples phase separated into columns aligned perpendicular to the surface. Although columns often prefer to orient parallel to the surface,[59] studies have shown that film thickness,[60,61] directional evaporation,[34] selective solvent use,[63] casting on a neutral surface,[64,65] and casting onto water,[66] can create conditions where perpendicularly aligned cylinders are preferred.

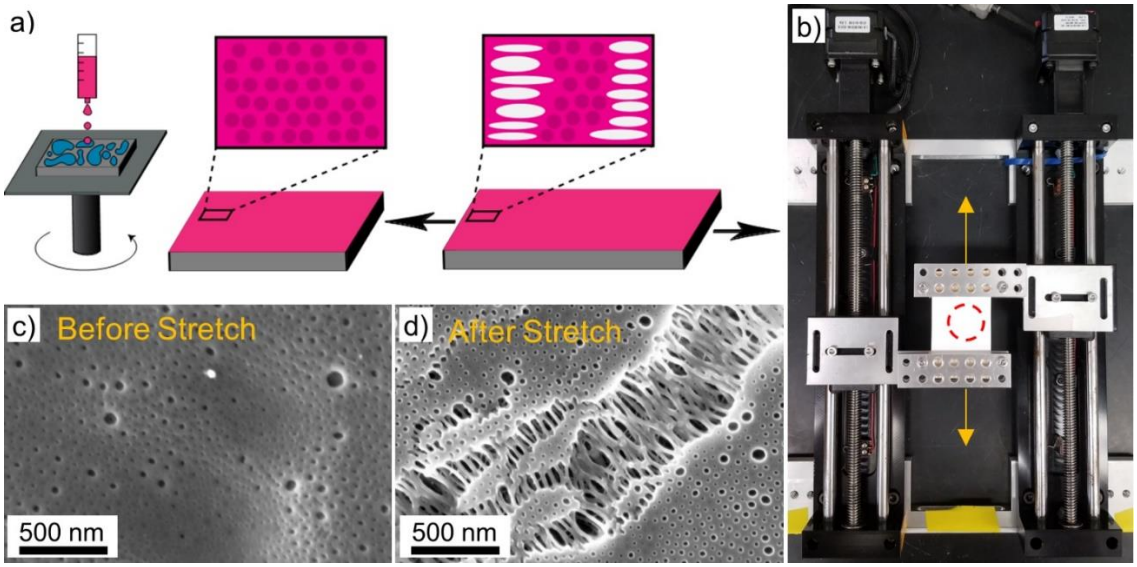

Figure 2.1 *Strain-induced nano cavitation process*

(a) composite membrane manufacturing process. (b) Two motor uniaxial stretching device. Dotted circle represents approximate tested membrane size. (c) SEM image of PS-b-PEO 110 kDa on PES substrate before stretch. (d) SEM image of PS-b-PEO 110 kDa after stretching to 20% strain.

2.4.2 Effect of strain on morphology and membrane performance

PS-*b*-PEO 110 kDa solution was cast onto PES and stretched to different extents to see the effect that strain had on membrane performance and morphology. Membrane performance results, completed in triplicate, are shown in Figure 2.2a (for raw data see Figure A.6). As expected, at higher strains permeability increased and rejection decreased due to the formation and growth of pores. It is notable that at 10% strain, 99.7 (± 0.5) % rejection of 40 nm AuNP was achieved with a flux of 237 (± 38) L/(m^2·h·bar) implying a relatively small maximum pore size. By 20% strain, permeability increased to 1247 (± 409) L/(m^2·h·bar) while AuNP rejection was reduced to 80.7 (± 9.0) %. Scatter in the filtration performance at higher strains is likely due to subtle differences in manufacturing that affect the thickness as will be discussed later. SEM images taken after

0, 10, and 20% strains are shown in Figures 2.2b-d. The white lines observed in the images are imaging artifacts that occur due to charging effects that take place at the sharp edges formed by crazing. These bright streaks nicely show the size and density of the craze formed by tensile stretching. Zooming in on the white streaks (insets) revealed that crazing, not cracking, occurs in these zones. At 0% strain (Figure 2.2b) no flow occurs, showing that strain generates the pores rather than holes formed during self-assembly. By 10% strain (Figure 2.2c) many areas of deformation are present. These areas run perpendicular to the stretch direction and are held intact by threads of polymer. With further strain (Figure 2.2d) the areas of deformation become more numerous and larger, but the integrity of the film remains.

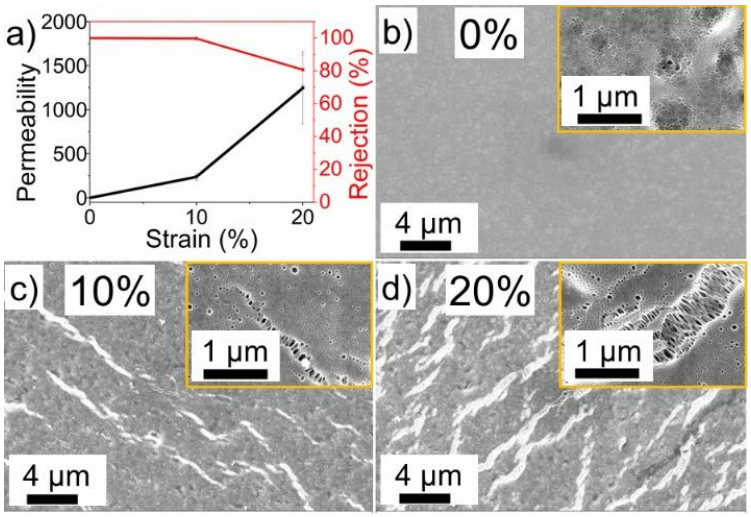

Figure 2.2 *Effect of strain on performance and morphology*

100 nm PS-b-PEO 110 kDa membrane tested at different strains (a) Water permeability in L/(m2·h·bar) and 40 nm AuNP rejection after various levels of strain. (b) SEM image for the composite membrane subject to 0% strain, (c) 10% strain, (d) and 20% strain.

The SEM images show that the pores are initiated from the dark PEO domains. Early work investigating BCP toughness noticed a similar "fishnet" craze behavior in unsupported linear diblock polystyrene-*b*-polybutadiene (PS-*b*-PB).[4] Schwier claimed that the soft PB minor block cavitates once a critical negative pressure is exceeded, followed by necking and drawing of the PS matrix. They also showed that the size of the holes left by crazing is determined by domain size. We noticed similar behavior, observing that pore width scaled with domain size (Figure A.18). As strain was increased, the pores elongated, and the prevalence of crazing increased. Using image processing software (Image J), we found that at 20% strain there were five times as many pores compared to those stretched to 10% strain (Figure A.7). Additionally, stretching between 10 and 20% strain also increased average pore length (90 to 109 nm) while average pore width slightly narrowed (31 to 28 nm). Similar analysis (Figure A.8) determined that increasing from 10 to 20% strain doubled average craze size (1.5 to 3.1 μm^2) and nearly tripled craze coverage (5.1 to 14.7%). This behavior is exciting for membrane formation because permeability can be increased (higher craze density, longer pores) without loss of rejection (pore width remains similar). High aspect ratio pores have been shown theoretically,[67] and experimentally,[68–71] to be more permeable than circular pores without sacrificing selectivity. Our results contradict this behavior as we saw a significant reduction in rejection at 20% strain. This can be explained by again looking at the pore size analysis of Figure A.7, where it can be seen that although average pore width remained similar at higher strain, the number of pores with diameters larger than 40 nm increased greatly. Narrowing pore size distribution should alleviate these issues and increase separation performance.

2.4.3 Polymer structure effect

A glassy polymer can deform by crazing, shear, or cracking.[72,73] As a pore forming strategy, only crazing is desirable. To determine which types of polymers craze when stretched on a PES support, various polymers were used as selective layer and characterized. In addition to measuring membrane performance and morphology, a custom-built film-on-water tensile testing instrument was used to measure the stress-strain curves of the unsupported selective layers (Figure A.9). A description of the set-up is provided elsewhere.[58] Two similarly size diblock copolymers were compared along with a PS control to see the effect minor block has on membrane performance and deformation mechanism. Only PS-*b*-PEO which contains a soft minor block formed crazing while its PS-*b*-P2VP and PS equivalents formed shear deformation zones (SDZs) (Figures 2.3b-d). The mechanical performance showed that the SDZ forming polymers (PS 113 kDa and PS-*b*-P2VP 115 kDa) were more ductile than the craze forming PS-*b*-PEO. The cavities that formed in the PEO containing samples likely acted as crack initiating sites in these thin films, reducing the strain at failure as compared to its dense P2VP counterpart.

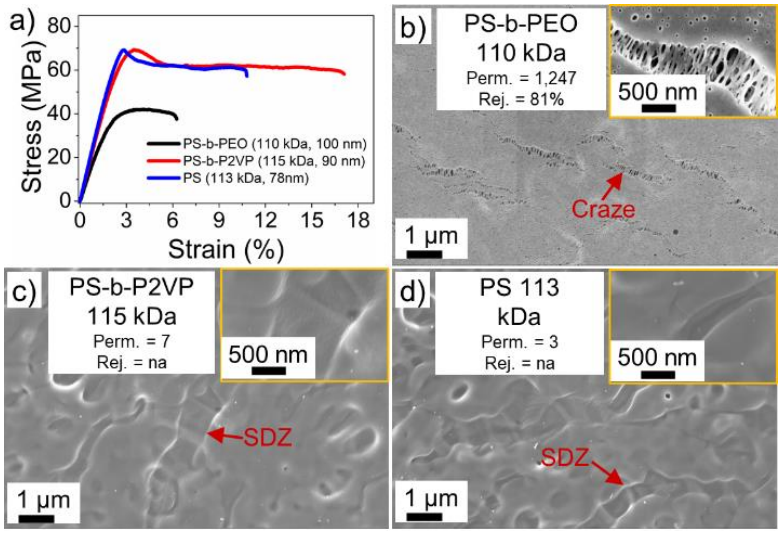

Figure 2.3 *Minor block effect on performance and morphology*

Minor block effect on (a) Film-on-water stress-strain data. (b-d) SEM images of composite membrane surface after 20% strain along with their filtration performance for PS-b-PEO (110 kDa), PS-b-P2VP (115 kDa), and PS (115 kDa), respectively. All permeabilities are in L/(m2·h·bar) and rejections are for 40 nm dia. AuNPs.

When supported on PES, all selective layers were able to be stretched well beyond their fracture strain without cracking (Figure A.10). We attribute this to the stress distribution provided by the PES support. In an unsupported film, thinner areas where SDZ's or crazing occurs will have higher stress where fracture can occur. In a supported film however, strain is evenly applied to the film through the support regardless of local deformations. Strains larger than 20% are possible in these supported films, although we were unable to probe the limit where cracking occurs as our PES support fractured just after 20% strain (Figure A.11). Incorporating a more ductile substrate may be a viable strategy to allow greater strains that further improve craze density and membrane performance.

2.4.4 BCP molecular weight effect

Molecular weight is known to have a dramatic effect on the ductility and toughness of a polymer film as we have shown previously.[74] In this section we explore how the molecular weight of a BCP selective layer influences its mechanical properties, membrane performance, and deformation behavior when stretched to 20% strain. Three PS-*b*-PEO BCP's of varying M_n (80, 110, and 707 kDa) but with similar volume fractions and thickness were used. Additionally, PS homopolymers of various M_n (35, 113, 173 kDa) were used as comparison. In both PS and PS-*b*-PEO polymers, increasing M_n increased strain before failure (Figures 2.4a,e). Both low M_n polymers formed cracks when supported on PES and stretched (Figures 2.4b,f) resulting in membranes with extremely high permeabilities and low AuNP rejection. Both high M_n polymers formed SDZs and were virtually impermeable as can be seen in Figures 2.4d,h (See Figure A.12 for raw data). From these trends it appears that the craze formation is not only unique to BCPs with a soft block, but also only occurs at specific molecular weights.

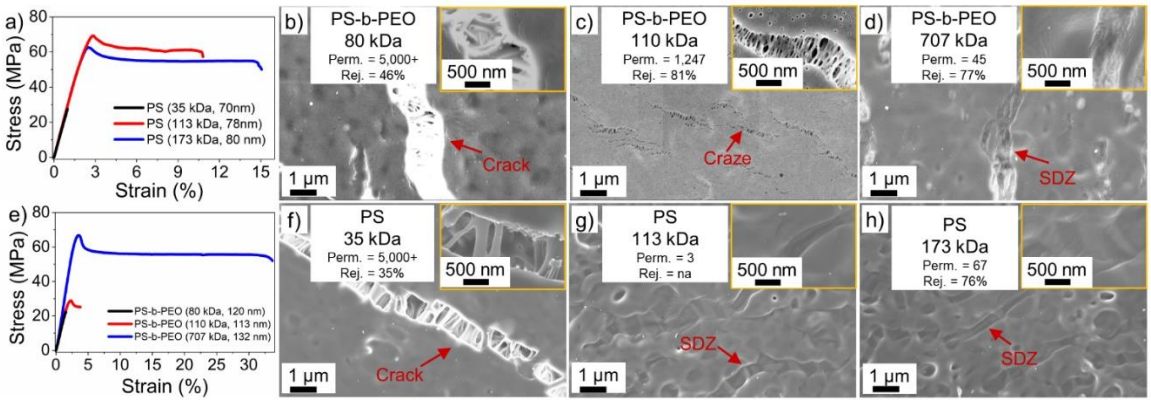

Figure 2.4 *Molecular weight effect on performance and morphology*

Molecular weight effect in PS-b-PEO and PS samples on selective layer tensile strength, composite membrane performance, and craze formation. (a, e) Thin film stress-strain data using film-on-water testing method. (b-d, f-h) Membrane performance and morphology after 20% strain for PS-b-PEO and PS selective layers, respectively. All permeabilities are in L/(m2·h·bar) and rejections are for 40 nm diameter AuNPs.

2.4.5 BCP film thickness effect

Film thickness has been shown to impact mechanical properties and deformation behavior through the confinement effect.[75] Additionally, as thickness is increased, permeability decreases due to increased pore length/tortuosity. To explore the thickness effect, five membranes with varying selective layer thicknesses (PS-*b*-PEO 136 kDa) were stretched to 20% strain and tested for permeability/selectivity. Thickness variation was achieved by depositing different BCP concentrations (10-30 mg/mL) on the PES support. Reported thicknesses were estimated based on the thickness of each concentration when cast on a silicon wafer as measured by interferometry.

Permeability was expected to scale linearly with thickness following the Hagen–Poiseuille equation without greatly effecting selectivity. As seen in Figure 2.5a, above a critical thickness (≈120 nm) this trend was observed (see Figure A.13 for raw data). At

lower thicknesses however, a rapid increase in permeability occurred. For very thin films (58 nm) this is due to film rupture during filtration as rejection of 40 nm AuNPs was just 38%. For 88 nm films however, rejection remained relatively high (89%) demonstrating the abnormally high permeability is not a result of selective layer rupture. Instead it appears the increased permeability comes from a change in morphology/craze-behavior that occurs around 120 nm where thicker films showed smaller domain sizes, more defined crazes, and smaller pores (Figures 2.5b,c,e,f). Optimal performance occurred near 120 nm as well, producing permeabilities of 959 L/(m^2·h·bar) while rejecting an impressive 97% of 40 nm AuNPs. A similar phenomenon, where craze formation, transition to ductile behavior, and optimal filtration performance, all occurred at the same thickness was observed in PS-b-PEO 110 kDa but at a lower thickness (85 nm) (Figures A.14-15).

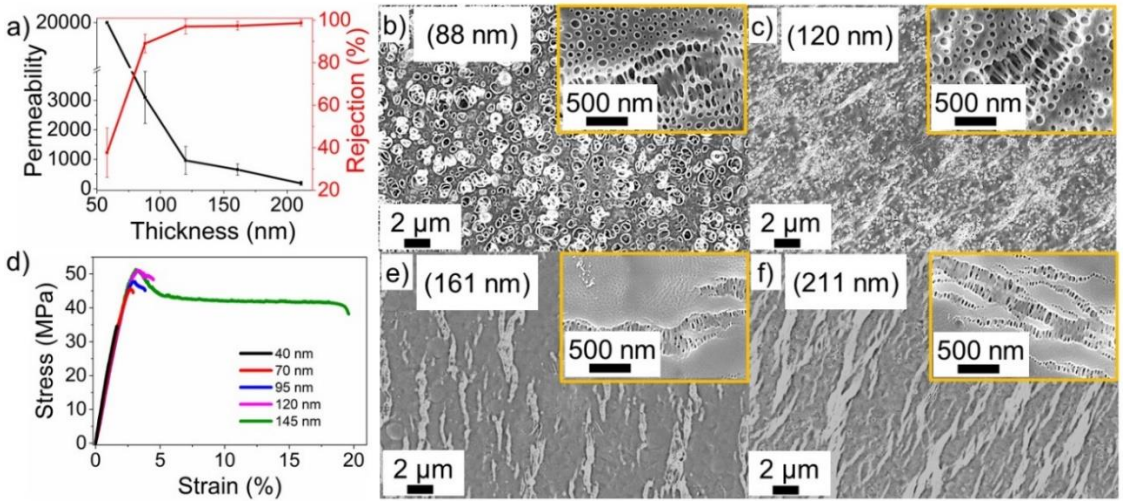

Figure 2.5 *Thickness effect on performance and morphology*

Thickness effect in PS-b-PEO 136 kDa samples on (a) composite membrane performance, (b) selective layer tensile strength, and (b,c,e,f) craze formation. Permeabilities are in L/(m^2·h·bar) and rejections are for 40 nm diameter AuNPs.

Tensile testing of the selective layers also demonstrates a critical shift occurring around 120 nm (Figure 2.5d) where the failure mode shifted from brittle to ductile. This is likely due to changes in interchain entanglement. Recent work by Zhang et al. demonstrated the thickness of polymeric thin films greatly impact the fracture behavior using a unique thin film fracture energy measurement tool.[76] Samples thick enough to fail ductility showed much more repeatable permeability as seen by the smaller error bars. It is likely that much of the error that occurred throughout this study is due to slight changes in thickness that occurred during the coating process. Between 88 and 120 nm a change of thickness of just 10 nm would create a change in permeability of over 600 $L/(m^2 \cdot h \cdot bar)$.

2.4.6 Discussion

This work is the first investigation, to the authors knowledge, using BCP guided cavitation to create a filtration membrane. BCP membranes made prior to this work either relied on the phase inversion process to create pores, which requires a large amount of BCP, or used a minor block removal step which is time consuming complicates the scale-up process. Strain-induced nano cavitation on the other hand has the potential to be both manufacture and material cost friendly. Using strain to create pores is not a new idea and has been used commercially in homopolymers for decades in products like Gor-Tex which is expanded polytetrafluoroethylene. Pores are generated by cavitation of the softer amorphous regions of a semicrystalline polymer. Typically these types of membranes are in the microporous regime,[77] however controlled crystallization has been used in expanded polypropylene films to form pores with widths as low as 25 nm.[78] Potentially,

even smaller pores could be made using BCP guided nano cavitation as BCP domains can be as small as just a few nanometers.

In this proof of concept work, we showed that strain is a valid method of pore formation in BCP films, and that it creates membranes whose performance is on par with many other literature reports of BCP membranes[43,79,80] This is promising, considering the simplicity of the process. It would be disingenuous however, to ignore the challenges that still must be overcome for this technique to succeed. Two issues that must be addressed are (1) performance relative to commercial membranes and (2) size selectivity. The ultrafiltration community has adopted bovine serum albumin (BSA) as a standard to compare filtration properties.[81] BSA filtration performance was evaluated for 120 nm PS-*b*-PEO 136 kDa membranes stretched 20%, achieving a rejection of 47% with a permeability of 967 L/(m^2·h·bar) (see Figure A.16 for raw data). Figure 2.6a, adapted with permission from Ref. [81], shows how this membrane compares with other commercial membranes where the separation factor was calculated as 1/(1-Rejection) and the black line represents the theoretical upper limit of efficiency assuming a log normal distribution of pore sizes. It is possible for BCP membranes to exceed this theoretical limit because of their isoporous nature but in this test, our membranes were outperformed by commercial polysulfone and cellulosic membranes.

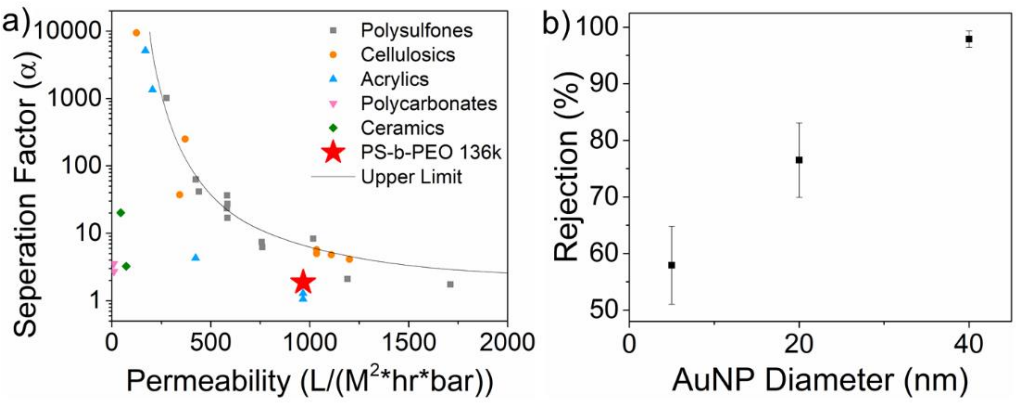

Figure 2.6 *Permeability selectivity performance comparison*

(a) Ultrafiltration permeability/selectivity comparison with typical commercial membranes. Figure adapted with permission from Ref. [81]*. (b) Size selectivity performance of 120 nm PS-b-PEO 136 kDa.*

Poor BSA filtration performance was expected as our membrane pore size was not optimized for rejecting such a small species (3.9 nm R_h[82]). Additionally, the size-selectivity curve (Figure 2.6b) was not as steep as other BCP membranes have shown. In many separations it is desirable to completely block a larger species while rejecting very little of another. In this membrane around 57% of the 5 nm dia. AuNPs were rejected despite being 8 times smaller than the 40 nm dia. AuNPs. We believe membrane adsorption is responsible for the high rejection of small species. In a future work we plan to steepen the curve by annealing our films to better control domain size, tightening pore size distribution, and coating our membrane in polydopamine to prevent the adsorption.

2.5 Conclusion

The work presented here demonstrates that strain-induced crazing can be used as a pore formation method to create BCP membranes with low material cost and easy manufacturability. Controlling craze was critical to success, and design criteria for three

key variables were determined. Firstly, a soft minor block (PEO) was necessary to induce crazing while hard minor blocks (P2VP) underwent shear deformation. Secondly, craze only occurs at intermediate M_n (110-136 kDa). Lower M_n BCPs (80 kDa) formed cracks while much larger M_n (707 kDa) formed SDZs. And finally, two critical thickness were determined, one at 88 nm, above which polymers were robust enough to be tested without rupturing, and another at 120 nm, above which failure was ductile and crazing was more defined. The filtration performance of these membranes was on par with other BCP membranes described in literature. The standout feature of these membranes is their ability to be made in simple one-step process attractive for use in large-scale roll-to-roll manufacturing. Further improvement of filtration properties is expected as the technique becomes more mature.

CHAPTER III – ROLL-TO-ROLL SCALABLE PRODUCTION OF ORDERED MICRODOMAINS THROUGH NONVOLATILE ADDITIVE SOLVENT ANNEALING OF BLOCK COPOLYMERS

Portions of the text in this chapter have been reprinted with permission from:

Weller D.W., Galuska L.A., Wang W., Ehlenburg D., Hong K., Gu X., Macromolecules 2019, 52, 5026−5032

3.1 Abstract

A new method, Non-Volatile Additive Solvent Annealing (NVASA), has been developed to anneal block copolymers during film deposition by controlling the solvent drying process. Precise amounts of high boiling point additive added to the polymer solution briefly remain in the polymer film after casting, leaving the film in a swollen state increasing its chain mobility, and ultimately improving domain order. We demonstrated the effectiveness of NVASA on several block copolymer systems and used in situ grazing incidence small angle X-ray scattering (GISAXS) to validate the ordering process during the self-assembly. The simplicity and reproducibility of the method is attractive for implementation in large scale manufacturing processes such as roll to roll printing as swell ratio is easily controlled by the amount of additive used and separate annealing steps are not needed. This work potentially introduces a new way to quickly and cost effectively anneal block copolymers.

3.2 Introduction

Block copolymers (BCP) are chemically dissimilar polymers covalently bound together. If the blocks are sufficiently incompatible with one another they phase separate, but because they are permanently bound to one another nanophase separation occurs rather than a bulk phase separation.[83] BCP's ability to self-assemble into nanoscale features is a phenomenon that has been studied for over 40 years establishing a rich knowledge base of theory as well as techniques.[84–87] BCP chains self-assemble based on thermodynamics and energy minimization, although kinetic factors often trap BCP's in a morphology far from equilibrium because chains are unable to arrange into their preferred state. This is often the case when films are formed from solution (e.g. spin coating, doctor blading). In solution, BCP chains have high mobility but low propensity to phase separate as solvent lowers their effective χ. In a dried glassy film, the opposite is true. A high χ value exists between the polymer blocks driving phase separation but lack of chain mobility results in a kinetically frozen molecular landscape thus limiting nanophase separation. In neither case will effective phase separation take place. Therefore, traditionally after solution coating, where there is a rapid change from solution to solid, a secondary annealing step is needed to give the chains enough mobility to find their equilibrium state.[88]

Annealing of polymer films can be accomplished by raising the BCP temperature above its glass transition temperature (Tg) as is done in thermal annealing (oven,[89] microwave[90–92], laser[93–97]) by reducing the polymers' Tg below room temperature as in solvent annealing,[98] or a combination of the two as in solvothermal annealing.[99] Solvent vapor annealing (SVA) is widely used to promote long-range order in BCP thin films as

it is generally faster than thermal annealing and can be used with thermally sensitive materials.[100] In SVA, a film is swollen after being exposed to a solvent vapor environment. As the film grows in thickness achieving a higher swell ratio (SR), BCP chain mobility is enhanced through a combination of the plasticizing effect from solvent molecules and a reduced χ parameter allowing blocks to briefly pass through domains of dissimilar blocks during reorganization.[101,102] One of the early challenges SVA faced was poor repeatability and reproducibility because solvent uptake into a polymer film can be heavily influenced by environmental conditions (e.g. temperature, partial vapor pressure of solvent in chamber). More recent work using in situ interferometry with proportional–integral–derivative (PID) controlled flow meter greatly improved the reproducibility of the annealing process. For example, the Buriak group showed that PID controllers could be used to regulate a solvent vapor generator allowing highly controlled swell ratios.[103] Their work, showed that effective annealing only occurs once a critical SR has been reached, past which ordering happens quickly and spontaneously.

Despite steady progress in understanding of BCP assembly, industry adoption remains virtually absent as many of the processes are long, complex, and difficult to reproduce. A process to simply, reliably, and rapidly anneal BCP chains is needed for industrial adaptation and has been attempted in multiple ways. Xu et al. showed that solvothermal annealing can speed up the annealing process to reduce the annealing time from hours to minutes, and even down to seconds to form ordered domains.[104] Rapid thermal annealing has also been achieved by the formation of temperature gradients and laser writing.[95,105] While these techniques show promise, they add a dimension of

complexity to the process and require specialty machinery as well as tight process control.

In this report, we introduce a new annealing method termed non-volatile additive solvent annealing (NVASA) to rapidly order the BCP film as it is being deposited. We demonstrated the NVASA process using various BCP systems and verified the assembly process using in situ interferometry and grazing incidence small angle X-ray scattering (GISAXS) during the film deposition. The NVASA method is simple to use, highly reproducible, and broadly applicable to many BCPs. This method eliminates the need for additional annealing steps and shows great potential for use in high volume production techniques such as continuous roll-to-roll manufacturing as demonstrated in this work.

3.3 Experimental

3.3.1 Materials and preparation of BCP films

Polystyrene-block-poly(ethylene oxide) (PS-b-PEO) Mn = 80-b-30 kg/mol was synthesized by anionic polymerization according to previous reports.[106] Polystyrene-block-poly(2-vinylpyridine) (PS-b-P2VP) Mn = 40-b-18 kg/mol was purchased from Polymer Source Inc. All solvents and additives were purchased from Sigma Aldrich and used as received without further purification.

Films were coated on bare silicon wafers after a 5-minute oxygen plasma cleaning (Diener Inc. at 10 m torr, 20 sccm O_2, 40 watts). BCPs were dissolved overnight in toluene (host solvent) to form 1~3 wt% solutions before high boiling point additive (chloronaphthalene or methylnaphthalene) was added to achieve targeted swell ratios. BCP solution was deposited into films by either solution shearing using a custom-built

shear stage or spun coat onto silicon. Spin coating was performed at 3000 rpm for 5 sec after which samples were further dried in ambient conditions. All thin films were immersed in ethanol for reconstruction at room temperature for 15 min, then etched in oxygen plasma for 10 s to enhance the contrast between major and minor blocks for imaging.

Roll-to-roll printing was performed on one-inch-wide polyethylene terephthalate (PET) without surface treatment. PS-b-PEO dissolved in toluene (10 g/L) with a SR of 3 of chloronaphthalene was delivered to the slot die head through a syringe pump at a speed of 0.5 mL/min while the PET substrate traveled 0.3 meter/min. Ethanol bath temperature was maintained between 43 and 47 °C by a silicon heating pad and thermocouple.

3.3.2 Characterization of BCP films

White light interferometry (Filmetric F-20 UVX) was used to measure film thickness during the film drying process. The reflected spectrum was collected every 100 ms to capture rapid solvent evaporation and analyzed in Filmetric software to obtain the film thickness. In situ GISAXS experiments were performed at beamline 1-5 at the Stanford Synchrotron Radiation Lightsource (SSRL) with an X-ray energy of 12.7 keV. The exposure time to collect each scattering profile was 10 seconds. The sample to detector distance (SDD) was around 2750 mm and calibrated by a silver behenate standard. The incidence angle between X-rays and the sample surface was fixed at 0.14° throughout the experiment. Scattering profiles were recorded on a Mar CCD 2-D area detector. The 2D scattering image was processed in Igor software with Nika package.[107]

The data was fitted to extract the structure factor of the ordered domain (e.g. peak position).

Surface topography of the BCP thin films was characterized by using either a scanning electron microscopy (SEM) (Zeiss Ultra 60 field emission SEM), or a Veeco Nanoscope Atomic Force Microscope (AFM). AFM was used to image the top surface morphology of BCP sample in air and in tapping mode.

3.4 Results and discussion

3.4.1 NVASA concept

Figure 3.1 shows the concept of NVASA to simultaneously deposit and order a BCP thin film. High boiling point (HBP) solvent is added to BCP solution to alter the evaporation step by creating a two-step drying profile: rapid drying of the host solvent followed by slow drying of the HBP additive. PS-b-P2VP and chloronaphthalene (CN) HBP additive is the model system we used to demonstrate the NVASA process. PS-b-P2VP polymer was dissolved in toluene to create a stock solution before adding the desired amount of CN. After spin coating the solution, toluene quickly evaporates leaving a CN swollen block copolymer film, mimicking the conditions where ordering occurs in traditional solvent vapor annealing.

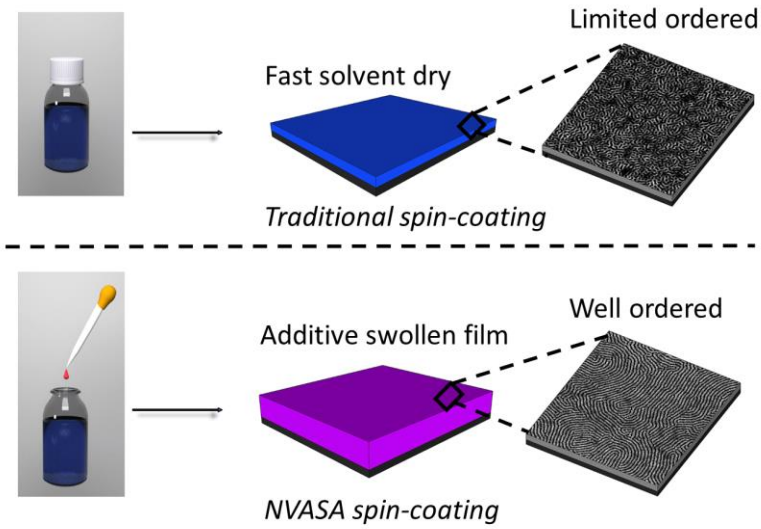

Figure 3.1 *NVASA concept overview*

NVASA process used to improve order of PS-b-P2VP upon deposition. (Top) Spin coating without HBP additive results in rapid thickness loss and therefore traps BCP into nonequilibrium morphology. (Bottom) Spin coating with CN HBP additive creates a swollen film with more mobility, producing a highly ordered morphology once dried. After complete drying (a few min) both films are the same thickness.

3.4.2 Effect of HBP additive on drying profile and BCP morphology

We first tested the effect of CN additive on the morphology of PS-b-P2VP by controlling the degree of swell ratio (SR). In the NVASA process, SR is precisely controlled by adding the desired volume of additive to the BCP solution. For example, a SR of 2 indicates that in the solution, there are equal amounts of HBP additive and polymer (by weight), thus after toluene evaporates, a spun cast film will have 1:1 ratio of polymer and CN additive in the deposited films. This pre-metered process ensures that after deposition the BCP thin film consistently achieves the same SR, despite environmental conditions (e.g. room temperature, humidity).

PS-b-P2VP with CN additive at different SRs ranging from 2 to 5 were manufactured and characterized. Ink was doctor bladed onto a silicon substrate using a custom set-up as reported previously.[108] Film thickness was monitored by white light interferometry during the film drying process (Figure 3.2a). Film thickness profiles of four samples with different SR are shown Figure 3.2b. For BCP ink without additives, the film thickness decreased rapidly from ~2.5μm (wet liquid film directly after deposition) to a dry film of ~40 nm within 10 seconds. Rapid drying resulted in poorly ordered polymer microdomains as shown in Figure 3.1. After adding CN to the BCP ink, the drying process showed two discrete steps, a fast drying of the host solvent (toluene) at ~100 nm/s and a slow drying of additive (CN) at 0.5 nm/s. The prolonged stay of HBP additive in the film resembles the SVA process giving inspiration for the name NVASA. Surface morphology of films cast with different SRs was quantified by scanning electron microscopy (SEM) (Figure 3.2c) after reconstruction in ethanol to enhance topographical contrast as previously described.[109,110] BCP order improved with increasing SR. At low SR (1.5, 2.0 and 2.5), order only slightly improved. At SR 3 order further improved and by SR 3.5 and 4 reasonable order was achieved with grain sizes up to ~300 nm. Other methods including traditional solvent annealing have been used to create better order at the expense of processing time for larger grain sizes (Figure B.9), however the NVASA process produces results faster and we expect, as with any new process, that results will improve as the method matures.

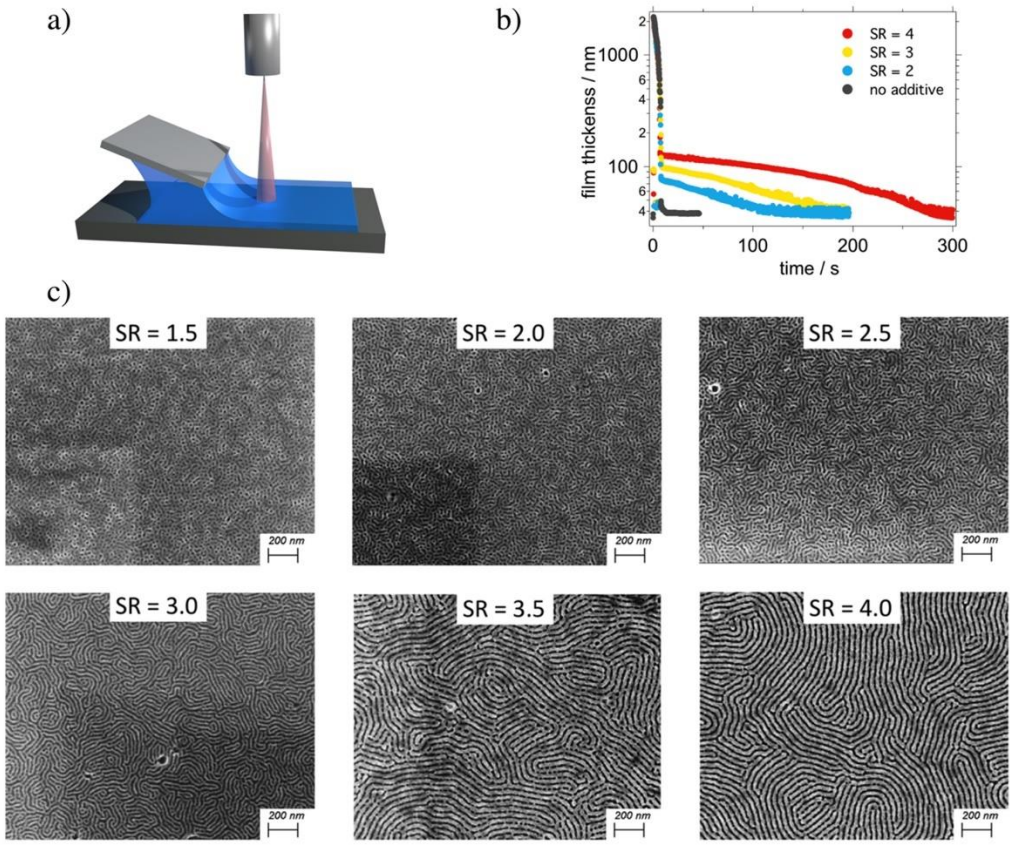

Figure 3.2 *Swell ratio effect on PS-b-P2VP ordering*

The drying process and surface morphology of PS-b-P2VP swollen with various amounts of CN. (a) schematic of the doctor blading set-up in combination with white light interferometer. (b) film thickness evolution during the drying process at different swell ratio. (c) SEM image of polymer film annealed with different amounts of additive. Six different swell ratios (SR from 1.5 to 4) are shown here. Dark areas in SEM images are artifacts generated by charge build up and damage from the electron beam.

3.4.3 Structural evolution of BCP during NVASA process by GISAXS

In situ GISAXS was used to understand how HBP additive effects self-assembly kinetics by monitoring order in the film during drying. In situ X-ray scattering is a powerful, non-disruptive, method to probe the polymer ordering process.[111,112] PS-b-P2VP with CN additive (SR 4) was doctor bladed onto a silicon substrate and left to dry in air while GISAXS was simultaneously performed on the drying film (Figure 3.3a). A

photo of the shear coater used for deposition can be found in the supporting information (Figure B.1).

GISAXS results were recorded and analyzed according to previous reports and protocol.[112] Interferometry was used simultaneously to link order with thickness (SR). Drying consisted of two distinct drying stages (one from the drying of toluene, and the other from the CN additive) in agreement with previous measurements (Figure 3.3c). Figure 3.3b shows the scattering intensity vs scattering vector plot at different swell ratios and Figure 3.3d shows representative 2-D scattering patterns. We consider the 3% BCP solution as a highly swollen film with SR of 32. Initially, at this high SR, BCP's are fully dissolved and no structure factor can be observed.

As host solvent leaves the film, the effective Flory-Huggins interaction parameter between the two blocks increases, and a disorder-to-order transition occurs at a SR of ~2.68. From there, order continues to improve reflected by the intensification and sharpening of the scattering peak in Figure 3.3d. Scattering curves were then fit to obtain peak position and full width at half maximum (FWHM). Figure 3.3c shows that within the first 200 seconds of drying, the BCP is in the disordered state and no scattering peak originating from the structure factor of an ordered BCP lattice was observed. At around 200 seconds (or a SR ~2.68) the scattering peak starts to show up becoming most intense and sharpest after ~350s indicating high order. After this point there is a decrease in intensity and a broadening in the FWHM. We attribute the loss of order between 350 and 600s to slow drying speeds. As solvent leaves the BCP the χ parameter between the blocks increases and therefore the preferred domain spacing increases, but polymer movements are limited at such low swell ratios and the polymers become kinetically

trapped in an intermediate state. Initially, the scattering peak was at 0.0175 A-1 (red curve in Figure 3.3c). The peak position continues to shift to lower q values, consistent with increased interaction between two blocks. For a fully dried film, the peak position stabilized at 0.0159 Å-1. The ordering process is also evidenced from the drop in FWHM. Real-time scattering results support our hypothesis that the ordering of the block copolymers occur during film drying with the help of a slow drying additive.

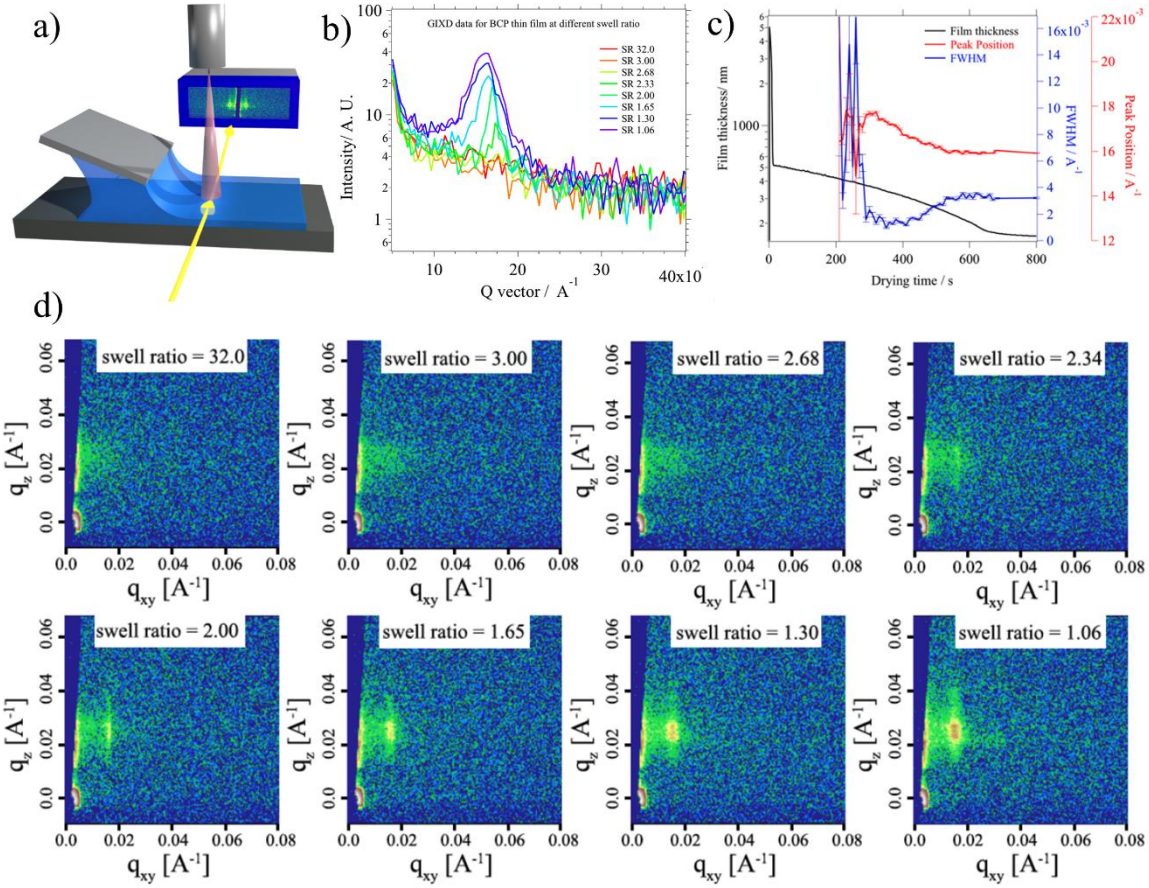

Figure 3.3 *In situ GISAXS during drying*

In situ GISAXS to quantify the ordering process of PS-b-P2VP (a) Schematic of in-situ GIXD scattering set-up with custom made blade coater combined with interferometry. (b) evolution of the scattering profile during drying (c) film thickness, peak position and FWHM of the scattering peak plotted with drying time. (d) representative frames of 2-D GISAXS data at different stages of drying. SR32.0, 3.00, 2.68, 2.34, 2.00, 1.65, 1.30, and 1.06 occur at drying times of 0, 89, 200, 221, 376, 477, 580, and 658 seconds respectively. Note that drying time depends on the thickness of film, thicker films taking longer to dry.

3.5 NVASA applied to different BCP systems and morphologies

NVASA is a simple method capable of annealing multiple block-copolymer systems of varying morphologies and molecular weights. PS-b-PEO undergoes an order-order transition from spherical (Figure B.10) to cylindrical morphology (parallel to surface) during annealing. The onset of this transition moves predictably to higher SR as Mn is increased due to the unfavorable kinetics of restructuring. In the case where SR is near the order-order transition, hexagonal packing of the spherical domains can be improved by the NVASA process (Figure B.2-3). It is also noteworthy that various HBP additives can be used with similar results (Figure B.4). Figure 3.4 demonstrates that NVASA is also capable of improving hexagonal packing order. PS-b-PEO films were cast with different amounts of CN additive (SR = 1,2,3), improving order (Figure 3.4a-c) by increasing chain mobility, indicated by the island and hole formation at larger length scales (Figure 4d-e). Island and hole formation appear after ~60 seconds of drying and is fully developed after ~180 seconds (Figure B.5). Films were spun coat on Si wafers for 5 seconds removing the host solvent while leaving behind a swollen PS-b-PEO film to dry in ambient conditions (~1 min). Color change in the film during the spinning process stopped after ~4 seconds because film thickness stops rapidly changing indicating that toluene had been effectively removed. Interferometry was again used to monitor the drying process. Using more or less CN the drying process could be tuned (Figure B.6).

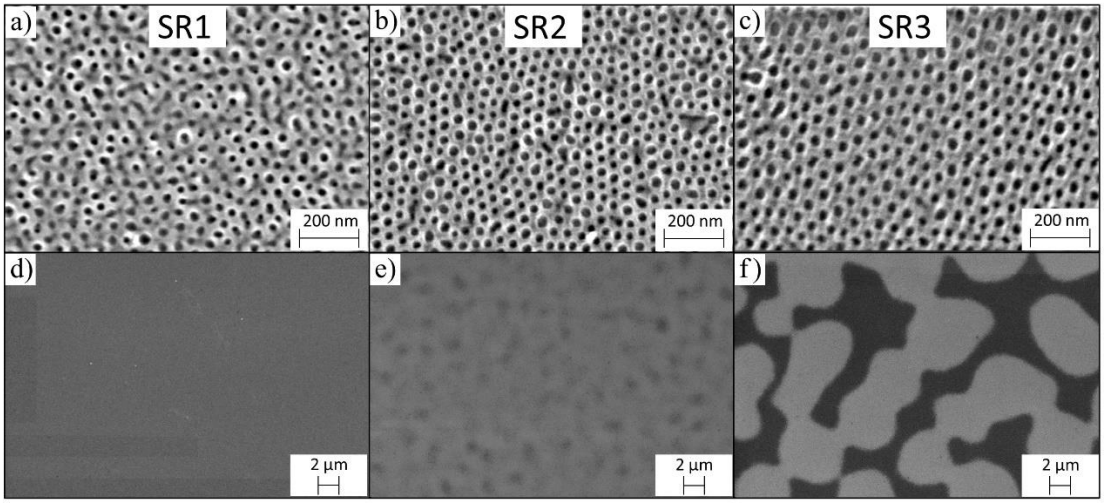

Figure 3.4 *Swell ratio effect on PS-b-PEO*

Effect of CN on PS-b-PEO from SR1 (no additive) to SR3. (a-c) shows that hexagonally packed spheres become more ordered with higher SR. (d-f) are zoomed out views of the same films showing the formation of island and hole morphology often seen after solvent annealing and a strong indication that the additive imparts mobility to the chains before evaporating.

Noticing that film thickness is constant after just a couple minutes using the NVASA process, we recognize the time in which a film remains swollen is relatively short, and better order could be achieved if the film remained in its swollen state longer. Dibutyl phthalate, a common plasticizer, was used in place of CN. Dibutyl phthalate does not evaporate appreciably in ambient conditions and remains in the swollen film until it is rinsed away in an ethanol bath. We named this plasticizer assisted solvent annealing (PASA). To demonstrate the idea, a 30 nm PS-b-PEO film was swollen to 3 times its original thickness (SR3) with dibutyl phthalate for ~30 min resulting in a highly ordered, hexagonally packed, pillar morphology (Figure 3.5a). Thickness loss in ambient conditions was slower than 0.1 nm / min (Figure 3.5b) showing that SR is held essentially constant until the plasticizer is extracted in a room temperature ethanol bath. Order is maximized at a SR of ~3 (Figure B.7) and shows significantly better order than films

swollen with CN, although the reason for such a dramatic improvement in is not yet fully understood. We hypothesized that order would be improved using dibutyl phthalate as an additive because it would increase the time that polymer chains remain in a swollen state, however there are other factors which may have had in impact on order. We predict that because dibutyl phthalate is rapidly removed, in contrast to CN which evaporates over 100's of seconds, the χ parameter, and therefore domain spacing, remains constant resulting in better order. Dibutyl phthalate also has different solubilizing effects on the BCP compared to CN as indicated by the inverse morphology it produces. CN preferentially solvates PS while dibutyl phthalate is a good solvent for both blocks but preferentially swells the PEO domains (Table B.8). Regardless of the morphology, the result show that plasticizer annealing, although slower than non-volatile annealing, has the potential to create very ordered structures.

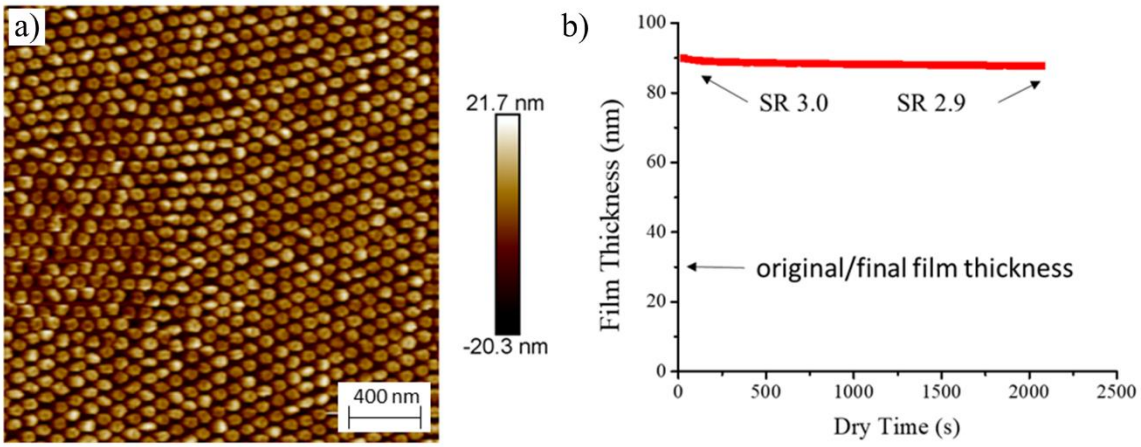

Figure 3.5 *Plasticizer additive effect on morphology*

PS-b-PEO annealed with dibutyl phthalate additive for 45 min achieves highly ordered column formation. (a) AFM image of PS-b-PEO film annealed using PASA process. (b) film thickness vs annealing time profile for PS-b-PEO film swelled with dibutyl phthalate showing minimal evaporation at RT.

3.5.2 Continuous production using roll-to-roll coater

NVASA is a simple, rapid, and low-cost method to produce ordered microdomains creating opportunities for this technology to be incorporated into large scale manufacturing processes. We demonstrated this by using the technique in a custom-made roll-to-roll printer (Figure 3.6) and continuously printing ordered nanophase separated films. The NVASA ink is slot-die coated onto a flexible polyethylene terephthalate (PET) substrate before traveling through a heated ethanol bath where it is reconstructed and then finally rewound. Figure 3.6a-b depicts the setup by schematic drawing as well as photograph. A syringe pump meters the solution and a programable rotary motor sets the casting speed. Film thickness is controlled by adjusting the slot-die gap height, solution concentration, and motor speed. Specific coating conditions used in this work are described in the experimental section and a movie of the coating process is included in the supporting information. After deposition, the film travels through a heated ethanol bath to selectively swell the minor block and create pores as described previously in this paper. We first demonstrated the NVASA roll-to-roll process on a PET substrate. Figure 3.6c shows the optically clear, coated PET film and its ordered microstructure which we were able to produce at a rate of 760 mm^2/min. AFM imaging confirms the formation of ordered micropores resulting from the continuous printing process Figure 3.6d.

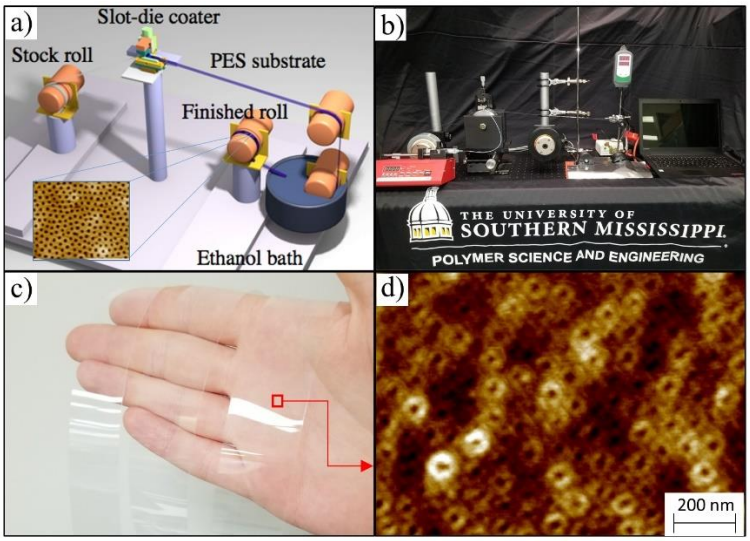

Figure 3.6 *Roll-to-roll printing using NVASA*

NVASA process used to produce large area ordered structures using in situ roll-to-roll printing process. (a) printer schematic (b) Photograph of the actual setup. (c) Photograph of PET film with ordered pores through continuous NVASA printing process. (d) AFM image of PS-b-PEO nanopores on a PET substrate.

3.6 Conclusion

This work demonstrates that NVASA can be used to quickly order block copolymers without extra steps or machinery and can be easily incorporated into high volume manufacturing techniques such as roll-to-roll printing. We have shown that high boiling point solvent additives such as CN create a two-step drying profile, and the effective SR experienced by a polymer film is proportional to the amount of additive used. The NVASA process clearly enables chain mobility after deposition and works with multiple block copolymer systems improving both fingerprint and hexagonal packing. As we turn towards finding applications for the exciting self-assembling properties of BCP's, it is essential that we find techniques which are both economically feasible as well as practically manufacturable.

CHAPTER IV – LONG-CHAIN BRANCHED POLYPENTENAMER RUBBER: TOPOLOGICAL IMPACT ON TENSILE PROPERTIES, CHAIN DYNAMICS, AND STRAIN-INDUCED CRYSTALLIZATION.

Portions of the text in this chapter have been reprinted with permission from:

Weller, D. W., Halbach, R., Rohde, B., Kang, S., Dwivedi, S., Mehringer, K. D., Shankar, R., Storey, R. F., Morgan, S. E., Zabula, A. V., Gu, X. & López-Barrón, C. R. ACS Applied Polymer Materials **2021,** 3, (5), 2498-2506.

4.1 Abstract

In this work, the effect of long-chain branching (LCB) on the tensile properties of sulfur-cured, unfilled, polypentenamer rubber (PPR) was investigated. Branched PPR, prepared by ring-opening metathesis copolymerization (ROMP) of cyclopentene (CP) and dicyclopentadiene (DCPD), showed improved mechanical strength demonstrating greater than three times higher tensile stress at 500% strain compared to its linear counterpart (a homopolymer of CP). *In situ* wide-angle X-ray scattering (WAXS) showed that branching units caused significant changes in the strain-induced crystallization (SIC). At low temperatures linear PPR underwent rapid SIC after a critical stretch was reached while branched PPR crystalized more slowly. However, SIC is not the cause of the enhanced mechanical strength. Elevated temperature experiments confirmed that even in the absence of SIC, LCB PPR exhibits a stiffer stress-strain response. We propose that the stiffer behavior of branched PPR is caused by a reduction in chain mobility. The

origins of reduced chain mobility likely come from topological constraints imposed by the LCB architecture, and also from an unintended nanofiller effect created by microphase separation of DCPD-rich domains. The work described here is the initial investigation of adding branching units to PPR to improve elastomer performance.

4.2 Introduction

Natural rubber (NR) remains the peak performance elastomer despite nearly a century of searching for synthetic alternatives that do not require foreign dependence on rubber trees. Due to its unique properties NR is used in over 40,000 consumer products, although its largest market by far is tires.[113] Styrene-butadiene-rubber (SBR) has very similar tensile properties to NR and is a sufficient alternative in many consumer tires, although it exhibits lower elongation at break as well as lower tear resistance. In more demanding applications such as aircraft and trucking tires, SBR is unable to replace NR, motivating the industry to explore different synthetic elastomers that may fulfill this need. It is widely believed that NR is stronger, tougher, and more durable than its SBR replacement because it exhibits strain-hardening caused by strain-induced crystallization (SIC).[114] The impact of SIC can be easily seen by comparing NR to its synthetic equivalent polyisoprene. Polyisoprene lacks the perfect regioregularity and natural impurities present in NR that aids its strong SIC response, and exhibits greatly reduced strength and toughness.[115,116] This comparison illustrates the dramatic impact that chain structure and SIC can have on a rubbers properties.

Polypentenamer rubber (PPR) is a synthetic elastomer prepared by ring-opening polymerization of cyclopentene followed by vulcanization. The low melting point of PPR

(0 – 25 °C, tunable by the *cis/trans* ratio) leads to SIC behavior, which makes it a potential NR replacement. Early synthetic work developing ring-opening metathesis polymerization (ROMP) of cyclopentene was done in the 1960's by multiple groups.[117,118] Natta was the first to recognize PPR's ability to undergo SIC and determine its crystalline structure using X-ray scattering techniques.[117] Later Kraus showed that crystalline domains of PPR make up less than 10% of the total volume, similar to that of NR.[119] More interestingly, Tucker showed that by altering the *cis/trans* ratio PPR's thermal properties, and therefore SIC, can be widely tuned.[120] After these initial reports PPR research went dormant. Recently however, there has been renewed interest due to its synthetic versatility.[121]

Since the early days of PPR research, advancements in synchrotron facilities now allow real-time monitoring of SIC via WAXS. This technique has been widely used to characterize the SIC of NR[116,122–126] and recently we applied these methods to study the SIC behavior of a high-*trans* PPR (having *cis/trans* ratio = 17/83).[127] We found that SIC is a major contributor to strain-hardening of PPR between -10 °C and 25 °C. This temperature range shows promise for tire applications; however, the relatively high crystallization temperature (T_c) of the high-*trans* PPR (-25 °C) means that traction properties at or below this temperature will be poor. Increasing the *cis* content improves PPRs low temperature performance by lowering T_c, however it also lowers SIC reducing its mechanical strength. If an alternative strengthening method, for example branching, could be developed then the PPR rubber would be useful across a broader range of temperatures.

Topology greatly effects mechanical properties. This has been well described in literature for many chain architectures including linear, short and long-chain branched, hyperbranched, cyclic, comb, bottlebrush, dendritic, and star polymers.[128,129] The effect of branching on polymer properties is dependent on both branch density and branch length. Generally, shorter branches interfere with crystallization and make the material more amorphous while long-chain branching doesn't interfere with crystallization as branching chains are long enough to participate in lamellar packing.[130,131] Industrially, branching has been most notably adopted in the modification of polyethylene (PE). The linear version of PE forms high density polyethylene (HDPE) which is stiff and highly crystalline while the branched version of PE forms low density polyethylene (LDPE) which is more ductile and less crystalline. In the melt-state however, branched PE is actually stronger than linear PE due to greater effective entanglement density.[131] Because PPR, and elastomers in general, are used at service temperatures above their melting point (T_m), we hypothesized that adding branches would increase strength as elastomers are in their "melt-state" during use. Vulcanization makes the elastomer act like a solid by preventing flow and preserving its shape at rest, but when stretched polymer chains can easily rearrange acting like a liquid. Branching units should hinder this rearrangement increasing the strength/stiffness of the material.

Herein we study the effect of long-chain branching (LCB) on *trans* PPR. Ultimately, we are interested in exploring the use of branching units to alter PPR's mechanical properties, but this study also provides us the opportunity to study how topology affects chain dynamics and impacts SIC. To this end, we synthesize and evaluate a branched PPR alongside its linear counterpart. We then characterize the extent

of branching and its effect on the thermal and rheological properties. We further test their mechanical properties while monitoring their chain dynamics to understand LCB's effect at the molecular level.

4.3 Experimental

4.3.1 Materials and methods

Commercial cyclopentene monomer (96%) and anhydrous toluene (Sigma-Aldrich) were additionally purified by degassing and passing through an activated alumina column. Dicyclopentadiene (Sigma-Aldrich) was purified by dissolving in toluene (1:1, v:v), and degassing and passing the resulting solution through an activated basic alumina column. Tungsten (VI) hexachloride, triethylaluminum and 2,6-di-*tert*-butyl-4-methylphenol were purchased from Sigma-Aldrich and used as received. The generation of catalyst solutions and polymerizations were carried out under nitrogen atmosphere using glove-box or Schlenk techniques. Neat triethylaluminum (CAUTION: extremely pyrophoric material) was diluted with toluene (at least 90 wt. % of toluene) in a glovebox before transferring into the polymerization reactor.

4.3.2 Linear PPR synthesis

The general synthesis of linear PPR was previously described.[127] In short, the polymerization pre-catalyst was prepared by adding solid $(4\text{-}MeC_6H_4O)_2AlCl$ (1.05 g, 3.77 mmol) to a solution of WCl_6 (0.75 g, 1.89 mmol) in toluene (20 mL). After stirring for 60 min at 25 °C, the resulting mixture was added to a solution of cyclopentene (CP) (250 g, 3.671 mol) and triethylaluminum (432 mg, 3.79 mmol) in toluene (900 mL) at 0

°C. The reaction mixture was stirred using mechanical agitator for 3 h at 0 °C. Then, a solution of 2,6-di-*tert*-butyl-4-methylphenol (1.00 g, 4.48 mmol) in ethanol (20 mL)/toluene (100 mL) was added to quench residual catalyst and alkyl aluminum. The obtained mixture was added to methanol (1.5 L) under intense mechanical mixing. The precipitated polymer was washed three times with ethanol (500 mL) and dried under vacuum at 50 °C for 4 h. Yield: 228 g (91%).

4.3.3 LCB PPR synthesis

The pre-catalyst was formed by adding solid $\{4\text{-}(PhCH_2)C_6H_4O\}_2AlCl$ (0.87 g, 2.02 mmol) to a solution of WCl_6 (0.40 g, 1.01 mmol) in toluene (20 mL). After stirring for one hour at ambient conditions, the resulting mixture was added to a solution containing cyclopentene (major comonomer, 275 g, 4.035 mol), triethylaluminum (activator, 230 mg, 2.02 mmol), and toluene (2200 mL) at 0 °C. A solution of dicyclopentadiene (DCPD) (minor comonomer, 3.6 g, 27.3 mmol) in toluene (15 mL) was slowly added to the polymerization mixture over 60 min under intense mechanical stirring. After an additional 2 h, a solution of 2,6-di-*tert*-butyl-4-methylphenol (1.00 g, 4.48 mmol) in 100 mL of ethanol/toluene mixture (1:4, v:v, respectively) was added. The obtained mixture was then poured into methanol (4 L). The precipitated polymer was washed with methanol (500 mL × 3) and dried under vacuum at 50 °C for 4 h to give 139 g of the final product. Yield: 50 %. DCPD incorporation: 1.7 mol% (CP:DCPD = 57:1).

4.3.4 PPR vulcanization

Vulcanized PPR samples were prepared in two steps using the compounding recipe shown in Table C.1. First, the components were mechanically mixed at 80 °C using an internal (Brabender^{TM}) mixer. The compounds were then molded into plaques with a thickness of 0.5 mm and cured at 160 °C for 25 min using a hot press. This curing time was sufficient to achieve 90% of the ultimate cure according to the vulcanization curve data measured in an ARES G2 rheometer (TA Instruments^{TM}). The vulcanization curves are shown in the Supporting Information (Figure C.10). Dogbone-shaped specimens with dimensions 15 mm × 3 mm × 0.5 mm were cut from the plaques and used for the tensile tests and X-ray scattering measurements.

4.3.5 Characterization of non-crosslinked polymers

Cis/trans mole ratios of CP units and CP/DCPD comonomer mole ratios were determined by ^{13}C and ^{1}H nuclear magnetic resonance (NMR) spectroscopy. Weight average molecular weight (M_w, light scattering MW), dispersity (Đ, from conventional Mw/Mn), and branching index (g', with K= 0.000521 dL/g and a = 0.676 for linear polymer reference) were determined by gel permeation chromatography (GPC). Glass transition temperature, melting temperature and crystallization temperature (T_g, T_m, T_c) were identified by differential scanning calorimetry (DSC). The results of these characterizations are summarized in Table 4.1 and details of each technique will follow.

Table 4.1 *Material properties for linear and long-chain branched PPR*

	Linear	**LCB**
cis/trans mole ratio	17/83	19/81
CP/DCPD mole ratio	100/0	57/1
M_w, kg/mol	254	401
Đ (M_w/M_n)	2.03	2.97
g' (average)	0.97	0.87
T_g, °C	-97.9	-93.4
T_m (peak), °C	7.1	6.6
T_c (onset), °C	-21.8	-23.7

NMR spectroscopic data of polymers were recorded at 25 °C using a 600 MHz Bruker Avance IIIHD NMR spectrometer. Samples were prepared by dissolving the polymer in $CDCl_3$ and filtering this solution into a 10 mm NMR tube using $CDCl_3$. Note that the filtration was carried out to remove traces of catalyst residue, including aluminum hydroxide and tungsten oxide. Characterization of compositions including *cis/trans* ratio and CP/DCPD copolymer assignments were based on previous reports.[132,133] The NMR Spectra used to generate these values can be found in Figures C.6-9.

A triple-detector GPC equipped with a differential refractive index detector, an 18-angle light scattering (LS) detector, and a 4-capillary viscometer was used. Three Agilent PLgel 10-μm Mixed-B LS columns were used to provide polymer separation. HPLC-grade THF solvent was used as the mobile phase. The nominal flow rate and injection volume were 0.5 mL/min and 200 μL, respectively. The whole system including transfer lines, columns, and viscometer detector were contained in ovens maintained at 40 °C. The polymer was dissolved at 40 °C with continuous shaking for about 2 h.

DSC scans were performed using a DSC2500^{TM} (TA Instruments) in a heat-cool-heat cycle between -140 and 40 °C with a 10 °C/min heating and cooling rate. DSC scans can be found in Figure C.1.

Rheological measurements were performed using 1 mm thick plaques of unvulcanized PPR samples. Plaques were molded using a hot press equilibrated at 80 °C and subsequently cut into 25 mm discs. Dynamic frequency sweep (DFS) measurements were performed at 80 °C under nitrogen atmosphere using a strain-controlled ARES-G2 rheometer (TA Instruments^{TM}) with 25 mm parallel plate geometry. The frequency range used for the DFS measurements was 0.01 to 628 rad/s and the strain amplitude was 1 %.

4.3.6 Characterization of PPR rubbers

Morphologies of the PPR samples were examined using a bimodal AFM (Cypher, Asylum Research) after cryo-facing using a cryo-microtome (Leica) at -120°C. Bimodal AFM, where the cantilever-tip ensemble is simultaneously excited at two eigenmodes, was used to deliver enhanced contrast.[134,135] The instrument produces four images, one for each data channel, corresponding to height, 1st phase shift, 2nd oscillation amplitude and 2nd phase shift. Typically, the channel image with best contrast for the specific sample is selected for further analysis. In the case of the PPRs, the height channel was selected. Rubber performance was characterized by tensile testing combined with *in situ* WAXS measurement. A tensile stage (Linkam TST350^{TM}) equipped with a 200 N load cell was used for the tensile tests performed at two different temperatures (0 and 40 °C) unless otherwise noted. The Linkam stage was mounted in 12-ID SAXS beam line at the Advanced Photon Source (Argonne National Laboratory). The energy of the X-ray was

13.3 keV and the beam size was 500 μm × 500 μm. Two-dimensional WAXS patterns were collected using a Perkin Elmer detector and calibrated for q space by using silver behenate as a standard. After loading in the Linkam, the samples were equilibrated at the measurement temperature for at least 5 min. The dog-bone specimens were stretched at a linear deformation rate of 100 μm/s, which corresponds to a strain rate of $6.7 \times 10^{-3} \cdot s^{-1}$. Two second exposure times were used to generate WAXS images during stretch and retraction. Maximum stretch was 500% strain and WAXS measurements were taken in 20% strain intervals. The symmetric displacement of the two clamps of the Linkam stage enabled the same location of the sample to be probed during the tests.

Percent crystallinity was calculated by peak deconvolution of 1D scattering plots performed in IgorPro™. A representative curve fitting is provided in Figure C.2. After acceptable fit was achieved, peak areas were calculated and used to calculate percent crystallinity using Equation 4.1.

$$\%\ Crystallinity = 100 \times \frac{\sum Crystalline\ Peak\ Areas}{\sum Amorphous\ and\ Crystalline\ Peak\ Areas} \tag{4.1}$$

To quantify chain alignment during stretch and retraction alignment factor, A_f, was calculated as described by Walker and Wagner.[136] Angular sectors covering two different q ranges were considered in the analysis. The first sector covered the q-range $0.9 < q^*_{\mathrm{Am}} < 1.35$ Å^{-1}, and the second sector covered the q-range $1.4 < q^*_{\chi} < 1.5$ Å^{-1}. These two ranges were chosen to monitor the amorphous halo and the main crystalline peak, respectively (Figure C.3). Alignment factors were calculated from Equations 4.2 and 4.3,

where $I(q^*_{\mathrm{Am}})$ and $I(q^*_{\chi})$ are the integrated intensities in the corresponding q-ranges of interest and ϕ is the azimuthal angle.

$$\mathrm{A_{f,Am}} = \frac{\int_0^{\pi} \mathrm{I}(\mathrm{q}^*_{\mathrm{Am}}, \phi) \cos 2\,\phi \mathrm{d}\phi}{\int_0^{\pi} \mathrm{I}(\mathrm{q}^*_{\mathrm{Am}}, \phi) \mathrm{d}\phi} \tag{4.2}$$

$$A_{f,\chi} = \frac{\int_0^{\pi} I(q^*_{\chi}, \phi)\, cos\, 2\, \phi d\phi}{\int_0^{\pi} I(q^*_{\chi}, \phi) d\phi} \tag{4.3}$$

4.4 Results

4.4.1 Investigated PPR topologies

The two model topologies compared in this study were linear and branched as shown in Figure 4.1. When DCPD was copolymerized with the CP monomer, tetrafunctional branch points were formed as shown in purple. During vulcanization both rubbers underwent crosslinking forming trifunctional branching points shown in pink. We investigated the effect of adding branching points on thermal-mechanical behavior, chain mobility, crystallization kinetics, and morphology.

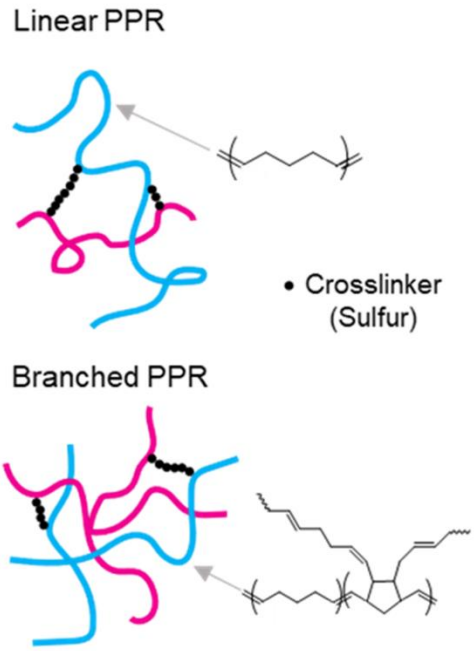

Figure 4.1 *Structure of linear and branched PPR's after vulcanization*

4.4.2 Evidence of LCB formation

LCB formation was verified by GPC and rheology. GPC data was used to determine the branching index by the relation $g' = [\eta]_{avg}/KM_v^{\alpha}$, where [η] is the viscosity, M_v is the viscosity-average molecular weight, and K and α are constants determined by the reference polymer. [137] The branching index of homopolymer CP was nearly 1 (1.01) and did not change as molecular weight increased indicating negligible branching. In contrast, CP/DCPD copolymers had an average branching index much less than 1 (0.81) which decreased as molecular weight increased suggesting significant branching. For more information see Figure C.4.

Further evidence of LCB was obtained from rheological data (Figure 4.2). Linear PPR showed typical viscoelastic response of linear polymers, with relaxation time of ~0.3 s, measured as the reciprocal of the angular frequency at moduli crossover (G' = G''). The van Gurp-Palmen (vGP) plot (plot of the loss angle, $\delta = \tan^{-1}(G''/G')$ versus complex modulus, $|G*| = \sqrt{G'^2 + G''^2}$ shown in Figure 4.2b) also showed typical response of linear polymer, approaching terminal regime (δ → 90°). In contrast, LCB PPR showed hindered relaxation due to hyperbranched architecture. This was also evident in the vGP plot of the branched PPR, which showed the typical shoulder at low δ values, characteristic of LCB polymers.[138]

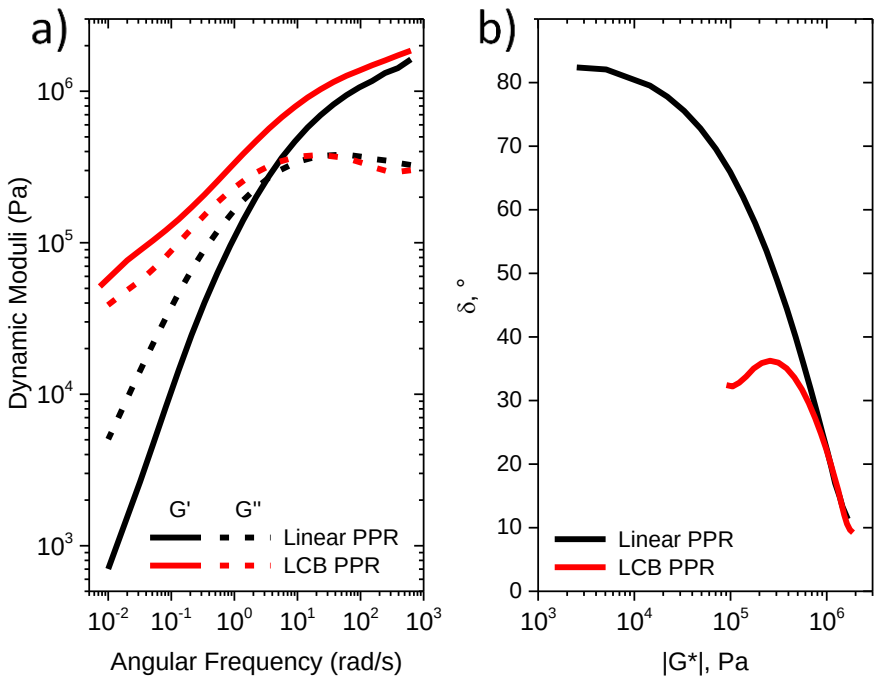

Figure 4.2 *Dynamic frequency sweeps of linear and LCB PPRs*

(a) Elastic and viscous moduli (G' and G'') versus angular frequency. (b) Van Gurp-Palmen plots.

4.4.3 Mechanical performance

Branching dramatically changed the tensile response of PPR. At 500% strain, branched PPR reached a stress (8.23 MPa) over three times greater than its linear counterpart (2.47 MPa) when tested at 0 °C (Figure 4.3a). Below 20% strain, branched and linear PPR displayed comparable mechanical responses. At about this elongation, linear PPR began a downward turn, due in part to narrowing cross sectional area, yet branched PPR showed a linear response indicating strain-hardening behavior. The same materials were tested at 40 °C, about 35°C above their melting points, to measure their elastic response in the absence of SIC (Figures 4.3b-c). At this elevated temperature, branched PPR still exhibited vastly stronger tensile performance showing that this phenomenon is inherent to topology rather than differences in SIC.

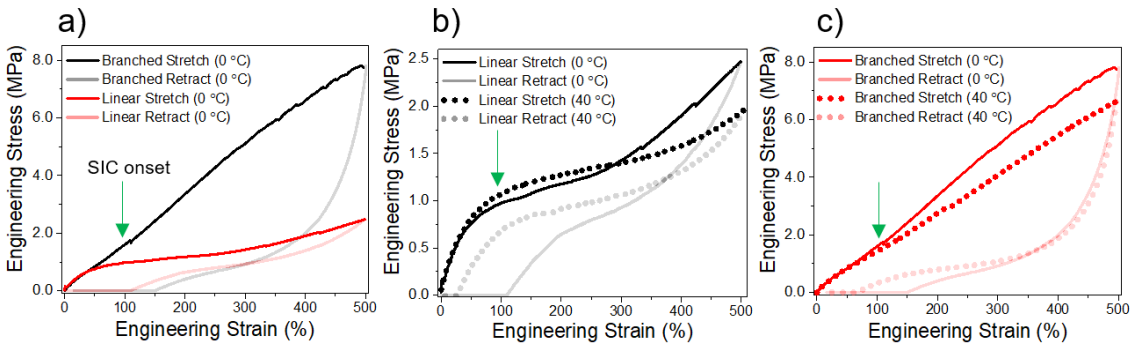

Figure 4.3 *Tensile test comparisons*

a) Linear versus branched PPR at 0 °C. b) Linear PPR with SIC at 0 °C and without SIC at 40 °C. c) Branched PPR with SIC at 0 °C and without SIC at 40 °C.

These results also revealed the differences between the two materials with regard to stress evolution during loading-unloading cycles. Linear PPR (Figure 4.3b) performed very similarly with and without SIC until around 250% strain, about 150% strain past

SIC onset. At this point a sharp upturn in the stress-strain curve was observed. At 400% strain, linear PPR experiencing SIC had a stress-strain slope over twice that of the same material without SIC. Branched PPR (Figure 4.3c) showed a much different response to SIC, with stiffness immediately increasing at the SIC onset. Mechanical hysteresis, characterized by the difference in area below the loading and unloading curves, occurred in all PPRs but was magnified in the branched specimen. Both linear and branched samples showed reduced hysteresis at 40 °C due to the absence of SIC and the supercooling effect.[122] At this temperature, we calculated that hysteresis was 2.5 times larger in the LCB sample than in the linear sample. This showed that branching caused significant energy loss during stretch.

4.4.4 In situ X-ray scattering

Figure 4.4 illustrates how adding branching units affected the WAXS pattern of PPR during a stretch and retraction experiment at 0°C and at elevated temperatures. The experimental set-up used to obtain 2D WAXS images is schematically illustrated in Figure 4.4a. Figures 4.4b, 4.4d, 4.4f, and 4.4h show scattering data taken at 500% strain for linear and branched PPRs at 0 °C when SIC is prevalent, and at elevated temperature where SIC is suppressed. The 2D data (inset) obtained from the detector was transformed into 1D plots showing how intensity changes with scattering vector (q). All samples showed similar amorphous peak positions centered at q = 1.24 $Å^{-1}$. Linear and branched PPRs tested at 0 °C showed a main crystalline peak centered at q = 1.34 $Å^{-1}$, and minor crystalline reflection peaks at q = 1.52, 1.61 and 1.68 $Å^{-1}$. Because the same crystalline peaks appeared in both samples, we concluded that branching units did not impact the

crystal packing structure. When samples were tested at elevated temperatures, crystalline peaks were no longer apparent, indicating negligible SIC occurred at these temperatures as expected. WAXS data during the stretching of branched PPR at 40 °C unfortunately could not be obtained; however, data at 25 °C was successfully gathered showing that even at this lower temperature minimal SIC occurred. From this data we concluded that indeed the mechanical difference between branched and linear PPR observed at 40 °C is not influenced by SIC.

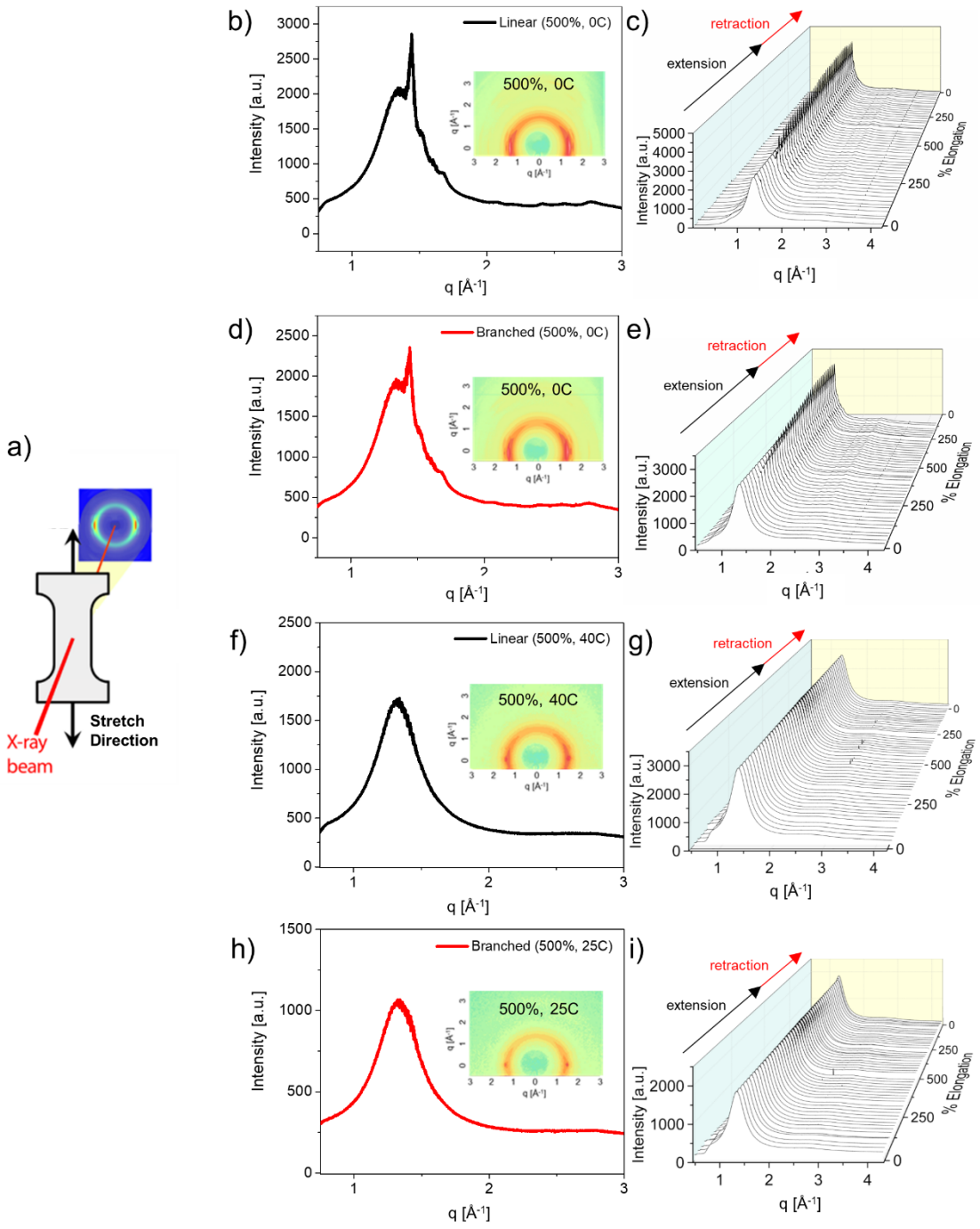

Figure 4.4 *In situ WAXS data*

a) Experimental set-up. b,d,f,h) 1D scattering pattern (2D inset) at 500% strain of linear and branched PPR at low and high temperatures. c,e,g,i) Waterfall plots showing the progression of 1D plots throughout stretch and retraction of linear and branched PPR at low and high temperatures.

Throughout extension and retraction, a total of 50 WAXS images were taken for each specimen. The progression of SIC during the *in situ* stretching experiment can be seen in the waterfall plots of Figures 4.4c, 4.4e, 4.4g, and 4.4i. Three interesting pieces of information were gleaned from these plots. Firstly, at elevated temperatures the formation of crystallization peaks was effectively suppressed. Secondly, at 0 °C crystallization happened more rapidly in linear PPR while branched PPR crystallized much more gradually. Thirdly, at this temperature significant melting never occurred during retraction in either sample until the sample was completely unstressed. Further analysis of the data using fitting software was used to quantitatively compare crystallinity and alignment during deformation. These analyses were limited to those samples tested at 0 °C which showed significant SIC.

Percent crystallinity was calculated as the ratio of the integrated scattering intensity from crystalline peaks to the total integrated scattering intensity (as illustrated in Figure C.2). Figure 4.5a shows the results of these calculations throughout stretch and retraction for both PPRs. Linear PPR crystallized much more rapidly than branched PPR. For instance, between 100% strain (SIC onset) and 140% strain linear PPR increased crystallinity by 2.6%, while branched PPR only increased by 0.2% crystallinity. Branched PPR also reached a lower ultimate crystallization throughout stretch. At maximum strain, linear PPR crystallinity (6.8%) was nearly 20% higher than branched PPR (5.7%). This result suggest that branches impose topological constrains for SIC. This can be rationalized by considering that when a hyper-branched molecule is subjected to uniaxial deformation, it could be pulled from multiple branching points, and potentially in multiple directions. This could hinder the local alignment of the chains and

the concomitant nucleation of crystalline domains. In the case of linear chains, the chains have more freedom to rearrange facilitating local chain alignment and crystal nucleation and growth.

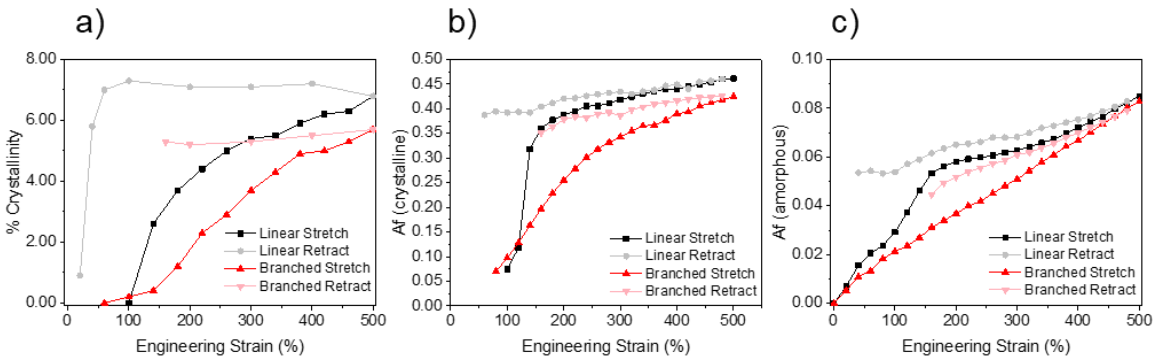

Figure 4.5 *WAXS data for linear and branched PPR plotted vs strain*

All data taken at 0 °C. a) Crystalline growth monitoring through stretch and retract. b) Crystalline alignment factor through stretch and retraction. c) Amorphous alignment factor through stretch and retraction.

During stretch, chains rearrange and orient themselves with the stretching direction. WAXS scatting patterns contain information about chain orientation that can be extracted by azimuthal analysis, using the alignment factor (A_f) expressions (Equations 4.2 and 4.3). The A_f takes values ranging from 0 to 1, with $A_f = 0$ indicating average random orientation of local chain segments, and $A_f = 1$ represents all chains being parallel to the stretch direction.[136] Depending on the q region being monitored the alignment of amorphous and crystalline regions can be investigated separately (see experimental section for details).

Figures 4.5b and 4.5c show how crystalline and amorphous alignment proceeded for linear and branched PPRs. Two regimes of crystalline alignment were observed in both samples (Figure 4.5b). During the first regime, rapid crystallite alignment occurred

between 80 and 140% strain in the linear PPR, while the branched PPR aligned about three times slower in this region. In the second regime, the rate of crystal alignment decreased, and the level was comparable for both samples. Amorphous alignment (Figure 4.5c) told a similar story. Linear PPRs displayed rapid alignment in the early stages of SIC, whereas branched samples did not. The result confirmed the postulate proposed above that the hyperbranched topology hinders local chain alignment, which in turns impedes crystal nucleation during uniaxial deformation. Therefore, it raises the question: if SIC is weaker in branched PPR, then what is the origin of the substantial tensile strengthening shown in Figure 4.3?

4.4.5 Discussion

It is clear from the stress-strain curves that branching produces strain-hardening behavior, but it is unclear why. In previous works, the origins of strain-hardening behavior have been widely debated. Treloar argued that strain-hardening behavior could be explained solely by accounting for finite extensibility of the chains,[139–141] while Flory,[142] and later Mark,[143] argued that SIC is the main contributor, as it results in local crystalline domains acting as additional crosslinks at higher strains. Since these early works, many others have shown a strong correlation between SIC and strain-hardening.[26,144] Our data does not appear to fit either of these theories. We observed strain-hardening in branched PPR at very low strains (≈20%) where finite extensibility typically does not come into play, as well as at elevated temperature where SIC was suppressed.

Simultaneous review of the data (Figure 4.6) suggests a probable mechanism by which branching affects deformation and provide a theory as to why. Figures 4.6a and 4.6b show how stress, crystallinity, and amorphous alignment simultaneously react to strain in linear and branched PPRs respectively. These figures have been divided into 3 regions. Region I (blue) indicates the region prior to SIC. Region II (green) indicates the region of rapid crystallization. Region III (yellow) indicates slower crystallization. Figures 4.6c and 4.6d illustrate two proposed explanations for the observed differences and are discussed in the following sections with respect to 3 key insights from the data.

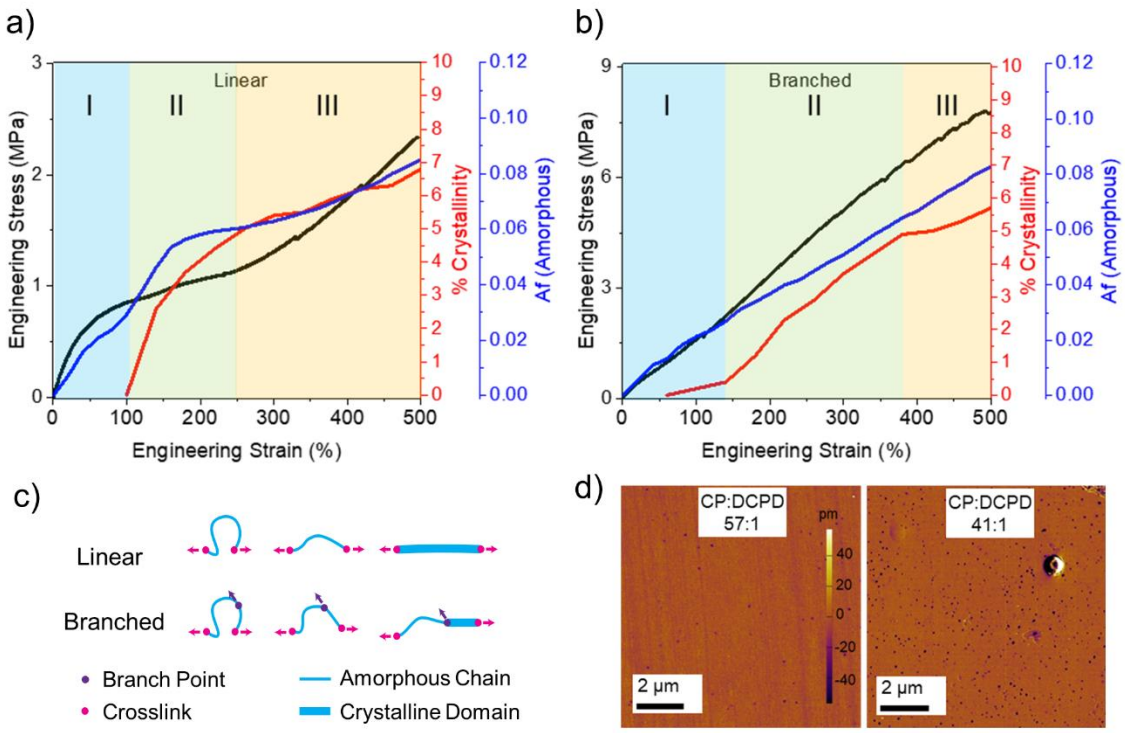

Figure 4.6 *Difference between linear and branched PPR*

a-b) Summary data comparing how stress, crystallinity, and amorphous alignment relate to strain at 0° C for linear and branched PPR, respectively. c) Proposed effect of branching addition on single chain movement during stretch. d) DCPD phase separated nanodomains that may be providing a nanofiller effect.

(1) DCPD addition restricts chain mobility (either by entanglements or nanofiller effect) prompting strain-hardening due to finite chain extension to occur continuously throughout the stretch.

Linear PPR shows a downturn in stress in region 1 (Figure 4.6a) that is not observed for branched PPR. We conclude that strain-hardening in branched PPR is responsible for preventing this downturn. Because this occurs in the absence of SIC the likely cause is finite chain extensibility. Finite chain extensibility, however, is typically not observed until it is stretched passed a few hundred percent strain. So why in branched PPR do we see this behavior so early? One possibility is that branched PPR chains have more constraints on them and thus sections of chain become fully extended earlier in the stretch (Figure 4.6c). Another possibility is that hard, phase separated, DCPD domains act as nanofillers restricting chain movement. Nanofillers are known to greatly effect elastomer mechanical performance and typically show similar stiffening behavior as we observed here.[145] Nanodomain like features were observed in these materials via AFM and become more prominent with increasing DCPD content (Figure 4.6d). The density of such nanodomains also increased when all of the DCPD monomer was added at the beginning of the reaction rather than slowly throughout (Figure C.5). With instantaneous addition of DCPD, we postulate that our copolymer would be blockier than with slow addition allowing greater phase separation to occur. Our reasoning is that DCPD is more reactive than CP and should add to the chain first. Similar observations have been made with other CP copolymerizations.[146]

Whether the reduced chain mobility is caused by branching points or by an unintended nanofiller effect cannot be distinguished from our current data. Therefore, in the remaining discussion we will not attempt to deconvolute their individual effects, but rather discuss branched PPR as a rubber possessing decreased chain mobility.

(2) Branching does not affect the onset of SIC, but it does affect the onset of strain-hardening due to SIC.

Both branched and linear PPR show WAXS crystalline peaks forming around 100% strain at 0 °C, marking the onset of SIC. At this point an immediate upturn in stress is present in the branched sample which is undoubtedly due to SIC because it did not occur when the branched sample was tested at 40 °C. Alternatively, the linear sample, despite undergoing faster SIC, does not show an upturn from SIC until much later in the stress strain curve (≈ 250%). Therefore, it begs the question: why is the mechanical impact of SIC instantaneous in the branched specimens, but delayed in the linear ones? We hypothesize that the branched PPR's chains have so little mobility to begin with, they are already experiencing some finite chain extension strain-hardening when SIC occurs. Then SIC magnifies the finite extensibility by reducing mobility further. Linear PPRs show a delay in the SIC stress response because at 100% strain the chains are still highly mobile and far from experiencing finite chain extension. SIC lowers the onset of finite chain extensibility, but not enough to be noticed before 250% strain. Thinking of SIC as an event that lowers chain mobility, shifting the effects of finite chain extension to lower strains, may help bridge the arguments of Treloar and Flory discussed earlier.

(3) Low mobility chains (branched) exhibit slower amorphous alignment leading to slower and more steady crystalline growth.

Prior to any SIC (region I), linear amorphous alignment (A_f = .029) is 38% greater than branched (A_f = .021). This is due to branched chains having more points of restriction that hinder alignment. Crystallinity occurs predominantly in aligned amorphous chains, so the effect persists into the kinetics of SIC. Therefore, we see a much slower crystallization rate for branched PPR. Figure 4.6c shows a representation of how we believe this occurs. When a chain between crosslinks is strained, an unhindered segment is free to align in the stretch direction as only 2 forces are acting upon it. A hindered chain however may have multiple forces acting upon the chain preventing it from fully aligning, and crystallizing. Alternatively, it is possible that phase separation, and the resulting nanofiller effect, is the culprit of reduced amorphous alignment. In either case our data suggests that lower mobility chains reduce amorphous alignment and slows the crystallization process.

4.5 Conclusion

This work investigates the molecular mechanisms leading to the significant increase in mechanical performance observed in branched PPR, compared to linear PPR. Through use of WAXS, we found that even in the absence of SIC, this trend remains true. The origins of this behavior remain unclear, although our data suggests that reduced chain mobility in branched samples is a likely factor. Under conditions where PPR

experiences SIC (0 °C), we found that branched PPR crystalizes at a more constant rate and to a lesser extent than linear PPR. We further found that amorphous alignment is slower in branched samples explaining the slower SIC kinetics. AFM data suggests that some of these effects may be coming from unintended filler effects caused by formation of glassy DCPD domains. The properties exhibited by LCB PPR show promise, especially in high temperature conditions where SIC cannot occur. However, further work is needed to fully understand the intriguing structure property relationships observed in this material.

CHAPTER V – POLYPENTENAMER THERMOPLASTIC ELASTOMERS VIA COPOLYMERIZATION OF CYCLOPENTENE AND DICYCLOPENTADIENE

Portions of the text in this chapter have been reprinted with permission from:

Weller D.W., Halbach R., Zabula A.V., Gu X., López-Barrón C.R.

Submitted to ACS Applied Polymer Materials 2021

5.1 Abstract

Dicyclopentadiene (DCPD) monomer was incorporated at various levels into statistical copolymerizations with cyclopentene (CP) to determine its influence on the resulting copolymers. We characterized the thermal, viscoelastic, mechanical, and morphological changes upon adding DCPD and determined its strengthening mechanism. DCPD units formed branching points along the polymer that phase separated into glassy domains. These glassy nanodomains acted as physical crosslinks providing strength to the uncured network. Increases in elastic modulus and viscosity were proportional to DCPD content, and at high levels of DCPD thermoplastic elastomer (TPE) mechanical behavior was observed. This work demonstrates that DCPD copolymerization can be used to predictably increase the uncured strength of polypentenamers and at higher loading levels could find use as a TPE.

5.2 Introduction

Elastomers are a class of soft, highly deformable materials. Elastomeric properties derive from an entropic effect that occurs when a network of long, flexible, chains become deformed.[147] Typically, elastomers are used well above their melting temperature (T_m) where large-scale chain rearrangement is possible, allowing extreme deformability before rupture. Elastomers typically employ a crosslinking strategy which lock a few places along each chain in place. Such crosslinking can be of physical or chemical nature (or a combination of both). When stretched, crosslinks prevent chains from relaxing into a coiled structure, preserving the network structure and allowing the material to be stretched repeatedly without much permanent deformation.[148] It has been shown that the mechanical response of an elastomer is largely dictated by its network topology including molecular weight between crosslinks, crosslink functionality, entanglement density, and number of dangling ends.[149]

Polypentenamers, formed by the ring opening metathesis polymerization (ROMP) of cyclopentene (CP), are a versatile class of elastomer that first gained attention for their potential as a natural rubber replacement. Originally discovered by Eletterio,[150] and further developed by Natta et al.,[117] polypentenamers can be synthesized to a primarily *trans* configuration using tungsten based catalysts or a primarily *cis* configuration using molybdenum based catalysts. Tucker et al. later showed that the thermal properties, and therefore strain-induced crystallization properties, could be vastly tuned by altering *cis*-*trans* ratios.[120] High *trans* polypentenamer has been most widely studied because its thermal properties are similar to that of natural rubber ($T_m \approx 18$ °C), and it also has better abrasion resistance, processability, and can withstand high loading levels of filler.[151] *Cis*-

polypentenamer has much lower melting temperature and therefore remains soft and flexible even in extreme environments, however its mechanical properties, including its ability to undergo strain-induced crystallization, are diminished.[152]

Dicyclopentadiene (DPCD) also undergoes ROMP with tungsten-based catalysts. DCPD differs from CP monomer in that it can ring open twice forming two branches at every linkage. When polymerized alone, DCPD forms a rigid crosslinked network. DCPD has been used industrially for reaction injection molding applications for its high modulus, impact strength, and creep resistance.[153] As we have shown previously, copolymerizing CP and DCPD monomer created a branched polypentenamer rubber with increased tensile strength and modulus, but it was suspected that phase separation, not branching, caused the improved properties.[154]

Branching is commonly used to tune material properties and its effects have been studied for many different chain architectures.[128,129] In polyolefins, branching is known to reduce crystallinity, resulting in lower modulus and tensile strength.[155,156] These effects are most obvious when short, densely packed, chains are employed.[130] As the chains become longer, the branches themselves may participate in crystallization/entanglement and the properties approach those of linear polymers. We therefore concluded that the increase in mechanical performance observed in DCPD containing samples was not due to branching. Instead, we concluded that nanophase separation of hard DCPD domains strengthened the polypentenamer by physical crosslinking, as well as acting as a nanofiller.

Fillers such as carbon black or silica are extensively used as reinforcement in elastomers and have been thoroughly studied.[157,158] Fillers are primarily used in tire

formulations to increase strength, modulus, abrasion resistance and to decrease cost. The strengthening mechanism is believed to come from restricted rubber movement due to a combination of hydrodynamic effects, filler-rubber interactions, and filler-filler interactions.[159]

Physical crosslinking, like chemical crosslinking, connects discreet polymer chains to form an interconnected network providing improved strength, modulus, and elastic recovery. Physical crosslinks differ from chemical crosslinks in that they do so using covalent bonds and can therefore be reprocessed at temperatures where the physical crosslinks dissociate. These types of elastomers are known as thermoplastic elastomers (TPE). TPE's are composed of polymer chains containing both hard and soft segments. The soft segments provide the elastomeric behavior while the hard segments undergo intermolecular association creating physical crosslinks. Commonly ABA triblock copolymers are used, however other types of TPE's are made with a statistical incorporation of hard copolymer. These "segmented" TPEs can contain more than 50 blocks.[160]

Up until now it was unclear whether the stiffening effect of DCPD was due to a nanofiller effect, or whether it was due to physical crosslinks. Herein we systematically explored the impact DCPD content has in uncured, trans-polypentenamers. We were able to observe clear trends relating DCPD content to changes in mechanical performance, thermal transitions, crystallization behavior, and morphology. This study suggests that the major strengthening mechanism is physical crosslinking.

5.3 Experimental

5.3.1 Materials

CP monomer, DCPD monomer, and anhydrous toluene (Sigma-Aldrich) were further purified by degassing and passing through an activated alumina column. DCPD was first dissolved in an equal volume of toluene before purification. Tungsten (VI) hexachloride, triethylaluminum, and 2,6-di-*tert*-butyl-4-methylphenol (Sigma-Aldrich) were used as received. All polymerizations, as well as catalyst generation, were carried out under nitrogen atmosphere using glove-box or Schlenk techniques. Neat triethylaluminum (CAUTION: extremely pyrophoric) was diluted with toluene to at least 1/10 its weight in a glovebox before transferring into the polymerization reactor.

5.3.2 Polymerizations

Polymer samples were generated as described recently.[161] The pre-catalyst was formed by adding solid $\{4\text{-}(PhCH_2)C_6H_4O\}_2AlCl$ (0.87 g, 2.02 mmol) to a solution of WCl_6 (0.40 g, 1.01 mmol) in toluene (20 mL). After stirring for one hour at ambient conditions, the resulting mixture was added to a solution containing CP (major comonomer, 275 g, 4.035 mol), triethylaluminum (activator, 230 mg, 2.02 mmol), and toluene (2200 mL) at 0 °C. Various concentrations of DCPD (minor comonomer) dissolved in toluene were slowly added dropwise throughout the first 60 min of polymerization. After an additional 2 h, a solution of 2,6-di-*tert*-butyl-4-methylphenol (antioxidant, 1.00 g, 4.48 mmol) in 100 mL of ethanol/toluene mixture (1:4, v:v) was added. The obtained mixture was then precipitated in methanol and further washed with methanol three times before being dried under vacuum at 50 °C for 4 h.

5.3.3 Characterizations

^{13}C and ^{1}H nuclear magnetic resonance (NMR) spectroscopy were used to determine the *cis/trans* content of the CP units as well as DCPD content of the copolymers based on previous reports.[132,133] Samples were prepared by dissolving the polymer in $CDCl_3$ and filtering this solution into a 10 mm NMR tube. NMR spectroscopic data of polymers were recorded at 25 °C using a 600 MHz Bruker Avance IIIHD NMR spectrometer.

Gel permeation chromatography (GPC) was used to determine weight average molecular weight (M_w), polydispersity (Đ) and branching index (g'). A triple-detector GPC equipped with a differential refractive index detector, an 18-angle light scattering (LS) detector, and a 4-capillary viscometer was used. Three Agilent PLgel 10-µm Mixed-B LS columns were used to provide polymer separation. HPLC-grade THF solvent was used as the mobile phase. The nominal flow rate and injection volume were 0.5 mL/min and 200 µL, respectively. The whole system including transfer lines, columns, and viscometer detector were contained in ovens maintained at 40 °C. The polymer was dissolved at 40 °C with continuous shaking for about 2 h.

A dynamic mechanical analyzer RSA-G2 (TA Instruments) was used for tensile tests of dog-bone specimens (of dimensions 15 mm x 3 mm x 0.5 mm). The dog-bone specimens were stretched at a linear deformation rate of 100 µm/s, which corresponds to a strain rate of 6.7×10^{-3} s^{-1}. The RSA-G2 is equipped with a force transducer that allows measurements of axial force as a function of strain during uniaxial deformation. The engineering stress is computed as $F(t)/A_0$, where $F(t)$ is the instantaneous force, and A_0 is the initial cross section area of the dogbone specimen.

Differential scanning calorimetry (DSC) was used to determine glass transition temperature, melting temperature, and crystallization temperature (T_g, T_m, T_c, respectively). DSC scans were performed using a DSC2500^{TM} (TA Instruments). Various heating/cooling rates were used to reveal different transitions. The details of each scan can be found where the data is presented below.

Rheological measurements were performed using 1 mm thick plaques of polypentenamer. Plaques were molded using a hot press equilibrated at 80 °C and subsequently cut into 8 mm discs. Dynamic frequency sweep (DFS) measurements were performed at 80 °C under nitrogen atmosphere using a strain-controlled ARES-G2 rheometer (TA Instruments^{TM}) with 25 mm parallel plate geometry. The frequency range used for the DFS measurements was 10^{-3} to 628 rad/s and the strain amplitude was 1 %. Dynamic temperature ramps were performed at a constant frequency of 1 Hz with a heating/cooling temperature of 2 °C/min, using a strain amplitude of 0.1 %.

Small-angle and wide-angle X-ray scattering (SAXS and WAXS) were performed using a Xeuss 2.0 laboratory beamline (Xenocs Inc.) with an X-ray wavelength of 1.54 Å and sample-to-detector distances of 137 mm and 2.5 m, respectively. Diffraction images were recorded on a Pilatus 1M Detector (Dectris Inc.) during an exposure time of 5 min. 2D images were then loaded into IgorPro^{TM} and analyzed using the Nika software package.[107,162] Percent crystallinity was calculated using the multipeak fitting function in IgorPro^{TM} to deconvolute the amorphous and crystalline contributions to the 1D WAXS scattering intensity according to Equation 5.1.

$$\% \, Crystallinity = 100 \times \frac{\sum Crystalline \; Peak \; Areas}{\sum Amorphous \; and \; Crystalline \; Peak \; Areas} \quad (5.1)$$

The long period (L_p), in this case representing the lamellar thickness (amorphous + crystalline), was found from Kratky plots ($I*q^2$ vs q). By plotting the data in this fashion, q_{max} is easily determined and used to calculate the long period from the equation $L_p = 2\pi/q_{max}$.[163]

Morphologies of the PPR samples were examined using a bimodal AFM (Cypher, Asylum Research). The specimens for AFM analysis were prepared by cryo-facing at -120°C using a cryo-microtome (Leica). Bimodal AFM, where the cantilever-tip ensemble is simultaneously excited at two eigenmodes, was used to deliver enhanced contrast.[134,135]

5.4 Results

To investigate the impact of DCPD content on polypentenamer properties, we copolymerized CP with varying amounts of DCPD. Each DCPD monomer unit that is incorporated into the polypentenamer backbone can ring open to create 2 branches as shown in Figure 5.1. In addition to branching these units can phase separate forming hard nanodomains that act as both physical crosslinks and nanofiller.

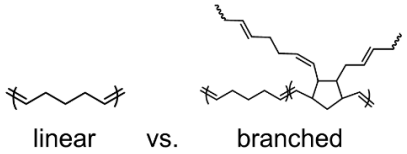

Figure 5.1 *Chemical structures of linear and branched polypentenamers*

5.4.2 Polymer Characterizations

Four copolymers were synthesized for this study with DCPD content ranging from 0.6 mol % to 21.3 mol % as well as a linear polypentenamer control (Table 5.1). Care was taken to ensure that the cis/trans contents were all equivalent as this greatly effects the thermal properties of the polymer. We also tried to keep molecular weight (MW) and dispersity (Đ) constant but unfortunately there was significant variation in the MW. Despite this, the trends in the properties with DCPD content remained clear as shown below. The branching index (g') is a measure of the degree of branching where a value of 1 represents a linear polymer, and this value is reduced as branching increases. The g' value is calculated from the GPC data by the relation $g' = [\eta]_{avg}/KM_v^{\alpha}$, where $[\eta]$ is the viscosity, M_v is the viscosity-average molecular weight, and K and α are constants determined by the reference polymer.[137] The values in Table 5.1 were acquired from the previously reported NMR [161] as well as GPC analysis (Figure D.1).

Table 5.1 *Comparison of polymer characteristics*

DCPD (mol%)	**cis/trans ratio**	**M_w (kg/mol)**	**M_w/M_n (Đ)**	**g' (vis avg)**
0.0	18/82	285	1.85	1.00
0.6	18/82	346	2.18	0.96
3.3	19/81	776	2.15	0.91
6.6	19/81	1072	2.27	0.87
21.3	19/81	541	1.81	0.87

5.4.3 DCPD impact on mechanical properties

Previous work done by our group showed that DCPD incorporation increased the strength and modulus of vulcanized polypentenamer rubbers.[154] Phase separated DCPD

domains acting as nanofiller were believed to be the main contributor to the increased mechanical properties. We expand on this work here by evaluating uncrosslinked (green) polypentenamers containing a wide range of DCPD content. We chose not to crosslink the rubbers for two reasons. Firstly, to isolate the impact of DCPD content on strength and modulus from the effect of vulcanization (chemical crosslinking). Secondly, to evaluate DCPD's ability to increase green strength, an important characteristic for the manufacturability of certain rubber products (e.g., tires).

Figure 5.2a shows the remarkable effect of DCPD on the green strength of the PPR copolymers. The linear sample with no DCPD showed typical tensile behavior of an uncured rubber, namely, a drop in tensile stress at small strains and no strain hardening. But with increasing amounts of DCPD we observed increases in strength and modulus. At 6.6% DCPD tensile strength was greatly improved while remaining highly stretchable. Note that the maximum strain achievable in the AR-G2 instrument is ~865% and, therefore, the arrows in Figure 5.2a indicate that the maximum stretch before break was not reached and further deformation was possible. For the sample with 21.3% DCPD rupture occurred earlier in the stretch (≈ 450%) indicating that at such large DCPD content, the rubber samples become brittle.

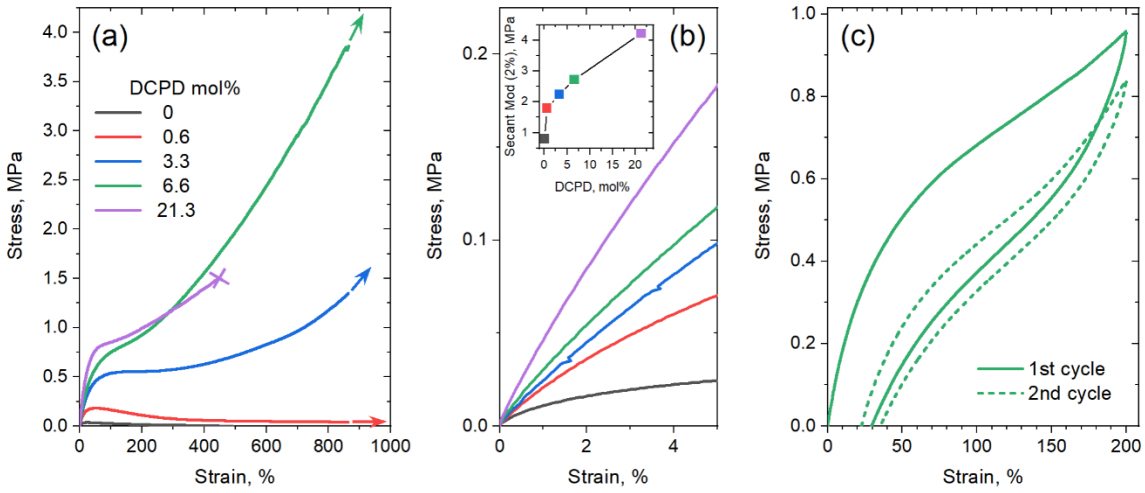

Figure 5.2 *DCPD effect on tensile properties*

(a) Stress-strain curves. The arrows indicate that the maximum deformation before break was not reached for those samples and further deformation is possible. (b) Detail of stress-strain curves in the low strain region and secant modulus as a function of DCPD content (inset). (c) First and second load-unload cycles of the 6.6 mol% DCPD sample.

Figure 5.2b shows a detail of the stress-strain curves up to 5% of strain. In this region, the modulus of each polymer can be seen more easily and demonstrates the stiffening effect of DCPD. The modulus of each polymer (taken at 2% strain) is plotted in the inset. A large increase in modulus was observed going from 0% to 0.6% DCPD, after which modulus increased with DCPD content in a near linear fashion. Note that at such low strain, differences in MW should not influence the modulus.[164]

Further testing of the 6.6% DCPD polymer revealed good cyclic tensile response. Figure 5.2c shows a strain cycling experiment used to evaluate the elastic properties of the sample. After the first stretch to 200% strain the sample achieved 85% recovery. After the second stretch the sample showed a 93% recovery. Compared to general purpose elastomers, the hysteresis is large, but significant recovery after strain shows that the polymers must be physically crosslinked.

5.4.4 Morphology

Room temperature AFM images of the samples revealed nano phase separated hard nanodomains within the soft matrix that increased in density with DCPD content (Figure 5.3). As discussed recently,[154] these nanodomains are aggregates of the DCPD-rich branching units. These aggregates act as physical crosslinks, which explains the elastomeric behavior discussed above in these uncrosslinked copolymers. Phase separation can occur between branched and unbranched domains,[165] or from differences in T_g.[166] Typically random copolymers do not phase separate as the minor component is sufficiently solubilized by its covalently bound neighbors. In this case however, we believe that the more reactive DCPD monomer may form blocky segments increasing the propensity to phase separate.

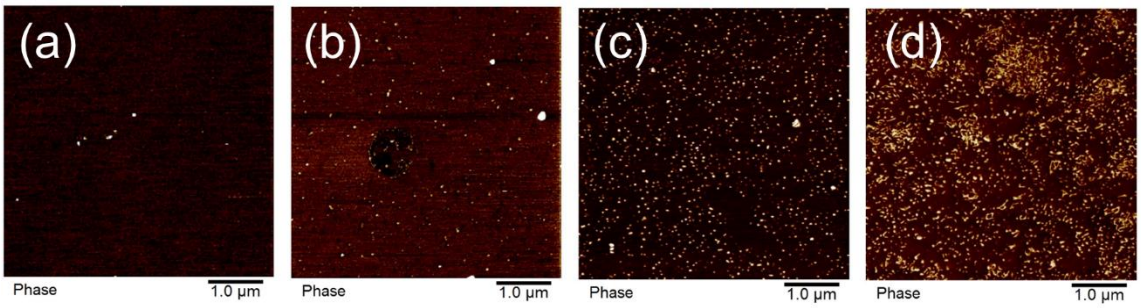

Figure 5.3 *DCPD effect on morphology*

AFM images showing an increasing amount of hard domains with increasing DCPD content. (a) 0.6 % DCPD, (b) 3.3% DCPD, (c) 6.6% DCPD, and (d) 21.7% DCPD.

5.4.5 DCPD impact on thermal properties

DSC scans on the polypentenamers show a strong correlation between DCPD content and their thermal transition temperatures. Under typical heating/cooling scans rates of 10 °C/min, polymers with low DCPD content show strong melting and

crystallization peaks. However, at high levels of DCPD incorporation, crystallization and melting was effectively suppressed (Figure 5.4a). We found that T_g, T_c, and T_m scaled linearly with DCPD content (Figure 5.4b). As DCPD content increases, both T_c and T_m decreases. We hypothesize that physical crosslinks reduce chain mobility therefore frustrating the crystalline packing and shifting T_c and T_m to lower and lower values. Reduced chain mobility also explains increases in T_g with DCPD content, as less mobile chains require more energy before transitioning into the rubbery region.

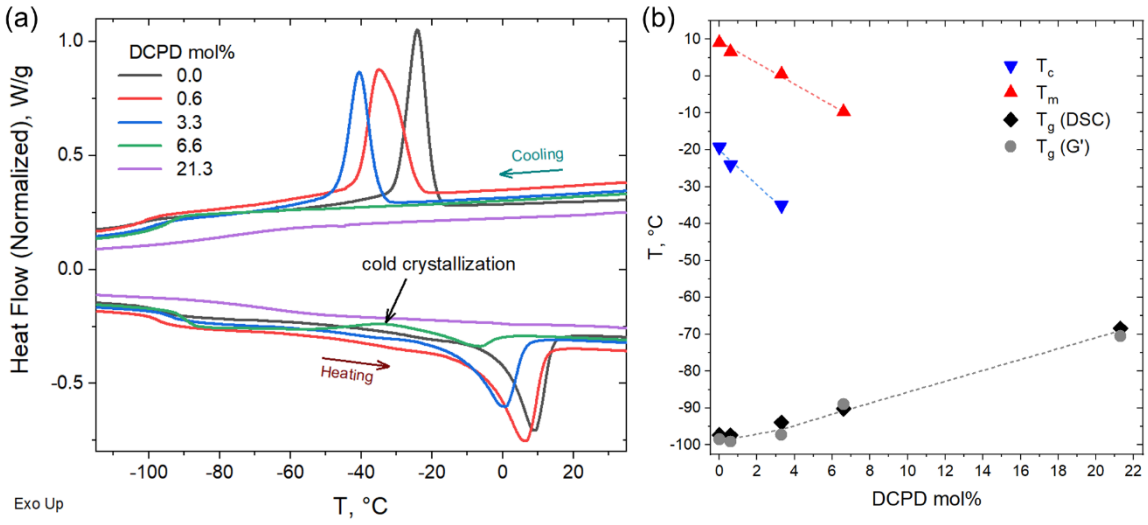

Figure 5.4 *DCPD effect on thermal properties*

(a) DSC heating and cooling curves at 10 °C /min. (b) Thermal transitions as a function of DCPD content.

Evidence of cold crystallization in the heating scan of the 6.6 mol% sample (as indicated in Figure 5.4a) prompted further thermal analysis using dynamic mechanical thermal analysis (DMTA). For this test the samples were loaded in the rheometer in the melt state (at 50 °C) and rapidly cooled down (at a cooling rate of 60 °C/min) to -120 °C, before starting the dynamic temperature ramp to 150 °C at 2 °C/min. Cold crystallization was evident in the DMTA data for the 3.3 and 6.6 mol% samples, as seen in Figure 5.5a.

The substantial decrease in storage modulus (G') marks the glass transition of the polymer. The subsequent increase in G', observed in the 3.3 and 6.6 mol% samples, was a result of polymer crystallization occurring after the polymer chains gain mobility. Further temperature increase led to melting of the crystals, manifested as the second drop in G'. A full description of the DMTA including G'' values are provided in Figure D.2. The cold-crystallization phenomena was verified by DSC measurements using a rapid cooling rate (60 °C/min) and a slower heating rate (2 °C/min) as shown in Figure 5.5b. Cold crystallization in high DCPD content samples shows that DCPD slows the kinetics of crystallization, reinforcing the correlation between DCPD and chain mobility.

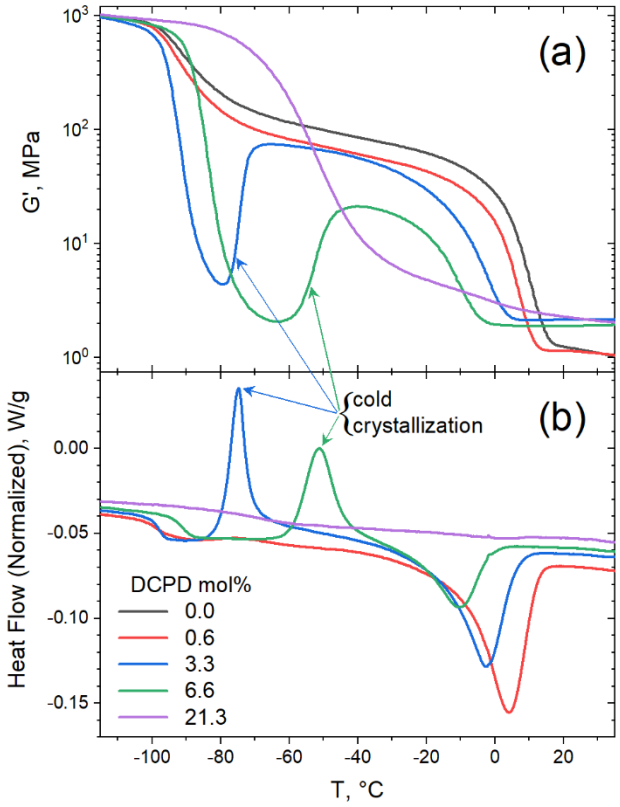

Figure 5.5 *Cold crystallization behavior*

Cold crystallization behavior in moderate DCPD loading levels observed by (a) Dynamic mechanical thermal analysis. (b) DSC after quench (-60 °C/min) and with slow heat (2 °C/min).

5.4.6 DCPD impact on rheological behavior

Rheology was used to get a better understanding of how DCPD incorporation impacted the mechanical response at different time scales. Frequency sweep measurements, as shown in Figure 5.6, demonstrate that branching increased the elastic behavior of the polymers. This is especially apparent when comparing the elastic modulus (G') at low frequencies where the relaxation of the whole chains is proved. Only the linear sample reached the terminal regime, indicated by a slope of loss modulus (G'') approaching a value of 2. In this regime the linear polymer can be considered a viscoelastic liquid. None of the copolymers reach this regime, indicating more elastic behavior. For samples with 6.6 and 21.3 % DCDP, a low frequency plateau can be observed, evidencing solid-like behavior. The same conclusion can be made by examining the tan δ curves, calculated as tan δ = G''/G'. Higher DCPD content polymers had lower tan δ values because they could store energy more effectively as the chain relaxation processes were hindered. The crossover frequency (tan δ = 1) is the point where the viscus and elastic components of a material are equivalent. The two polymers with the highest DCPD content never reach the crossover frequency, demonstrating primarily elastic behavior across all measurable time scales.

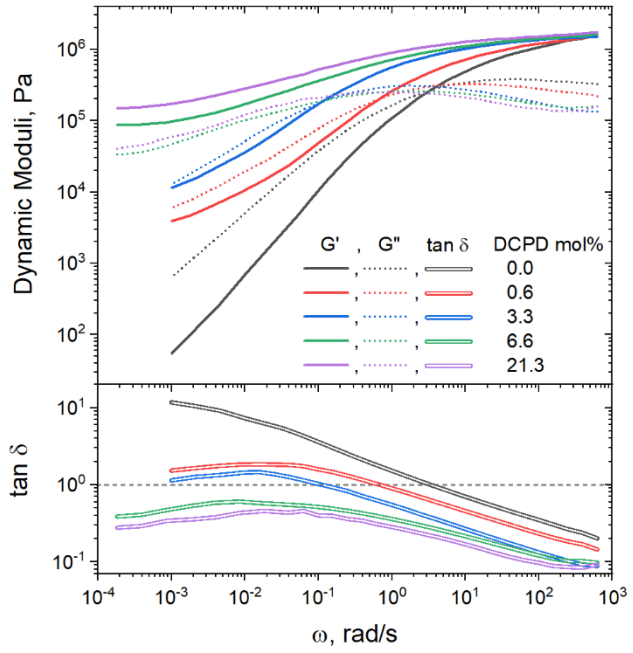

Figure 5.6 *DCPD effect on viscoelastic properties*

Mechanical response during frequency sweeps of polymers with various amounts of DCPD. Tan δ curves calculated from G', G'' measurements. Horizontal dashed black line represents crossover modulus.

The same data can be plotted as complex viscosity as defined as $|\eta^*| = |G^*| / \omega$. Complex viscosity gives a good description of the material's overall resistance to flow, assuming that the Cox-Merz rule is obeyed.[27] As can be seen in Figure 5.7a, the low frequency viscosity increases with DCPD content as expected, indicating improved melt strength. All samples showed shear thinning behavior with viscosities that converge at high shear rates. In this region the test primarily probes local chain dynamics, and the influence of overall chain topology disappears. At slower shear rates we begin to probe the dynamics of larger chain segments. In this region only the linear sample approaches a zero-shear-rate viscosity plateau, whereas all branched samples exhibited an apparent yield stress (ever increasing viscosity at low shear rate).

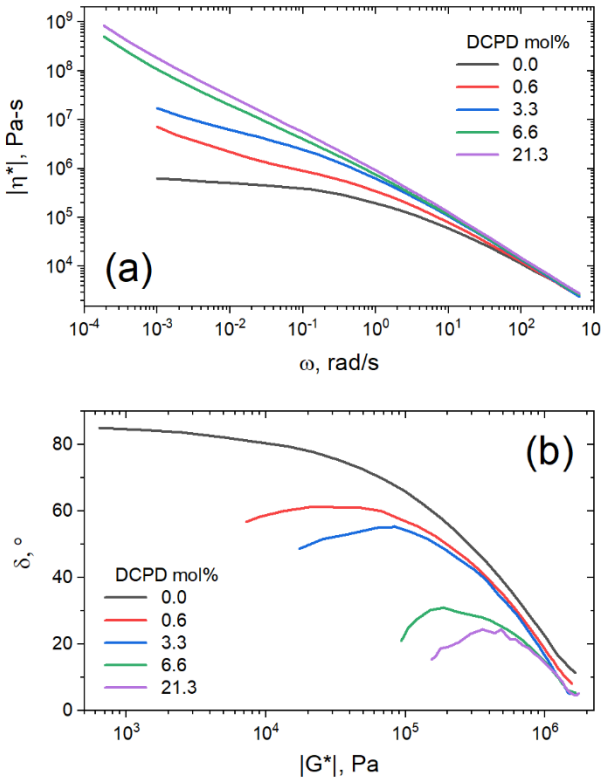

Figure 5.7 *DCPD impact on complex viscosity*

(a) complex viscosity vs. angular frequency. (b) van Gurp-Palmen plots.

The DFS data was reorganized in a van Gurp-Palmen (vGP) plot (Figure 5.7b), a plot commonly used to determine topological differences in polymer architectures.[138] In this plot, phase angle (δ) is plotted as a function of the complex modulus (|G*|). A monotonic decrease of δ with |G*| typically indicates linear polymer architecture, whereas inflection points or peaks suggest branched architectures. Phase angle refers to the phase shift between max stress and max strain in an oscillatory experiment. Purely elastic materials have a phase shift of 0°, as max stress occurs at maximum strain. Alternatively, purely viscous materials have a phase shift of 90°, as max stress occurs at 0

strain where velocity is highest. From this plot it is again apparent that DCPD content increases both the branching and the elastic behavior of the material.

5.4.7 DCPD impact on crystallinity

DSC and SAXS/WAXS were used to determine the effect that DCPD had on the crystallization behavior of the polypentenamers. DSC was performed with heating ramps of 10 °C/min after annealing at -50 °C for 1 hr to compare relative degrees of crystallinity (Figure 5.8). Annealing for 1 hr allowed plenty of time for crystallization to occur, allowing their enthalpy of fusion to be more fairly compared. As expected, the energy required to melt the crystalline domains decreases with higher DCPD content showing a reduced crystallinity in branched samples. It is unclear what is causing the endothermic peak at ~ -40 °C that occurs in three of the copolymers, although we speculate that it may relate to a transition in the DCPD domains, as the intensity increases with DCPD content.

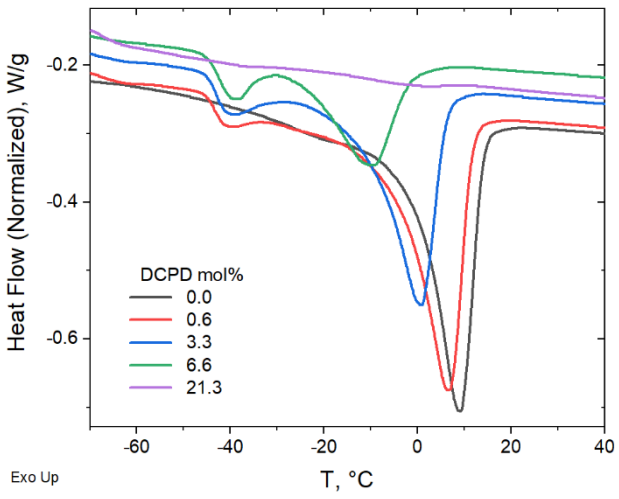

Figure 5.8 *DCPD impact on fusion of enthalpy*

Melting peak endotherms of polymers after 1 hr. annealing at -50 °C to allow full crystallization.

To gain further understanding on the crystallization behavior, WAXS was used to measure crystalline content as a function of temperature. In agreement with the DSC data, we observed that at high levels of DCPD, crystallinity is essentially arrested even at very low temperatures. This can be seen from the comparison of 1D scattering plots taken at -60 °C as shown in Figure 5.9a. At this temperature, a sharp decrease in crystallinity occurs between 3.3% and 6.6% DCPD content. This indicates a critical DCPD content may exist, above which a drastic reduction in chain mobility occurs that prevents crystallization. Prior to this critical concentration crystallinity appears largely unchanged, exhibiting almost identical crystalline peak positions with only a slight reduction in intensity.

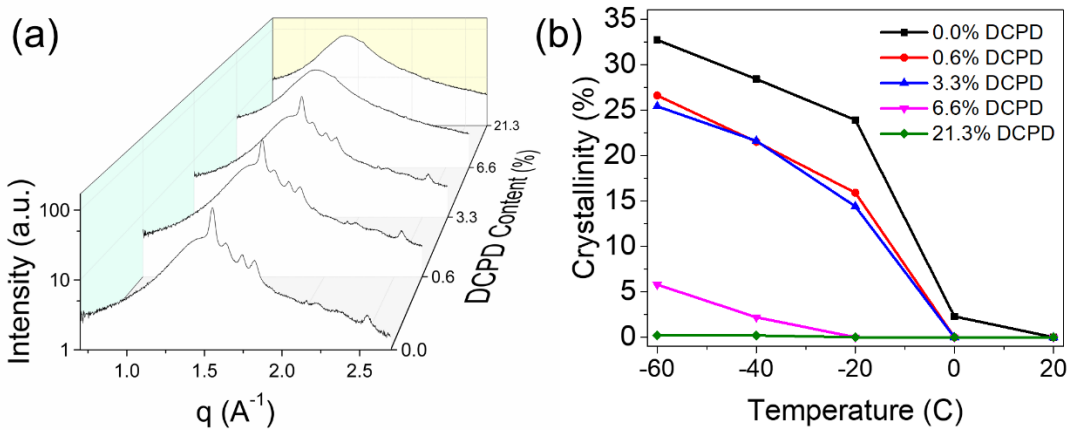

Figure 5.9 *DCPD effect on crystallinity as measured by WAXS*

(a) 1D WAXS plot comparison of polymers with varying DCPD content. All scans taken at -60C. (b) Effect of DCPD incorporation on crystalline content with respect to temperature.

A quantitative description of % crystallinity is possible using the above data by deconvoluting the peaks and comparing the scattering intensity from crystalline and

amorphous source (Figure 5.9b). At $T > T_m$, specifically at 20 °C, all polypentenamers were fully amorphous. At lower temperatures, greater crystallization occurs in samples with less branching. The three samples with the lowest DCPD content underwent rapid crystallization (with respect to temperature) between 0 and -20 °C. As temperature was further decreased, crystallization continued but at a slower rate. Interestingly, nearly all of the differences in crystalline content occurred at the onset of crystallization, between 0 and -20 °C, below this temperature all samples crystallized quite similarly. This suggests that crystallization occurs in two distinct phases. Phase 1, where chain mobility aids in greater crystallization by enabling large scale rearrangement. And phase 2, where chain mobility is restricted due to newly crystalized regions and crystalline growth comes from local rearrangements. A more thorough description of how we calculated % crystallinity as well as the 2D raw data for all measurements are included in Figures D.3-5.

Using SAXS, we were also able to see changes in crystalline structure. We observed that DCPD content increases the long period (L_p) which represents the total thickness of both amorphous and crystalline domains (Figure 5.10). Increases in L_p are likely due to a thickening of the amorphous domain, because DCPD reduced crystallinity. Decreases in L_p with temperature are a result of thermal contraction as well as increased crystallinity. L_p was calculated from Kratky plots and converting the q value at peak intensity to real space. These calculations can be found in Figures D.6-10.

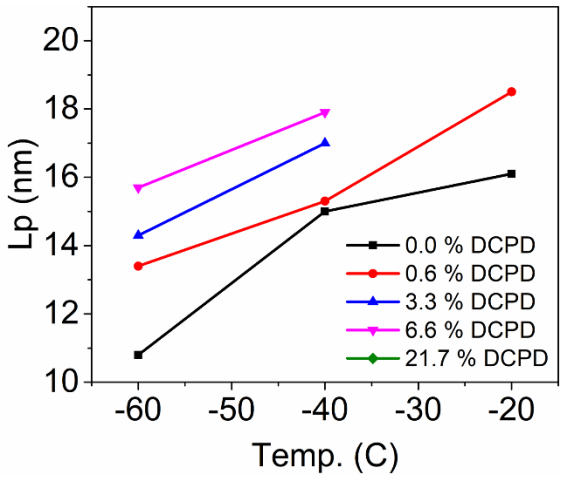

Figure 5.10 *DCPD impact on crystal thickness*

The long period as measured by SAXS increases with temperature and DCPD content.

5.4.8 Discussion

The impact of adding DCPD branching units is clear. DCPD reduces chain mobility which in turn increases elastic behavior and hinders crystallization. The mechanism by way this happens is less clear as branching density, physical crosslinking, and nanofiller content all increase with DCPD content. Branching may be responsible for the viscosity increase observed in the rheological behavior as similar effects have been reported in polybutadiene[167] and polyisoprene.[168] But the increase in tensile strength/modulus suggest a different mechanism. Phase separated domains acting as nanofiller is an attractive theory as it is well known that hard domains within a soft matrix stiffen the material. But nanofillers cannot explain the reversible elastic behavior seen at 6.6% DCPD content. To explain this behavior, we propose that phase separation of DCPD forms glassy domains that act as anchor points along the backbone (Figure 5.11). Even at low DCPD levels (0.6%) a single chain contains ≈ 50 DCPD units that

could aggregate at multiple sites. Following the blue chain of Figure 5.11 we can see that polymers could be interconnected through tie chains between multiple phase separated domains. Loops may also form, providing strong entanglements. It should be noted that each red DCPD unit shown in the figure below may represent a run of multiple DCPD units. The ROMP reactivity of the DCPD monomer is higher than the CP monomer so it is likely there are runs of multiple DCPD units in the chain. Slow addition of the DCPD monomer was performed to promote random copolymerization, but the DCPD was still added in discrete drops. The semi-blocky structure of the copolymer, its mechanical performance, and melt processability, are strong indications that we created a segmented thermoplastic elastomer.[160]

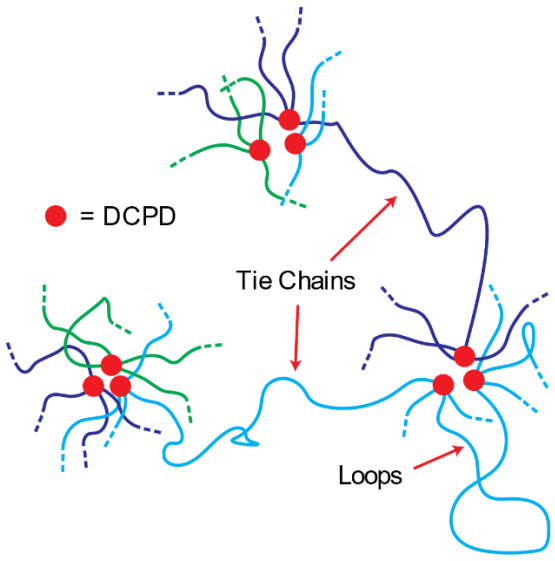

Figure 5.11 *Predicted morphology of DPCD containing copolymers*

5.5 Conclusion

DCPD copolymerization was shown to be a simple way increase the green strength of polypentenamers, as well as be a potential route to creating a new

polypentenamer TPE. DCPD incorporation showed a significant influence on the strength, modulus, elasticity, crystallization, and thermal properties. All measurements pointed to the conclusion that DCPD content decreased chain mobility. In DSC measurements this manifested as increased T_g, decreased T_m and T_c, and reduced crystallization kinetics. In rheology measurements DCPD content correlated to higher elasticity, viscosity, and slower relaxation times. In tensile tests DCPD content increased modulus and ultimate stress. And finally, SAXS/WAXS measurements showed that DCPD content decreased crystallinity and increased crystalline spacing.

The change in properties with DCPD cannot be explained by branching, nor by a filler effect. This study suggests that physical crosslinking in the phase separated DCPD domains is responsible for the changes. The first piece of evidence for this claim comes from AFM, which showed increasing hard nanodomains with DCPD content. The second came from tensile testing which showed high elastic recovery in an uncrosslinked system. Neither branching nor fillers could accomplish this.

CHAPTER VI – CONCLUSIONS AND FUTURE DIRECTIONS

6.1 Copolymer Membrane Research

Utilizing the self-assembled structure of linear diblock copolymers ultrafiltration membranes were created simply by stretching dense BCP films. Upon strain, the minor PEO domains cavitated and elongated to form high aspect ratio pores with an average width ≈30 nm and an average length of ≈110 nm. When proper strain, BCP thickness, and BCP MW were chosen, nearly complete rejection of 40 nm AuNPs (97%) was achieved with a respectable permeability of 960 L/(m^2·h·bar).

Using strain to generate pores rather than etching away the minor domains greatly accelerates the manufacturing process. Typical etching takes hours or days while the stretching process takes less than 30 seconds. Fast, simple, pore generation opens the doors to the continuous production of composite BCP membranes, which are currently made by hand, in a batch process, in low quantities. Developing a scalable manufacturing process for composite membranes such as roll-to-roll printing was the ultimate goal of the research, although it has not yet been achieved.

Future work in this research direction should incorporate the techniques developed in this work into a lab scale roll-to-roll printer to fully demonstrate its scalability. The first steps in this direction were taken in the NVASA research where we constructed a roll-to-roll coater capable of casting ordered BCP films on a substrate, but currently the system does not have the ability to stretch our membranes to generate the pores. I see three routes to overcome this hurdle.

The first is to add a module in the roll-to-roll coater to stretch the membranes after they have been coated and dried. I envision two angled pinch rollers that width of the membrane by stretching the membrane perpendicular to the rolling direction. By adjusting the angle and length of the pinch rollers total strain and strain rate could be changed. Of the options I will discuss, this would require the most engineering but if successful would provide the most impressive result: a single machine that coats a porous film on top of a substrate.

A simpler option would be to break the process up into two roll-to-roll processes. One to cast the film, and the other to stretch the film. The casting process is already pretty well worked out, which just leaves the stretching process left to develop. Because stretching would be performed on a separate machine, strain could be applied parallel to the rolling direction simply by adjusting the tension in the rollers. Higher tension would result in high strain. Although not as attractive as a single roll-to-roll machine, this two-step process may simplify the upfront engineering.

The final, and perhaps easiest option would be to ignore the stretching component of the roll-to-roll machine completely, instead using the pressure of the filtration process to generate the strain. Most membranes are used in combination with a woven spacer intended to provide paths for liquid to travel under the membrane. During the first filtration process the membrane conforms to the shape of the spacer creating local areas of strain. We have already demonstrated that the strain generated by certain spacers is sufficient to generate pores in a dense BCP film but have not fully explored this option. It was difficult to quantify how much strain was being applied by the spacer so for the work presented in Chapter II we stretched the membranes in a machine prior to filtration and

used a flat spacer during testing. This controlled strain approach was helpful in understanding the effects of strain but was not as favorable for roll-to-roll printing. Using a spacer to generate strain a dense BCP layer could be cast on a support using existing machinery, and then the pores would be generated by the spacer during its first filtration. Pore size and pore density could potentially be controlled by adjusting the spacer geometry. 3D printed spacers could be used to evaluate geometry's influence on performance. If successful, the strategy could enable a single membrane to be manufactured whose pore size could be chosen simply by changing out the spacer it is used with.

Aside from making the membranes more manufacturable there is considerable room for improvement of their performance. Under current processing conditions only roughly 15% of the membrane is porous after 20% strain. Further work optimizing the strain rate, as well as investigating biaxial stretching could greatly improve pore density and thus permeability.

BCP membranes hold a lot of promise for improved filtration efficiency due to their highly ordered nanosized domains but cannot yet compete with homopolymer membranes. This is understandable as traditional membranes have had a century of development while BCP membranes just a couple of decades. To make them more competitive, more effort has to go into lowering the cost, and improving the manufacturability of BCP membranes.

6.2 Copolymer Elastomer Research

Copolymerizing DCPD with cyclopentene significantly strengthened polypentenamer tensile strength. In its vulcanized state, the addition of just 1.6 mol% DCPD more than tripled the tensile stress at 500% elongation when compared to the control polypentenamer. This strength is comparable to unfilled natural rubber, which the polypentenamer aims to replace. DCPD segments of the polymer chain phase separated into glassy aggregates that acted as physical crosslinks. These crosslinks were observable even in the unvulcanized state as evidenced by a strong elastic response. Unvulcanized polypentenamers without DCPD a viscous liquid and had no elastic response. Because these materials were still melt/solution processable, the DCPD containing polypentenamers that were created were in fact novel thermoplastic elastomers.

A systematic study of DCPD incorporation at various loading levels in the uncrosslinked material showed that the thermal and mechanical properties could be controlled by changing DCPD content. Higher DCPD content led to higher modulus, tensile strength, and lower crystallization temperature. At high levels of DCPD content (> 6.6 mol%) crystallization was completely arrested. We attribute this behavior to restricted chain movement with increasing physical crosslinks. Restricted chain movement was also observed with increasing DCPD content in the materials viscoelasticity and chain alignment during stretch.

This research showed that polypentenamers may be an effective alternative for natural rubber in tire applications. By copolymerizing with DCPD, two drawbacks of polypentenamers were overcome. Firstly, the cured strength was increased near to that of natural rubber. Secondly, the uncured “green” strength of polypentenamers was greatly

increased which is important for the manufacturing process. Before polypentenamers could be considered a viable replacement for NR, future work clarifying DCPD's strengthening mechanism and chain architecture optimization must occur.

The strengthening mechanism of DCPD was the focus of Chapter V, and although it provided many answers a few critical questions remain. Our past work showed that DCPD aggregates forming physical crosslinks were the main contributor to the strengthening effects. Unfortunately, these physical crosslinks also may be acting as filler which generally provides similar effects. Deconvoluting the effects of physical crosslinking from filler effects is vital to the understanding of why these materials behave the way they do.

Another opportunity for discovery lies in the unique polymerization kinetics of the two monomers. Throughout this paper DCPD was added dropwise throughout the reaction to prevent it from adding all at once due to its higher ring strain. Adding half the DCPD at the beginning of the reaction and the other half at the end of reaction its possible a chain architecture resembling a triblock could be achieved. This could increase the number of active chains reducing the large hysteresis observed in these materials.

Polypentenamers possess many desirable qualities but fall short in a few key areas. Through copolymerization it is possible that the disadvantages can be mitigated so the benefits of these polymers can be fully realized.

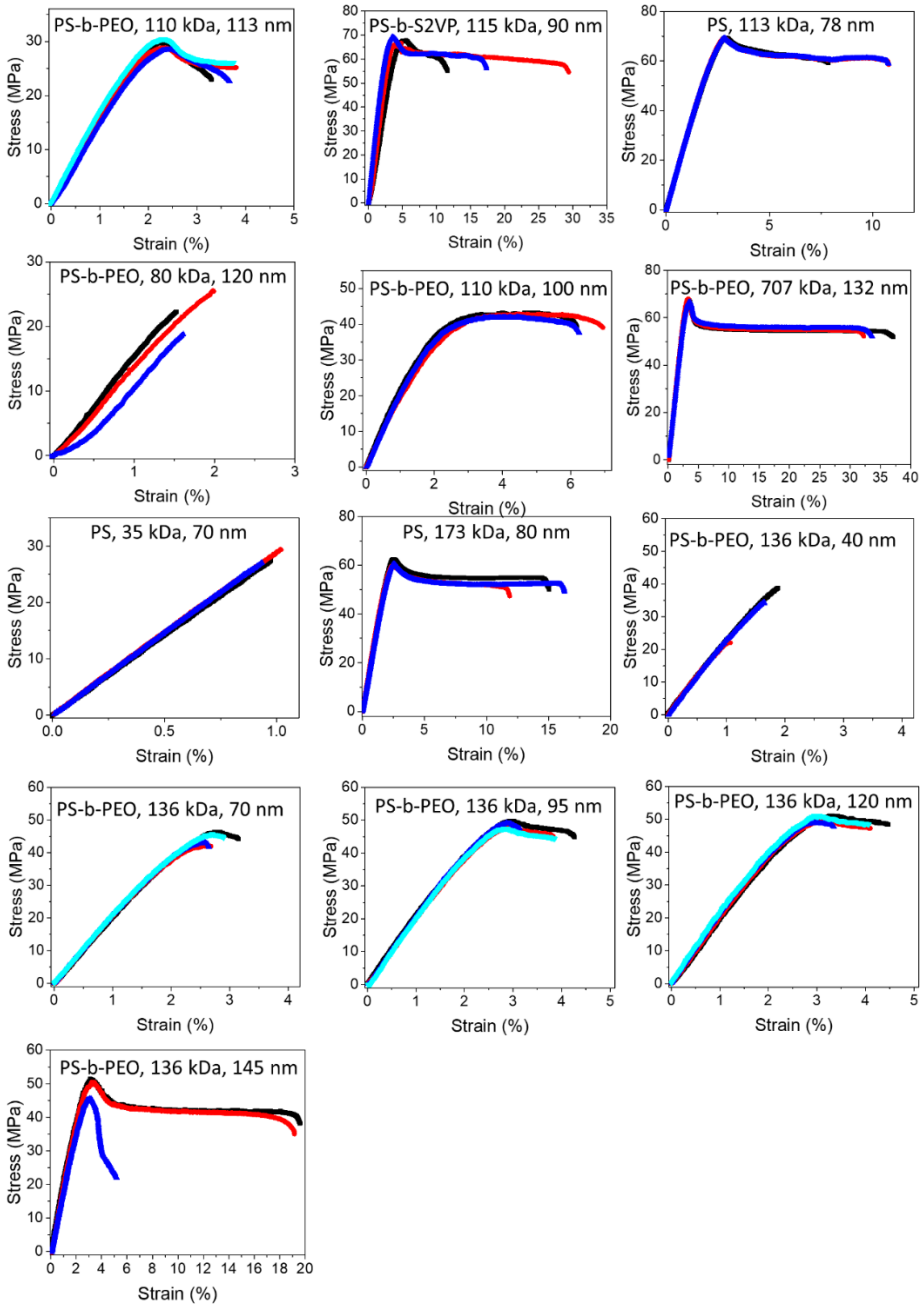

Figure A.1 *Mechanical film-on-water tensile data*

Stress-stain response for all polymers tested using film-on-water mechanical tester. Each polymer was tested at least three times. One representative stress-strain curve of each polymer was included in the main text for clarity as the data was highly repeatable.

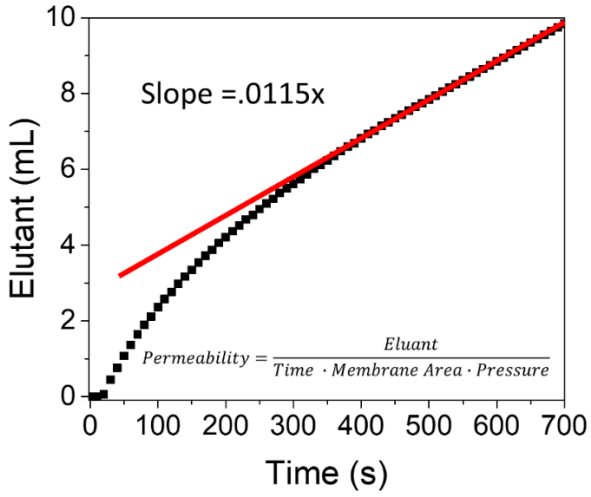

Figure A.2 *Permeability calculation example*

Representative example of how permeability was calculated. After an initialization period flux was linear with time. The slope at this portion of the graph was used to calculate permeability using the equation shown.

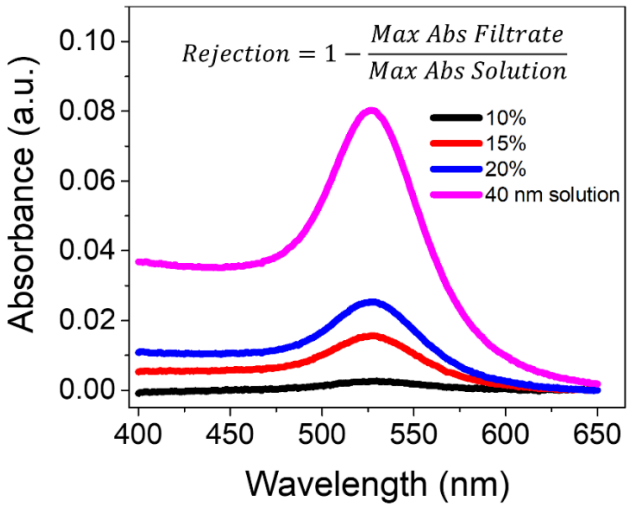

Figure A.3 *Selectivity calculation example*

Representative example of how AuNP rejection was calculated. UV-Vis absorbance was monitored near AuNPs absorption peak (530 nm) before and after filtration. The loss of intensity is directly related to loss of AuNP concentration and the rejection was calculated using the given equation.

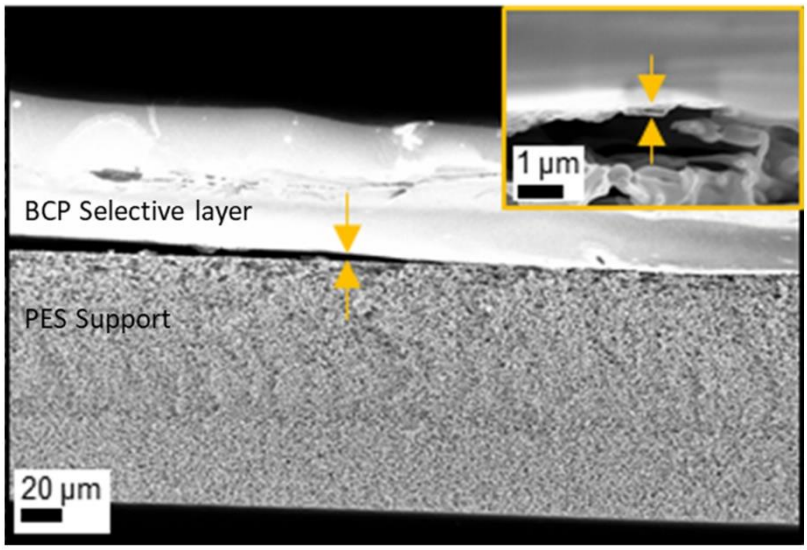

Figure A.4 *Membrane cross-section SEM*

Typical BCP composite membrane cross-section imaged by SEM. BCP layer is around 100 nm in thickness and has minimal infiltration into PES support.

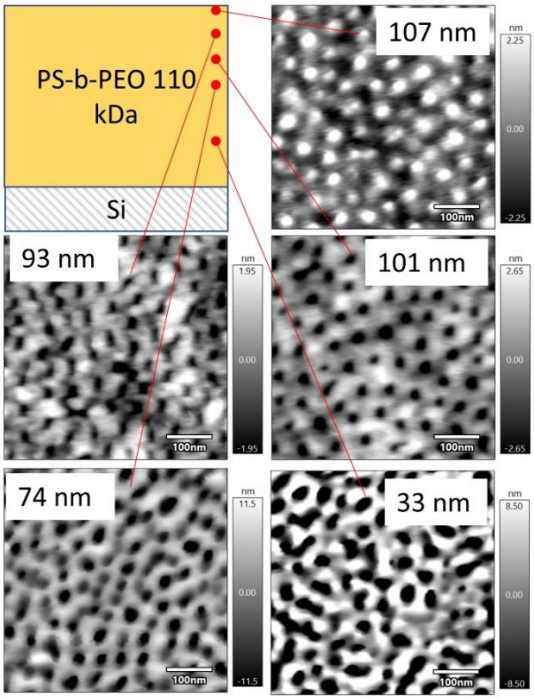

Figure A.5 *Morphology through thickness of selective layer*

PS-b-PEO 110 kDa morphologies after various plasma etching depths. All depths tested showed dot morphology consistent with perpendicularly aligned columns. At deeper depths (33 nm) morphology becomes partially mixed (dot and line).

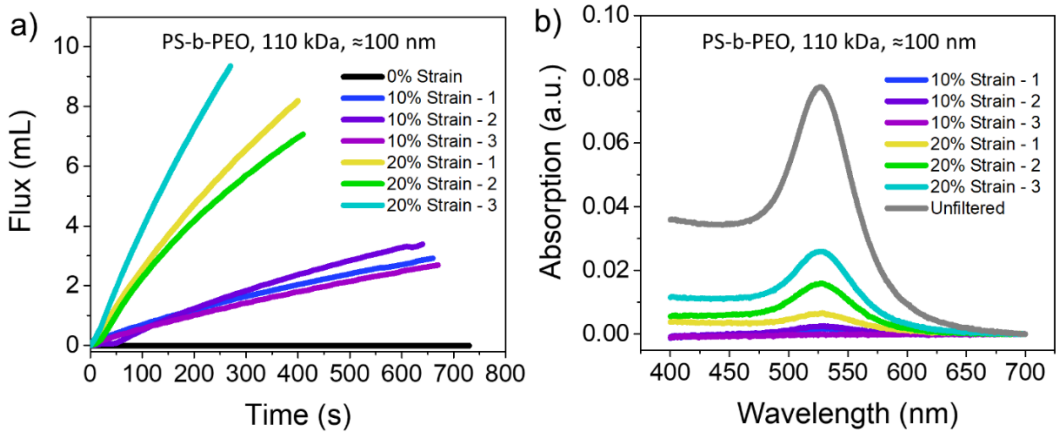

Figure A.6 *Raw filtration data PS-b-PEO 110 kDa*

Raw filtration data for stretched composite membrane based on PS-b-PEO 110 kDa. (a) clean water flux measurements. (b) UV-Vis absorbance spectra before and after filtration.

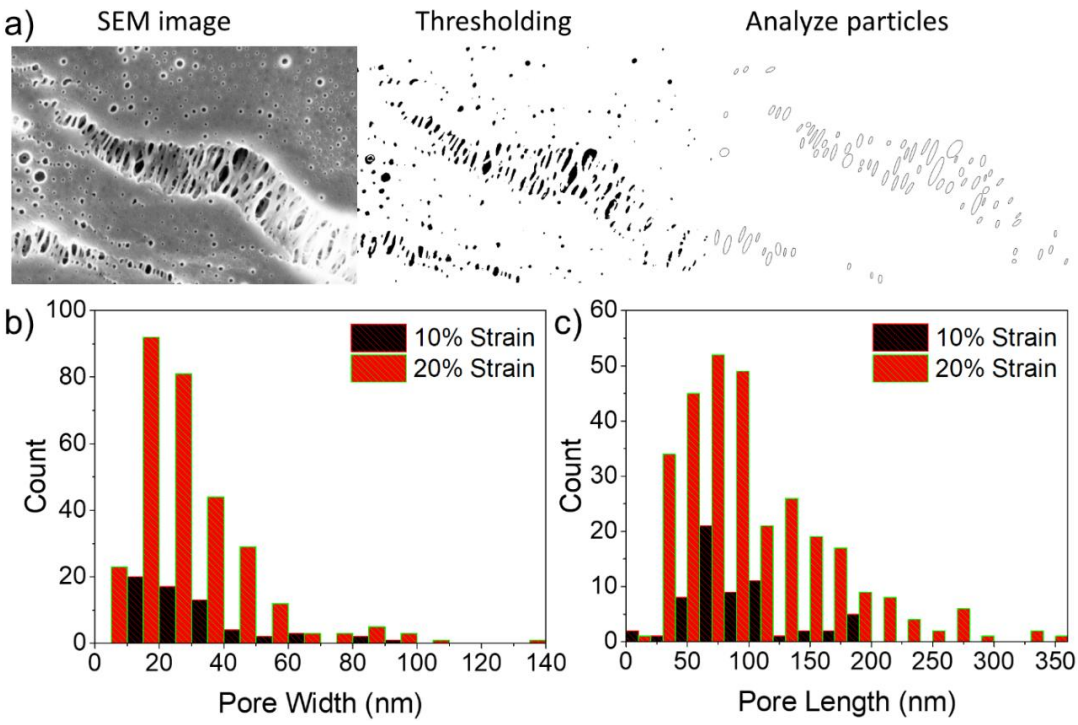

Figure A.7 *Pore size analysis PS-b-PEO 110 kDa*

Image J pore size analysis of PS-b-PEO 110 kDa (≈ 100 nm) stretched to 10 and 20% strain. (a) Example of Image J processing procedure. Thresholding is performed on the SEM image and then the particle analysis tool is used to fit ellipses to the dark areas. Only particles > 900 nm^2 with a circularity of < 0.7 were considered for analysis to eliminate non-porous features. (b)Histogram for minor diameters of the pore (pore widths) (c) Histogram for major diameters (pore lengths) of the analyzed particles.

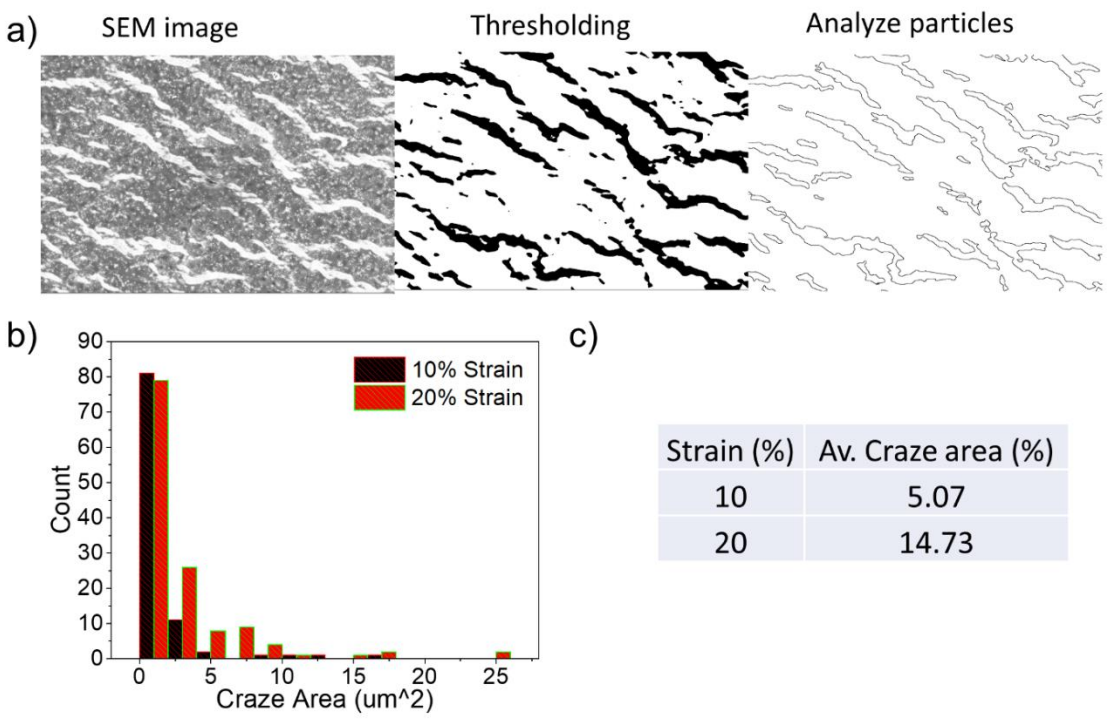

Figure A.8 *Craze size analysis PS-b-PEO 110 kDa*

Image J craze size analysis of PS-b-PEO 110 kDa (≈ 100 nm) stretched to 10 and 20% strain. (a) Example of Image J processing procedure. Thresholding is performed on the SEM image and then the particle analysis tool is used to calculate areas from the dark areas. (b) Craze area of the analyzed particles sorted into bins. (c) average craze area coverages.

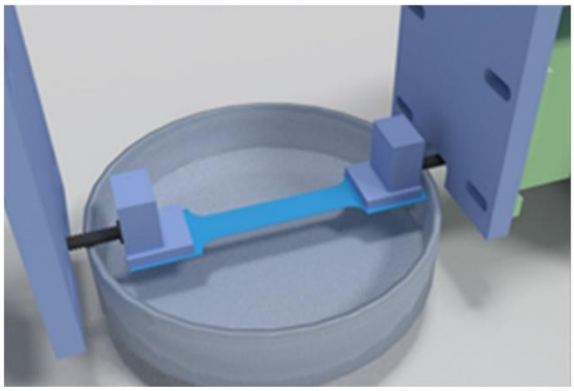

Figure A.9 *Film-on-water tensile tester*

Dogbone shaped thin-film specimens are floated onto a water bath and stretched by a linear stage after being attached by PDMS pads.

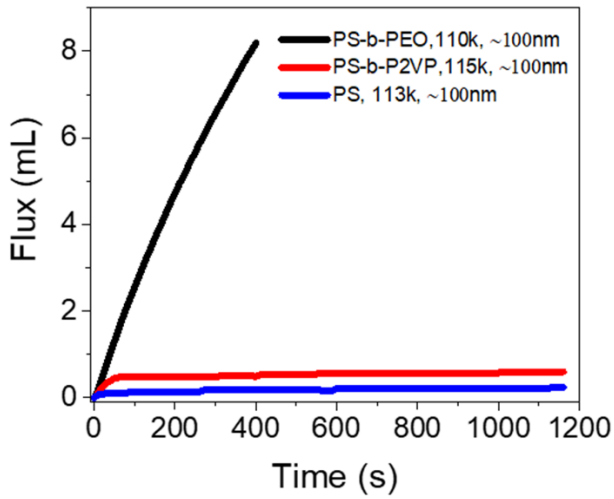

Figure A.10 *Water flux after 20% strain*

Clean water flux of 3 composite membranes containing different selective layers after 20% strain. Despite being stretched passed their unsupported fracture strain, their low flux indicate that when supported they remain intact up to 20% strain.

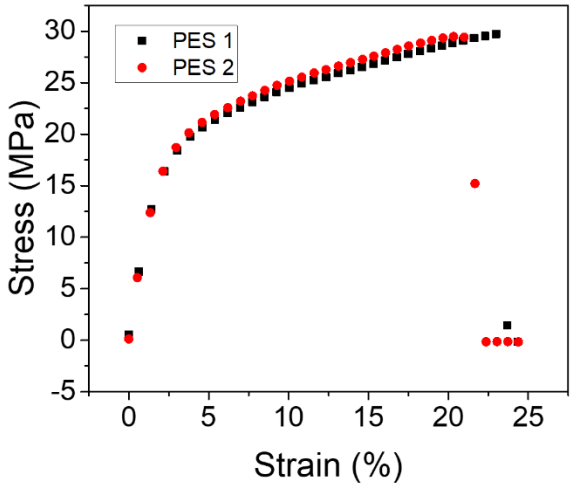

Figure A.11 *PES support mechanical properties*

Stress-strain data for bare PES support without any BCP top coatings. Rupture occurs between 20-25% strain.

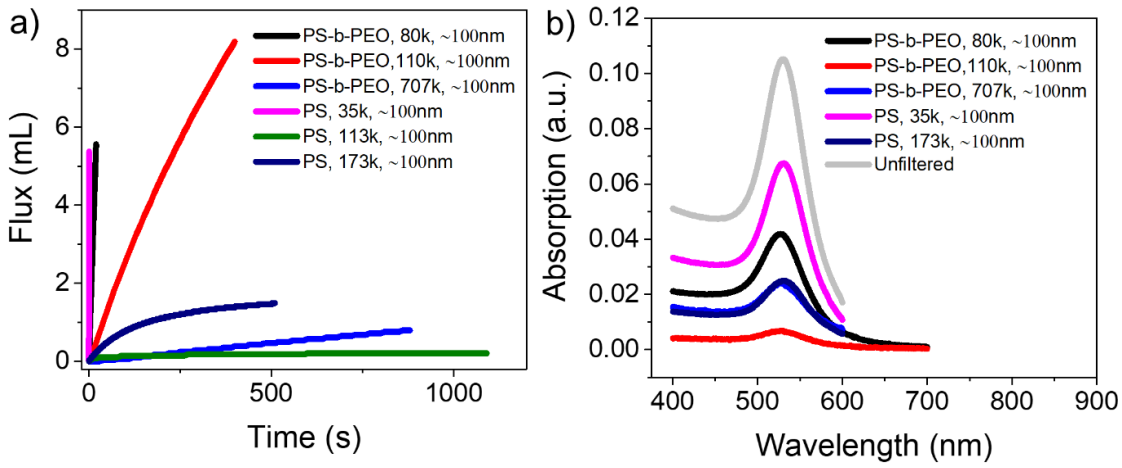

Figure A.12 *Raw filtration data for MW effect experiment*

Raw clean water flux (a) and UV-vis data (b) for determining the affect M_n has on filtration performance. Filtration of PS 113 kDa not possible due to insufficient flow.

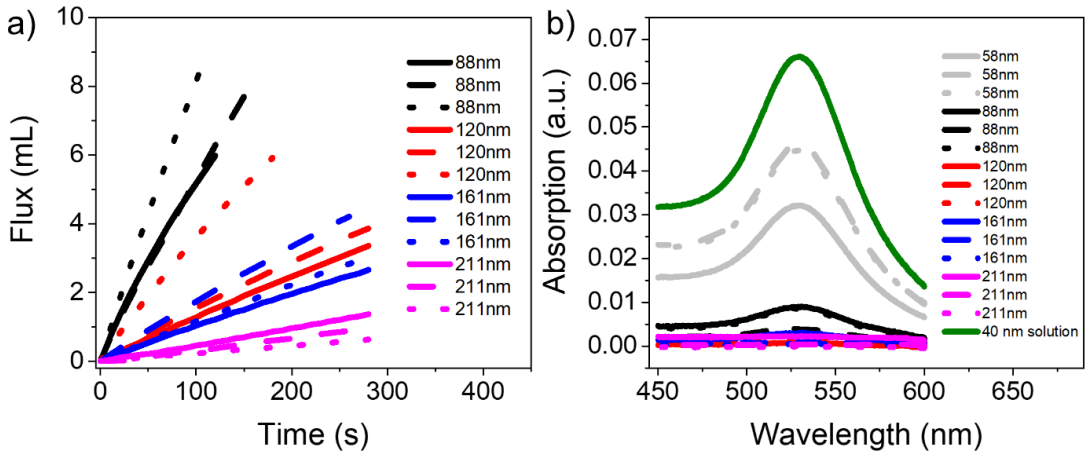

Figure A.13 *Raw filtration data for thickness effect experiment*

Raw clean water flux (a) and UV-vis data (b) for determining the affect thickness has on PS-b-PEO 136 kDa filtration performance. Flux of 58 nm film too high to measure with our set-up.

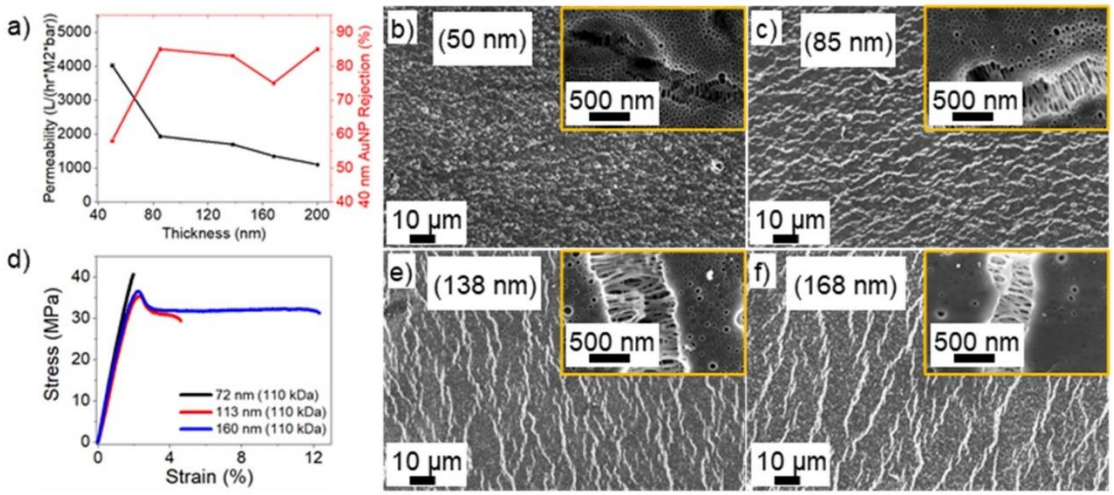

Figure A.14 *Thickness effect PS-b-PEO 110 kDa*

PS-b-PEO 110 kDa thickness effect on (a) permeability/selectivity (d) tensile properties (b,c,e,f) and craze formation.

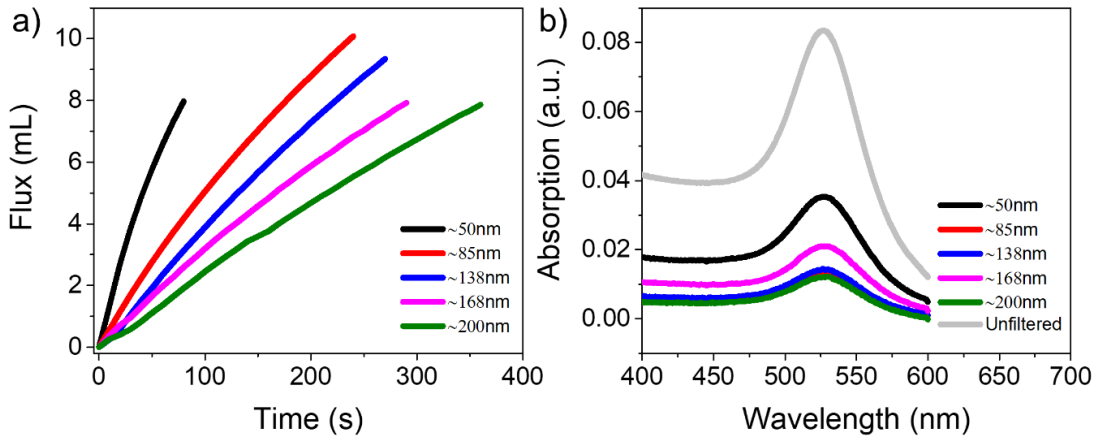

Figure A.15 *Raw filtration data for thickness effect experiment (PS-b-PEO 110 kDa)*

Raw clean water flux (a) and UV-vis data (b) for determining the affect thickness has on filtration performance for PS-b-PEO 110 kDa selective layers (Figure A.14).

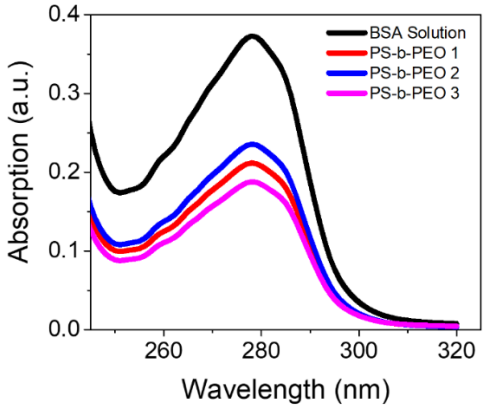

Figure A.16 *Raw filtration data for BSA rejection experiment*

Raw data for the filtration of BSA with PS-b-PEO 136 kDa membranes stretched to 20% strain

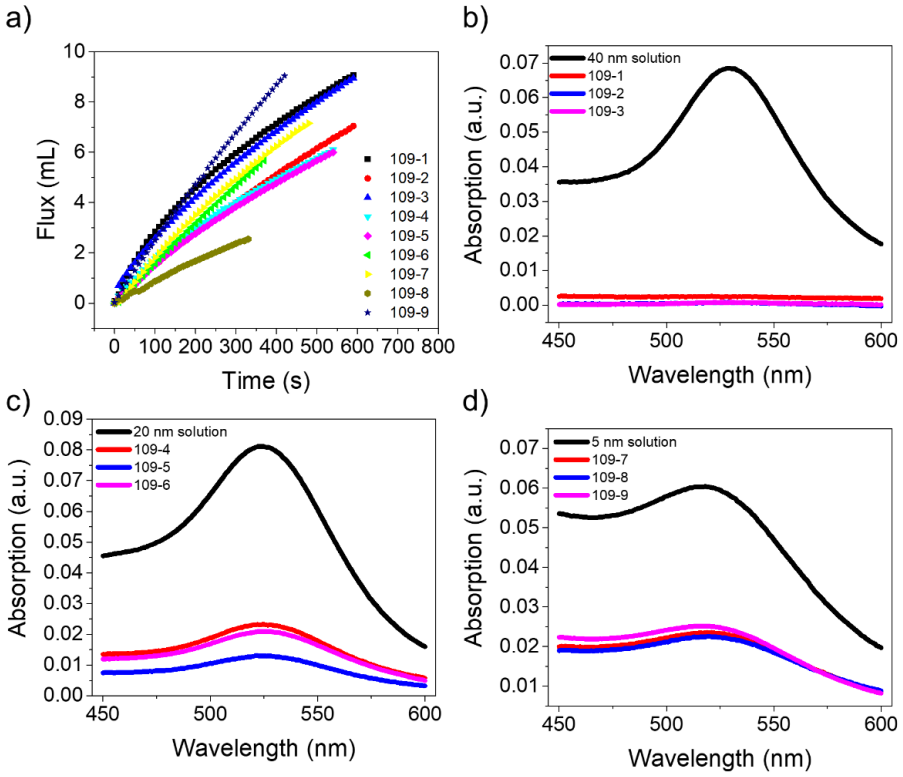

Figure A.17 *Raw filtration data for size selectivity experiment*

Raw data for AuNP size selectivity experiment of 125 nm PS-b-PEO 136 kDa stretched 20%. (a) clean water permeability of the 9 samples used in the study (b) Uv-vis data for calculating 40 nm rejection (c) Uv-vis data for calculating 20 nm rejection (d) Uv-vis data for calculating 5 nm rejection.

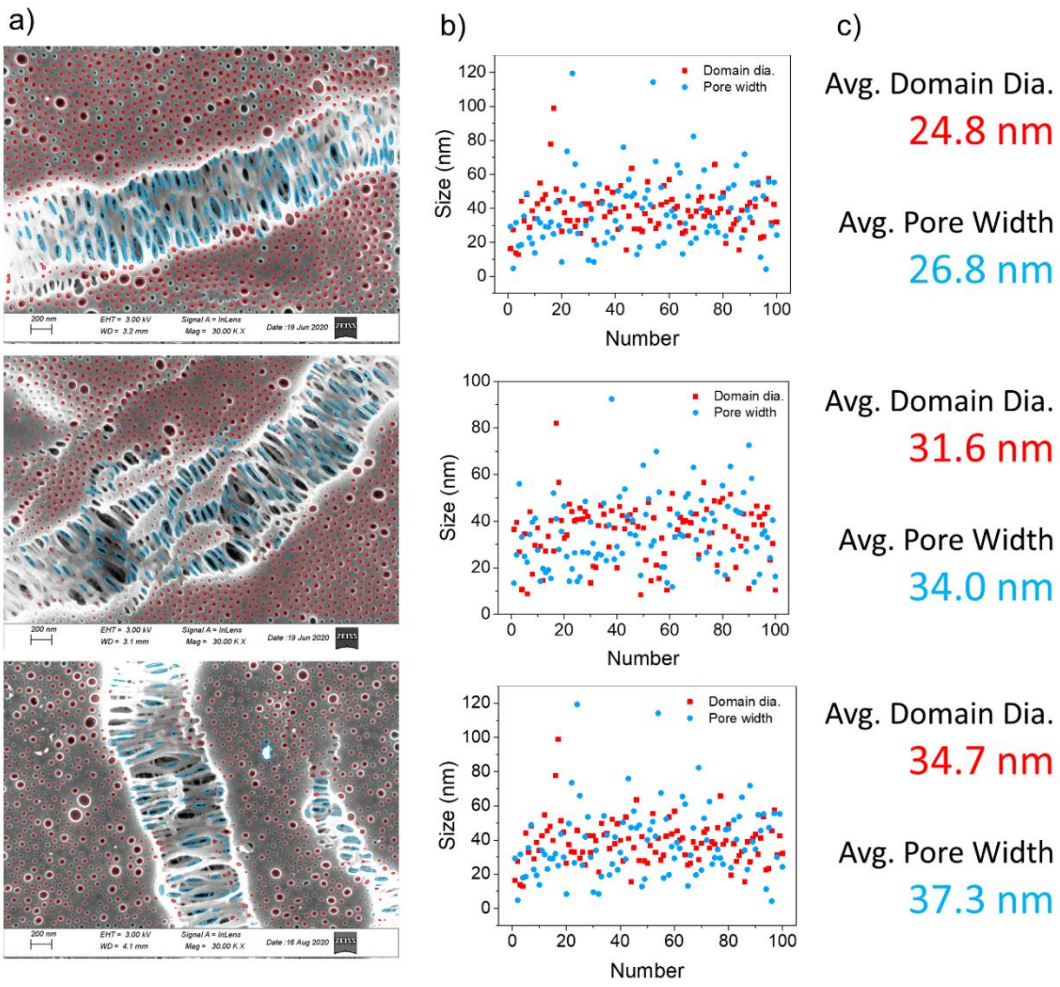

Figure A.18 *Domain size to pore width comparison*

SEM images were analyzed with Image J software on 3 different membranes showing a correlation between domain size and pore width. (a) Particle analysis was used to fit ellipses to all the dark regions. Ellipses were then sorted into “pores” or “domain” based on circularity, pores being much more elliptical. (b) The minor diameter of the fit ellipses plotted in scatter plots. (c) Averages of the domain sizes and pore widths.

APPENDIX B Supporting information for Chapter 3

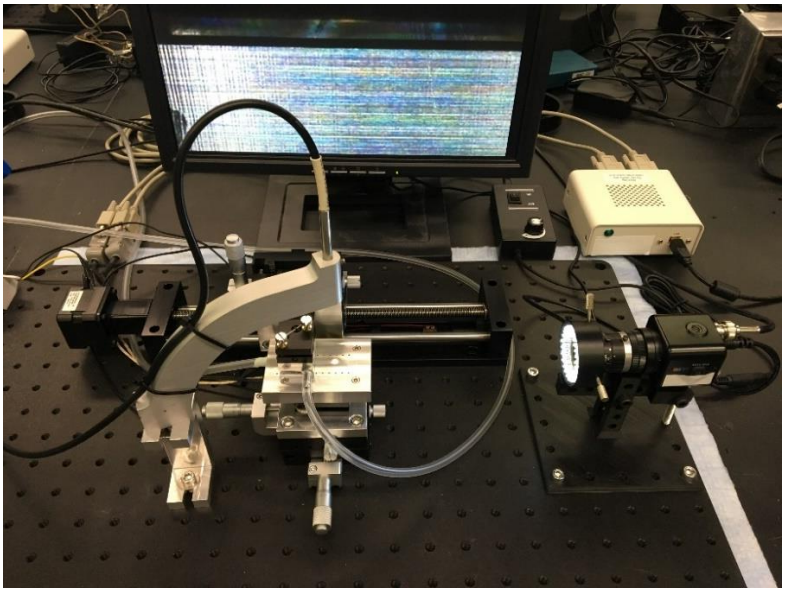

Figure B.1 *In situ thickness measurement shear coater set-up*

Photography of the in situ thickness measurement set up. An interferometer mounted above an adjustable shear coater measures the film thickness of a drying film every few seconds.

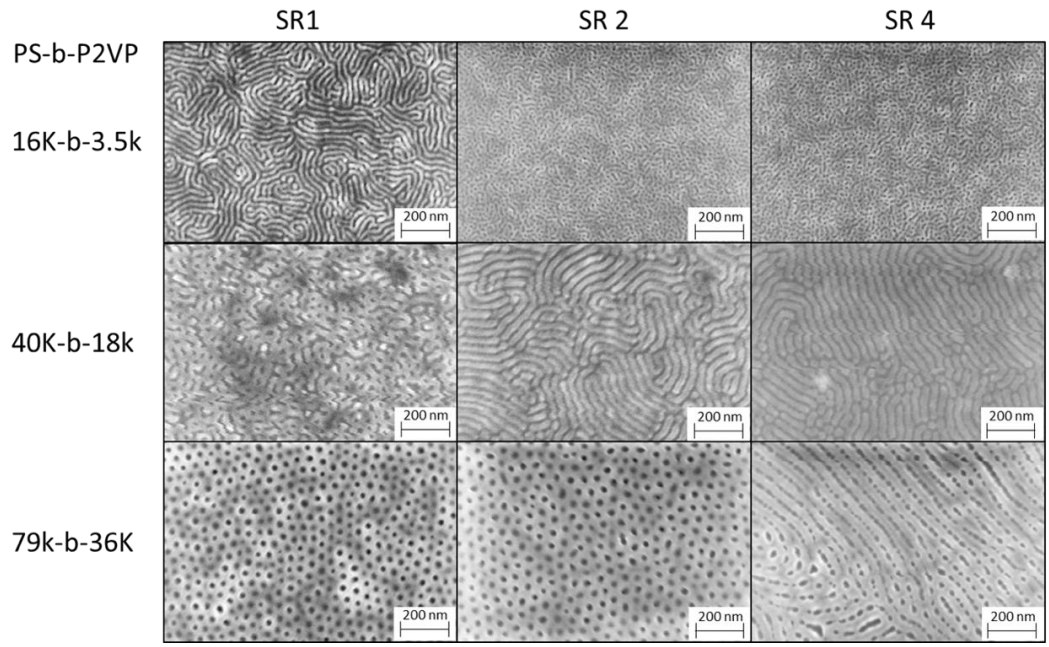

Figure B.2 *SR effect on PS-b-P2VP of varying molecular weight*

Representative PS-b-P2VP morphologies of various molecular weights annealed with CN additive. Without any annealing (SR1) it is interesting to note that low molecular weight polymers form fingerprint pattern while high molecular weight form dot patterns and medium sized chains are a line dot pattern. In all cases NVASA annealing moves the morphology towards the fingerprint pattern with lower swell ratios needed for smaller chains. Very short chains undergo an order disorder transition between SR1 and SR2 due to its low tendency to phase separate.

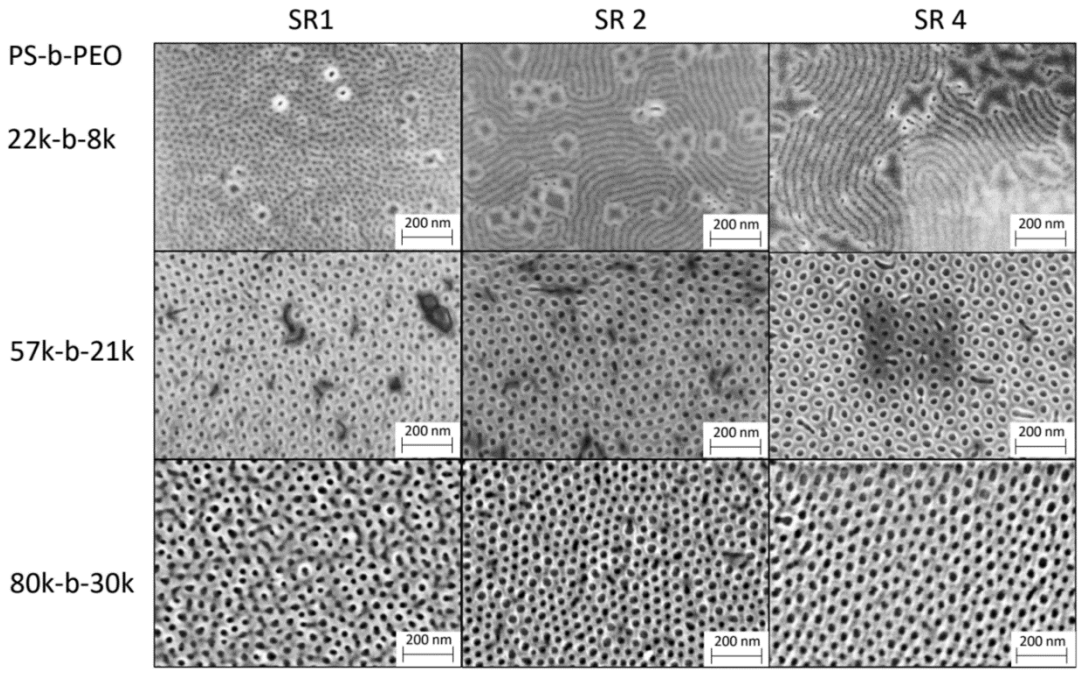

Figure B.3 *SR effect on PS-b-PEO of varying molecular weight*

Representative PS-b-PEO morphologies of various molecular weights annealed with CN additive. Without any annealing (SR1) all polymers form dot patterns. The lowest molecular weight chain switches to a fingerprint morphology at low swell ratios while larger molecular weight chains don't change morphology but rather improve their hexagonal order.

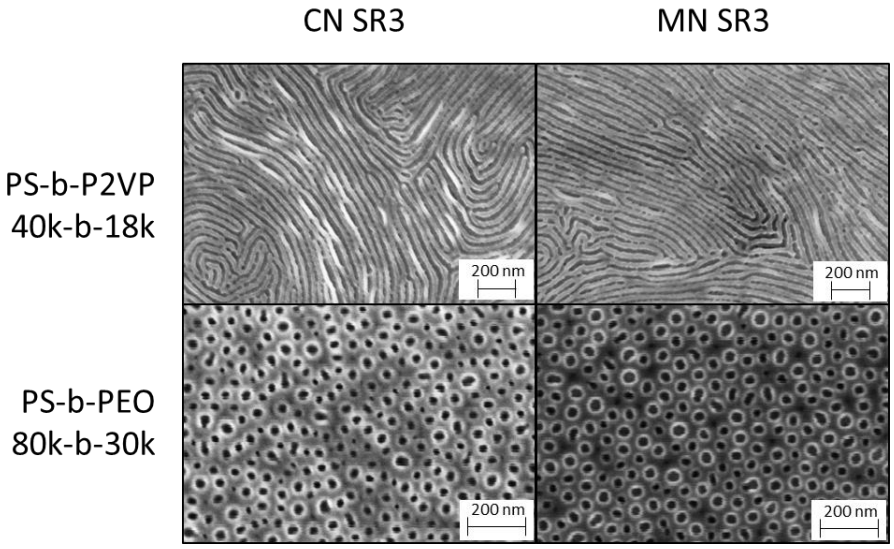

Figure B.4 *High boiling point additive comparison*

Comparison of Polymers swollen with 1-chloronaphthalene (CN) vs 1-methylnaphthalene (MN) Demonstration that 1-chloronaphthalene (CN) can be replaced with other high boiling point additives, in this case 1-methylnaphthalene (MN) and attain similar results regardless of the native morphology.

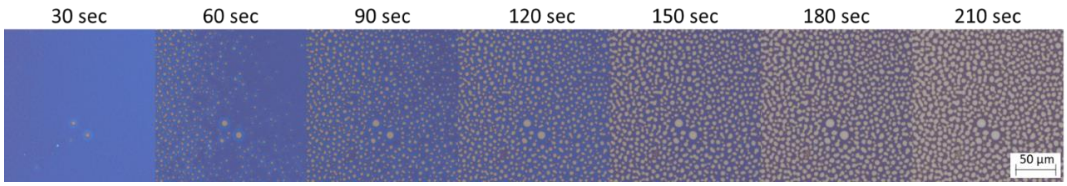

Figure B.5 *Island hole formation during drying*

Optical microscope monitoring of island and hole formation of PS-b-PEO, 80k-b-30k, 10 mg/mL in toluene with CN additive (SR3) solution after 5 sec spin coat. Formation of island and holes indicates high chain mobility which is not seen without use of a high boiling point additive to slow the drying process.

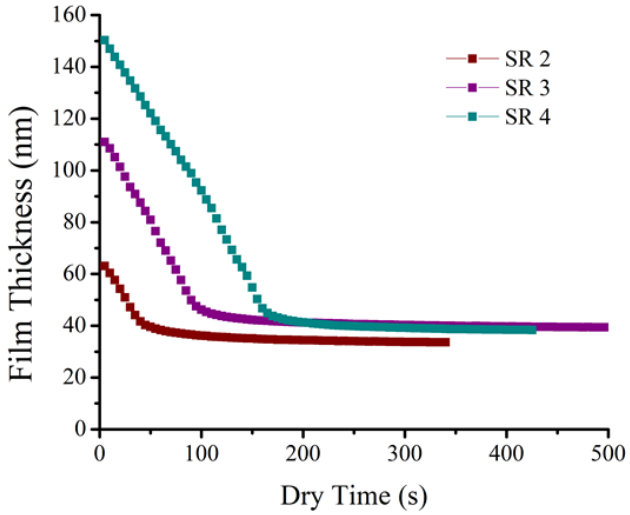

Figure B.6 *Swell ratio effect on drying profile*

PS-b-PEO, 80k-b-30k, 10 mg/mL (T_i ~ 38 nm) solutions were made with various amounts of CN additive to swell the polymer to different swell ratios. The graph above monitors film thickness while it dries after a 5 sec spin coat. Thickness loss is linear and independent of initial thickness.

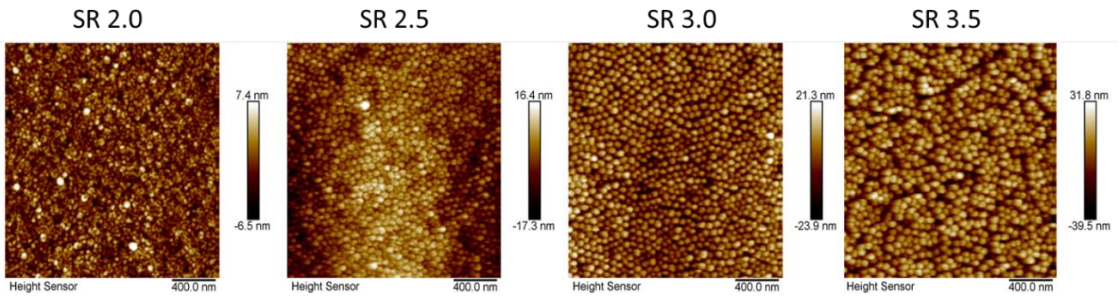

Figure B.7 *Effect of swell ratio in plasticizer swollen films*

SR effect of plasticizer (dibutyl phthalate) when added to PS-b-PEO, 80k-b-30k, for 45 min. before removal in ethanol. At low swell ratios no morphology seen but column formation appears at higher swell ratios reaching a maximum order at a swell ratio of 3. Beyond SR 3 the morphological order begins to degrade.

Table B.1 *Solubility parameters of additives and polymers*

Hansen Solubility Parameters

	δD	δP	δH
	Polymers		
PS	21.3	5.8	4.3
P2VP*	16.3	6.5	8.0
PEO*	17.0	10.7	8.9
	Additives		
CN	19.9	4.9	2.5
MN	20.0	0.8	4.7
DBPth	17.8	8.6	4.1

Distance Apart in Solubility Space

	Ra(CN)	Ra(MN)	Ra(DBPth)
PS	3.4	5.6	7.5
P2VP	9.2	9.9	5.3
PEO	10.4	12.3	5.5

*Solubility parameters found from alternative sources. P2VP from [169] and PEO from [170]

all solubility parameters taken from Hansen Solubility Parameters A User's Handbook and the calculated distance between solvents and polymers in solubiliy space (Ra). The lower Ra value the higher the solubility between the components. CN and MN are both selective towards PS, the major block, while DBPth is a good solvent for both major and minor blocks with a slight prefference for the minor block.

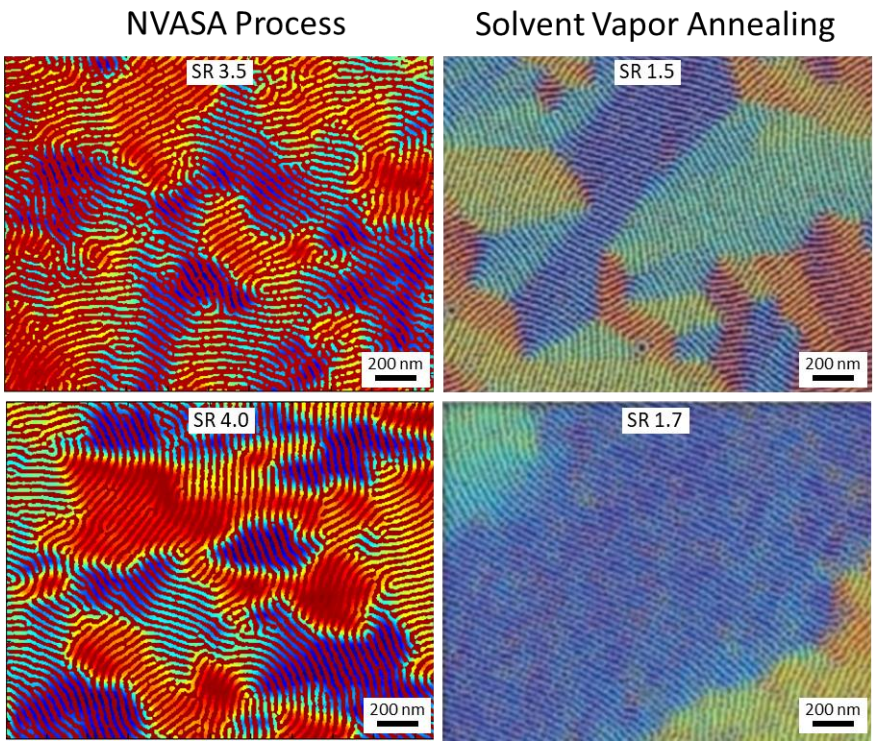

Figure B.8 *Grain size analysis of NVASA process*

Grain size visualization comparison of NVASA process with traditional solvent vapor annealing using an image filter which colors the image based on the angle of domains. NVASA process was performed with PS-b-P2VP (Mn = 40-b-18 kg/mol) BCP using CN additive shows a grain size up to ~300 nm. Solvent vapor annealing was performed with PS-b-P2VP (Mn = 23.6-b-10.4 kg/mol) and annealed with THF vapor achieving grain sizes up to about 2µm. Solvent vapor annealing images were adapted with permission from Ref. [101].

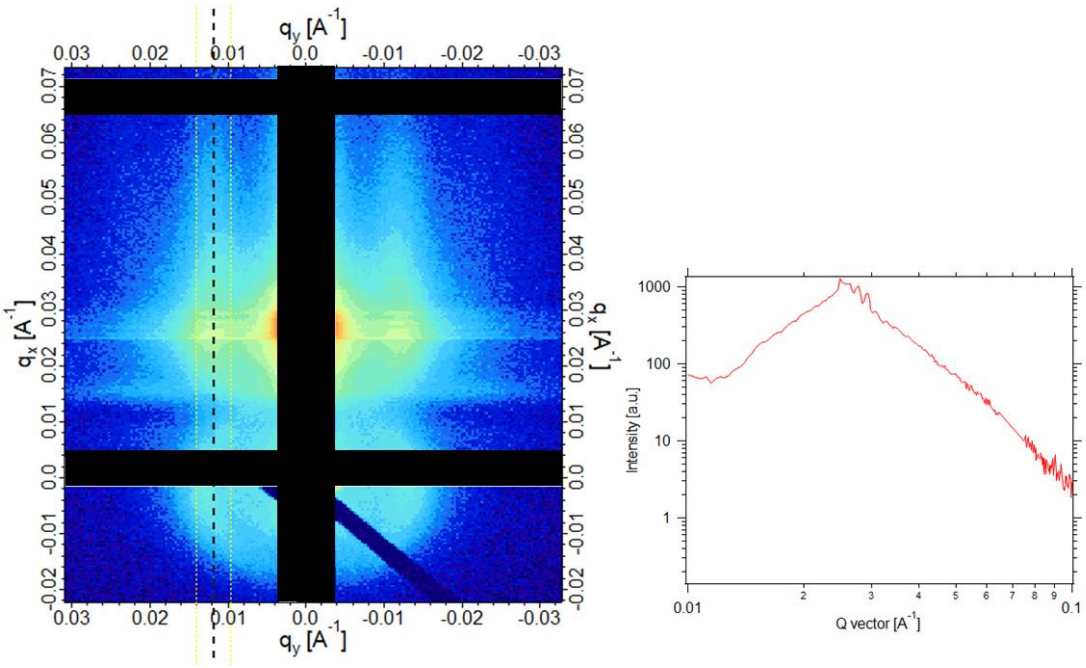

Figure B.9 *Morphology of PS-b-PEO by GISAXS*

GISAXS scattering data of PS-b-PEO (80-b-30 kg/mol) spun coat on a Si wafer and reconstructed in 2-Propanol at 50 C° for 20 min. Thickness before reconstruction was 122 nm and thickness after reconstruction was 139 nm. 2-Propanol swells the PEO domains deforming the PS matrix, when it evaporates a cavity of air is created giving a high scattering contrast. (left) 2-D scattering pattern showing multiple peaks in the vertical direction. The yellow dotted lines show the area that was integrated for 1-D analysis. (right) 1-D section cut scattering data. At least 3 peaks observed between .02 < q < .03. The appearance of peaks in the vertical direction indicates there is periodic spacing through the thickness of our film. This indicates that the dot pattern seen at the surface is not due to perpendicular columns but rather a stacked spherical morphology.

APPENDIX C Supporting information for Chapter 4

Table C.1 *Recipe for PPR vulcanization.*

Ingredient	**phr[a]**
PPR	100
Zinc stearate[b]	0.5
DPG[c]	0.2
CBS[d]	0.2
Sulfur[e]	0.5

[a]phr: parts per hundred rubber, [b]Technical grade (Sigma-Aldrich), [c]DPG: diphenyl guanidine (98%, TCI), [d]CBS: N-cyclohexyl-2-benzothiazole sulfonamide (>98%, TCI), [e]Superfine sulfur (99.5%, Akrochem)

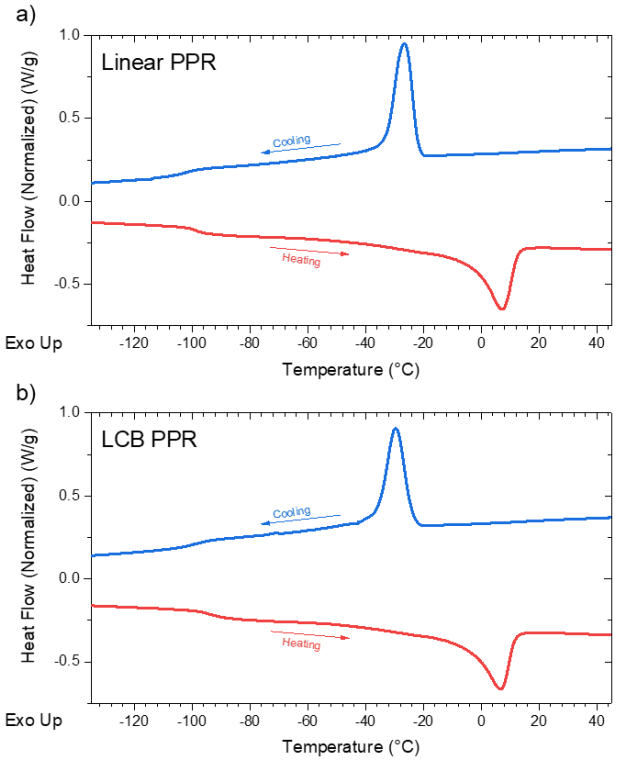

Figure C.1 *DSC Scans of a) Linear PPR and b) Branched PPR.*

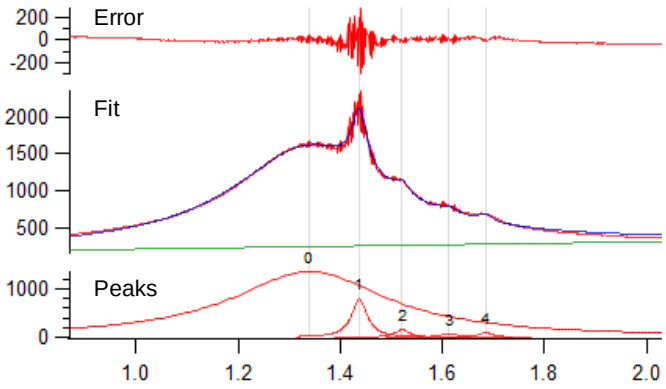

Figure C.2 *Igor curve fitting example*

1 amorphous (labeled as peak 0) and 4 crystalline peaks (labeled as peak 1~4) were used to fit data. The red line is the data, blue line is the model. The integrated peak areas were then used to calculate crystalline content by the equation below.

$$\%\ Crystallinity = 100 \times \frac{\sum Peak\ areas\ 1,2,3,4}{\sum Peak\ area\ 0,1,2,3,4}$$

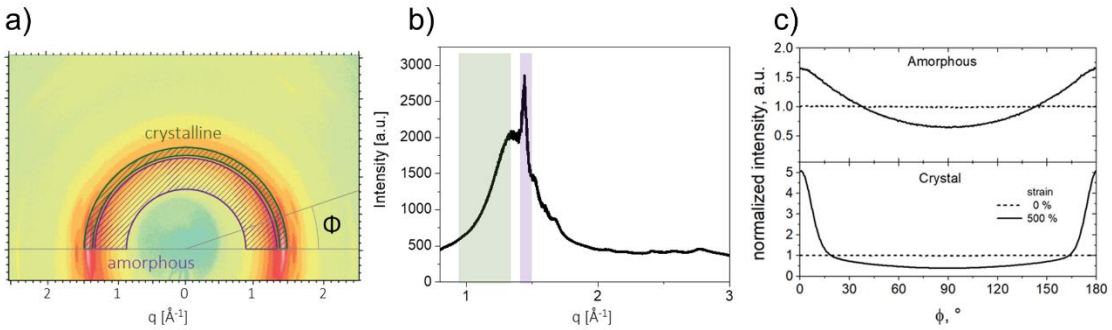

Figure C.3 *Alignment factor calculation*

Method for extracting alignment information from WAXS data. a) Amorphous and crystalline q regions on 2D scattering plot which were plotted vs. azimuthal angle. b) Amorphous and crystalline q regions used for azimuthal angle plot shown on 1D plot. c) Azimuthal angle vs. intensity plot for amorphous and crystalline q ranges showing alignment in stretch direction.

Figure C.3 shows the q range and methods used for the alignment calculations. Notice that half of the amorphous halo was not considered to avoid complication from crystalline

peak overlap. When intensity in these q ranges are plotted versus azimuthal angle (Φ) a plot like Figure 4.7c is obtained which gives an indication of the alignment present in the plot. Higher intensity near 0° and 180° comes from chains aligned with stretch. The intensity around 90° represents chains aligned perpendicular to stretch.

Branching Index Calculation from GPC Data

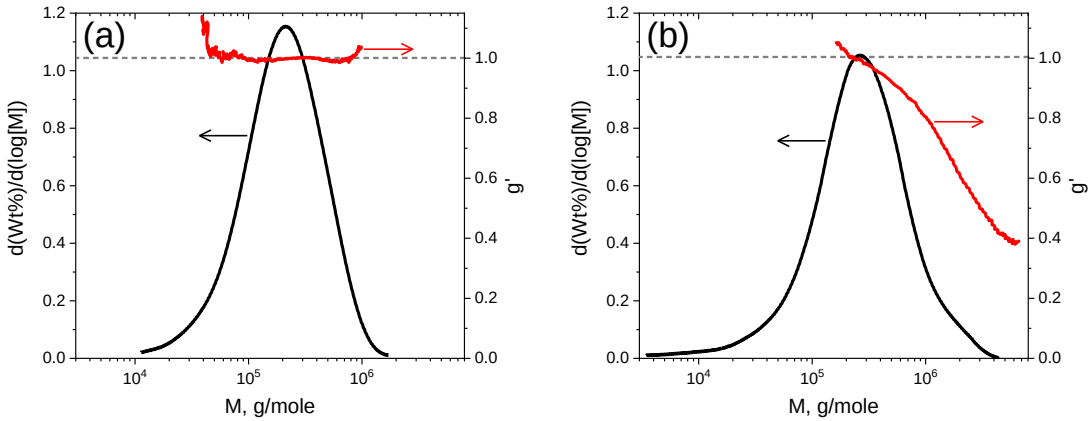

Figure C.4 *Branching index calculation from GPC data*

Molecular weight density and branching index (g') versus molecular weight (M) for linear and branched CP polymers. a) Linear CPR branching index is M-independent around 1. b) Branched CPR has an average branching index at 0.81 and decreases with increasing M, demonstrating branching is occurring.

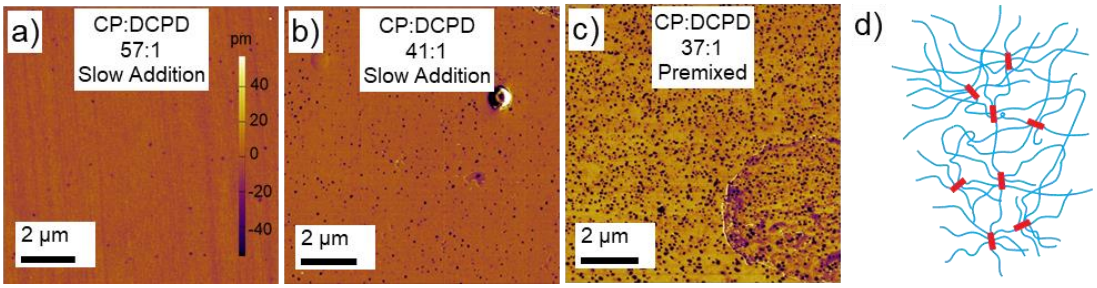

Figure C.5 *Hard domain size analysis by AFM*

AFM height images showing increased surface pitting with higher levels of DCPD. a) CP to DCPD monomer ratio of 57:1 contains minimal amounts of depressions. Scale bar applicable to all micrographs. b) Higher CP to DCPD monomer ratio of 41:1 ratio shows

increased size and abundance of depressions. c) CP to DCPD ratio of 37:1 where all DCPD was premixed with CP at start of reaction rather than slowly added. d) Proposed topology of the long chain branched CP:DCPD copolymerization. Hard DCPD domains (red) provide the majority of branching sites, all of which are interconnected through linear CP chains.

Atomic force microscopy (AFM) performed on cured PPR revealed nano-segregation occurring in the branched samples (Figure 4.5). The size and number of these nanodomains were influenced by both the amount of DCPD added, and the rate at which DCPD was added. The characterization of the PPRs for each DCPD level can be found in the next section. Because the nanodomain prevalence increases with increasing DCPD loading level, combined with the fact that DCPD's T_g is much higher than CP (163 °C), we believe the dark dots in the micrographs are glassy DCPD-rich hard domains embedded in the CP-rich soft matrix. We attribute the nanostructure observed in the LCB PPRs to the much larger ROMP reactivity of DCPD compared to that of CP. This results in the formation of blocky DCPD-rich chain segments being formed as soon as DCPD is delivered to the reactive solution. When this is done slowly during the course of the reaction, the local DCPD concentration can diffuse relatively fast and, thus, a more uniformly branched architecture is produced. However, formation of some concentrated DCPD domains cannot be avoided, and a few hard-glassy domains are formed (Figures C.5a and C.5b). If all the DCPD is added initially, this monomer will have less chance to diffuse and react homogeneously with CP, and more glassy domains will be formed, as seen in Figure C.5c.

We postulate that these domains act as branching hubs from where multiple branches originate, as illustrated in Figure C.5d. The hyperbranched topology is formed when DCPD monomers propagated for existing branches and form a satellite branching hub. Interestingly, no crosslinking events occur during the reaction, and these polymers can be

melt processed before vulcanization. Moreover, the hard DCPD domains may act as very well dispersed nanofillers with very effective reinforcement effect, which is likely contributing to branched PPR's increased tensile properties, obfuscating the effect branching would have on its own.

Table C.2 *Material properties for PPRs used in AFM study*

	57:1 Slow Addition	41:1 Slow Addition	37:1 Premixed
cis/trans mole ratio	19/81	20/80	23/77
cC5/DCPD	57/1	41/1	37/1
Mw, kg/mol	475	614	611
Mw/Mn	1.98	1.70	1.75
Tg, °C	-93.4	na	na
Tm (peak), °C	6.62	na	na
Tc (onset), °C	-23.7	na	na

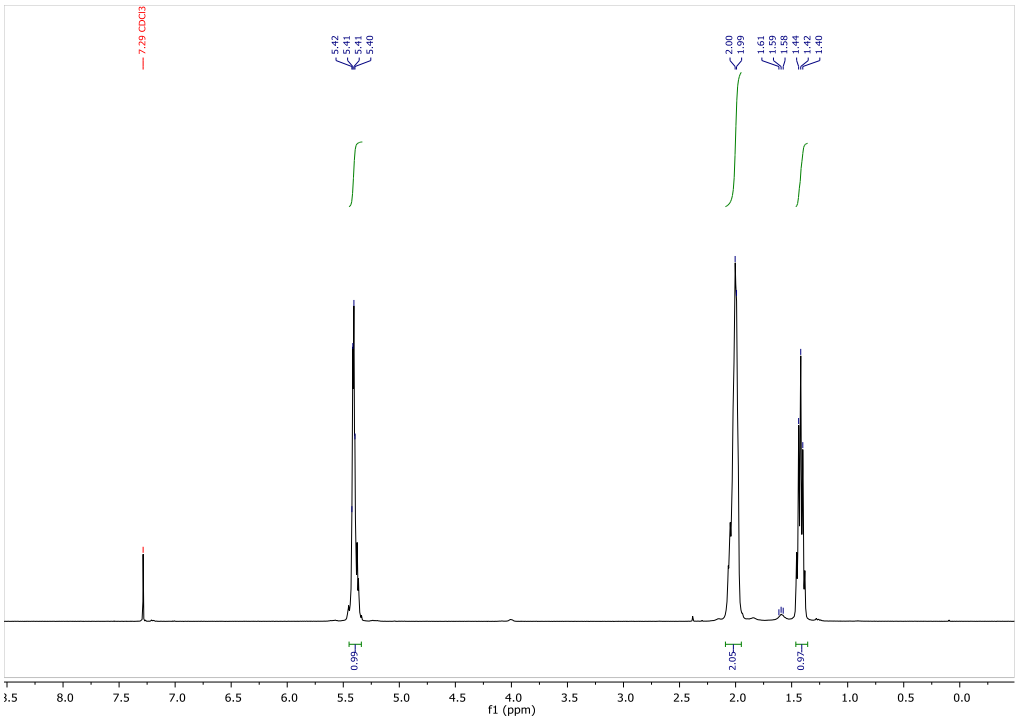

Figure C.6 *^{1}H NMR spectrum for linear PPR (in $CDCl_3$)*

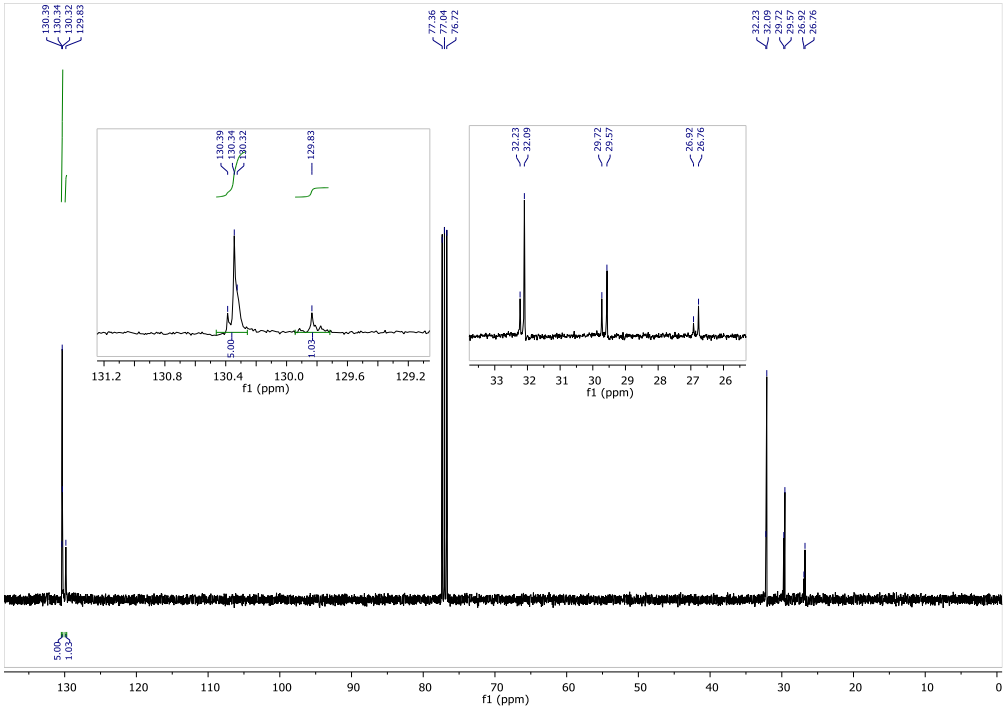

Figure C.7 *^{13}C NMR spectrum for linear PPR (in $CDCl_3$)*

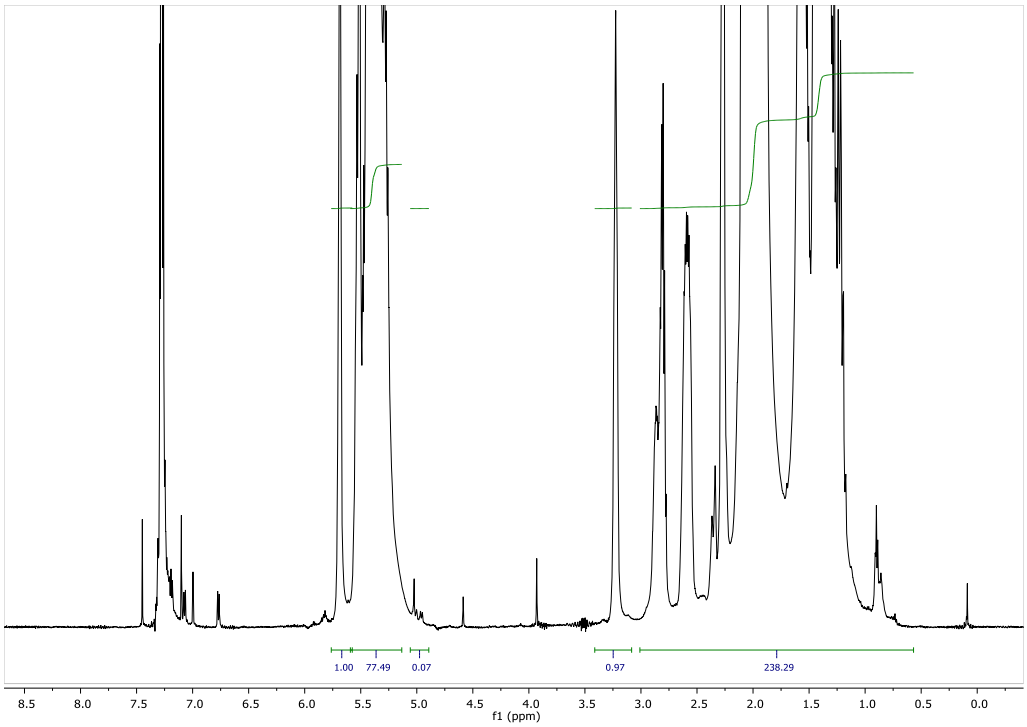

Figure C.8 *[1]H NMR spectrum for LCB PPR (in $CDCl_3$)*

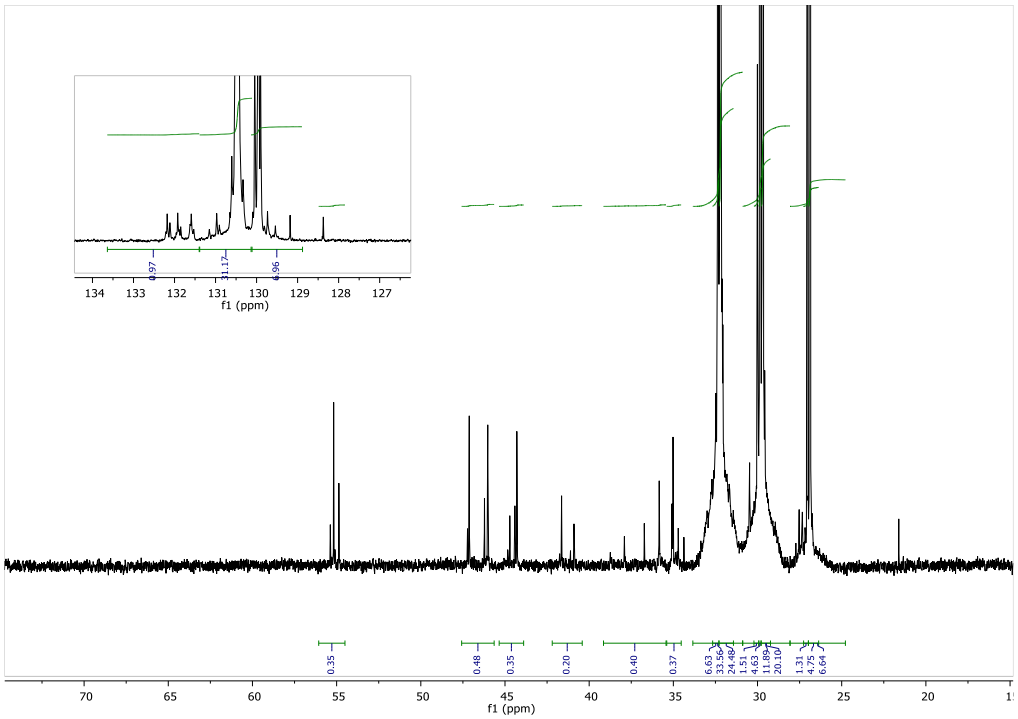

Figure C.9 *[13]C NMR spectrum for LCB PPR (in $CDCl_3$)*

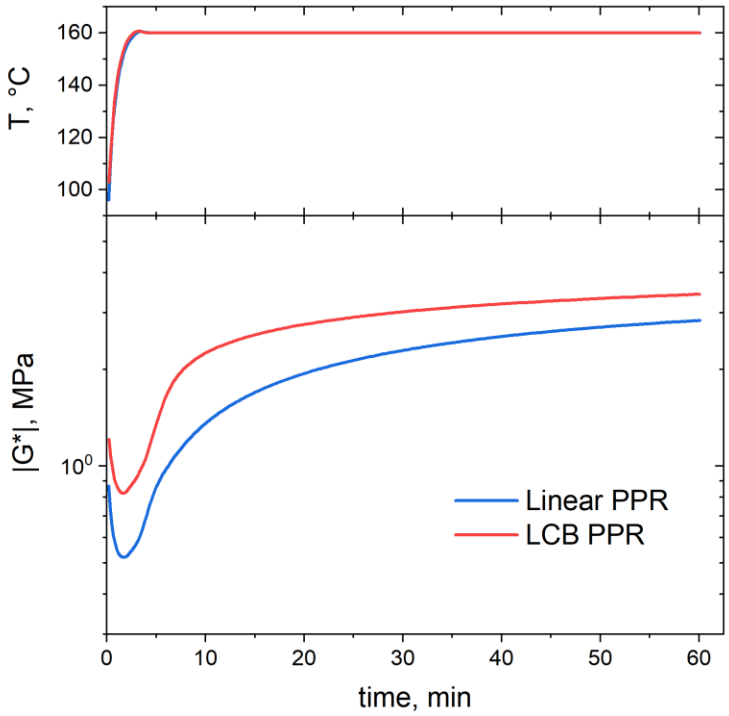

Figure C.10 *Cure kinetics of linear and LCB PPR*

Cure kinetic curves for linear and LCB PPRs measured in the rheometer ARES-G2 using a frequency of 1 Hz and strain amplitude of 0.1 %. Samples are loaded at 80 °C in 8 mm serrated parallel plates geometry, after which the temperature is increased to 160 °C.

APPENDIX D Supporting information for Chapter 5

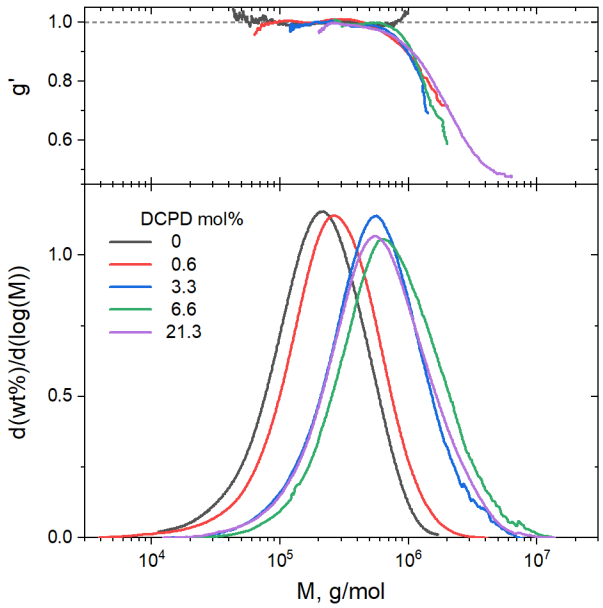

Figure D.1 *GPC data for the calculation of branching index*

(top) and molecular weight density (bottom) versus molecular weight (M) for polymers of varying DCPD content.

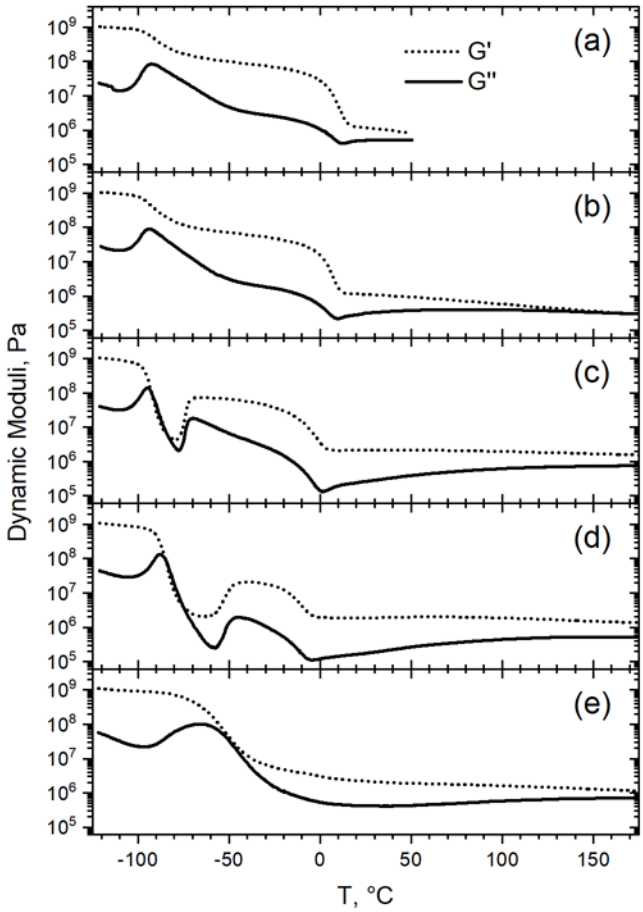

Figure D.2 *Storage and loss modulus curves of the DMTA*

DMTA scans ran at a heating ramp of 2 °C/min after fast quenching (60 °C/min)

0% DCPD (-40 C)
28.4% crystallinity

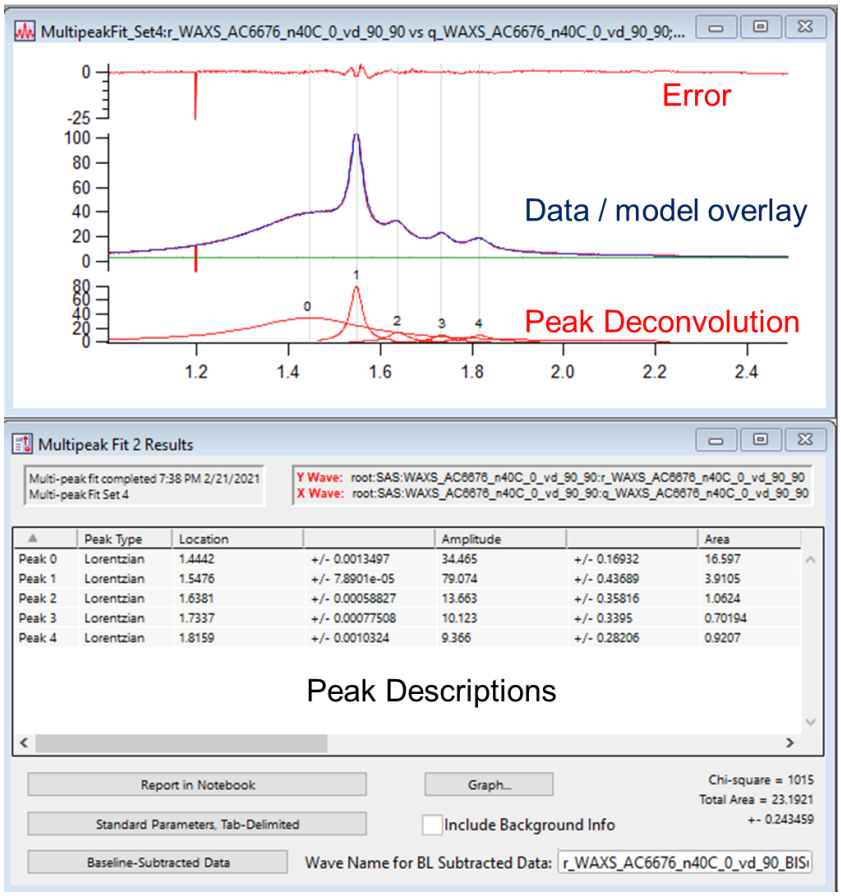

Figure D.3 *Crystallinity calculation example*

Example of Igor curve fitting software. (Top) Peak fitting results. Raw data neatly described as the combination of 1 amorphous peak (peak 0) and 4 crystalline peaks (peaks 1-4). (bottom) Peak descriptions used to calculate % crystallinity using following equation.

$$\%\, Crystallinity = 100 \times \frac{\sum Peak\ areas\ 1,2,3,4}{\sum Peak\ area\ 0,1,2,3,4}$$

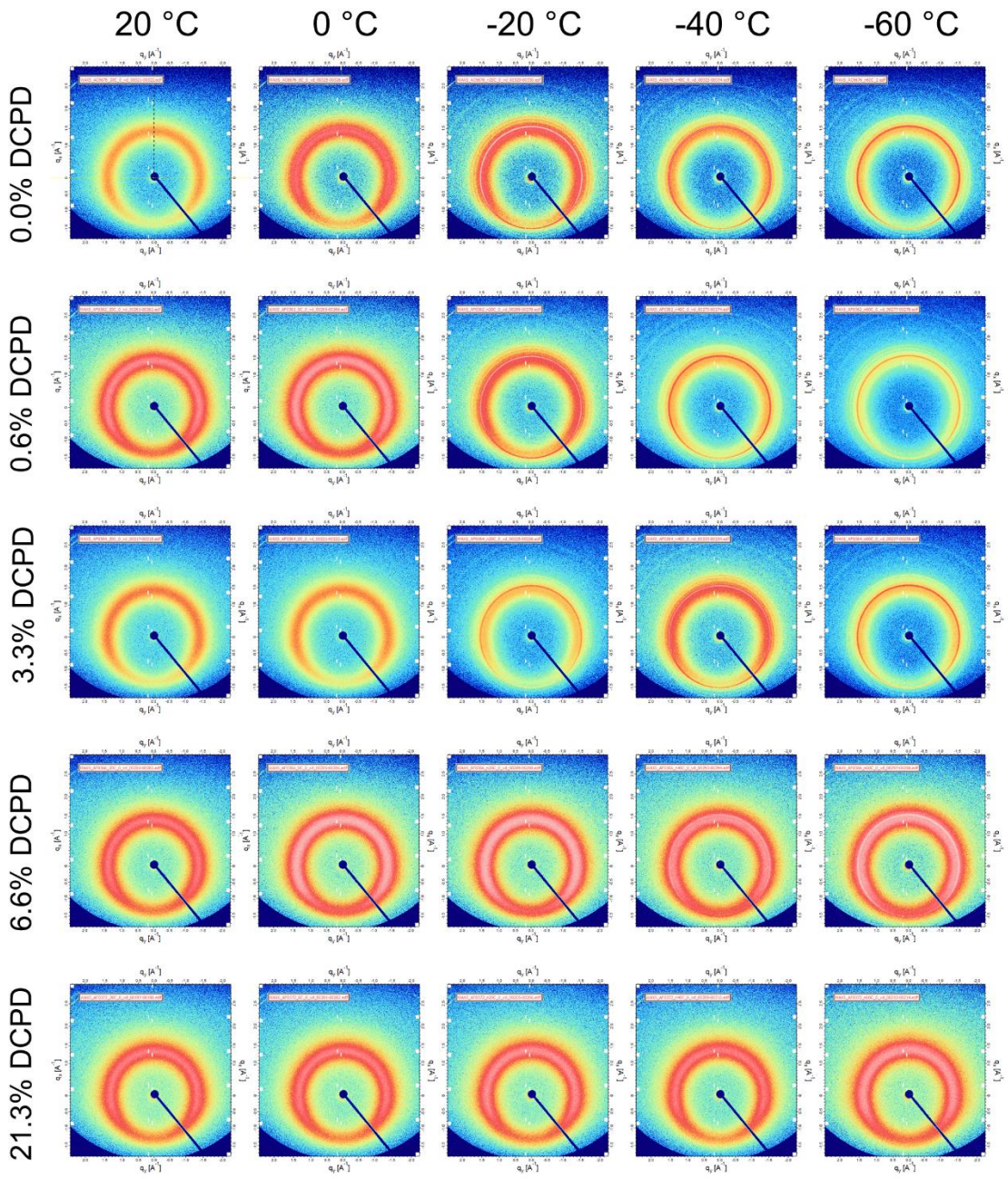

Figure D.4 *2D WAXS images*

Circular integration for 1D plots performed on the top half of data between 0 and 180 degrees to avoid the shadowing effect that reduced scattering intensity towards the bottom of the detector.

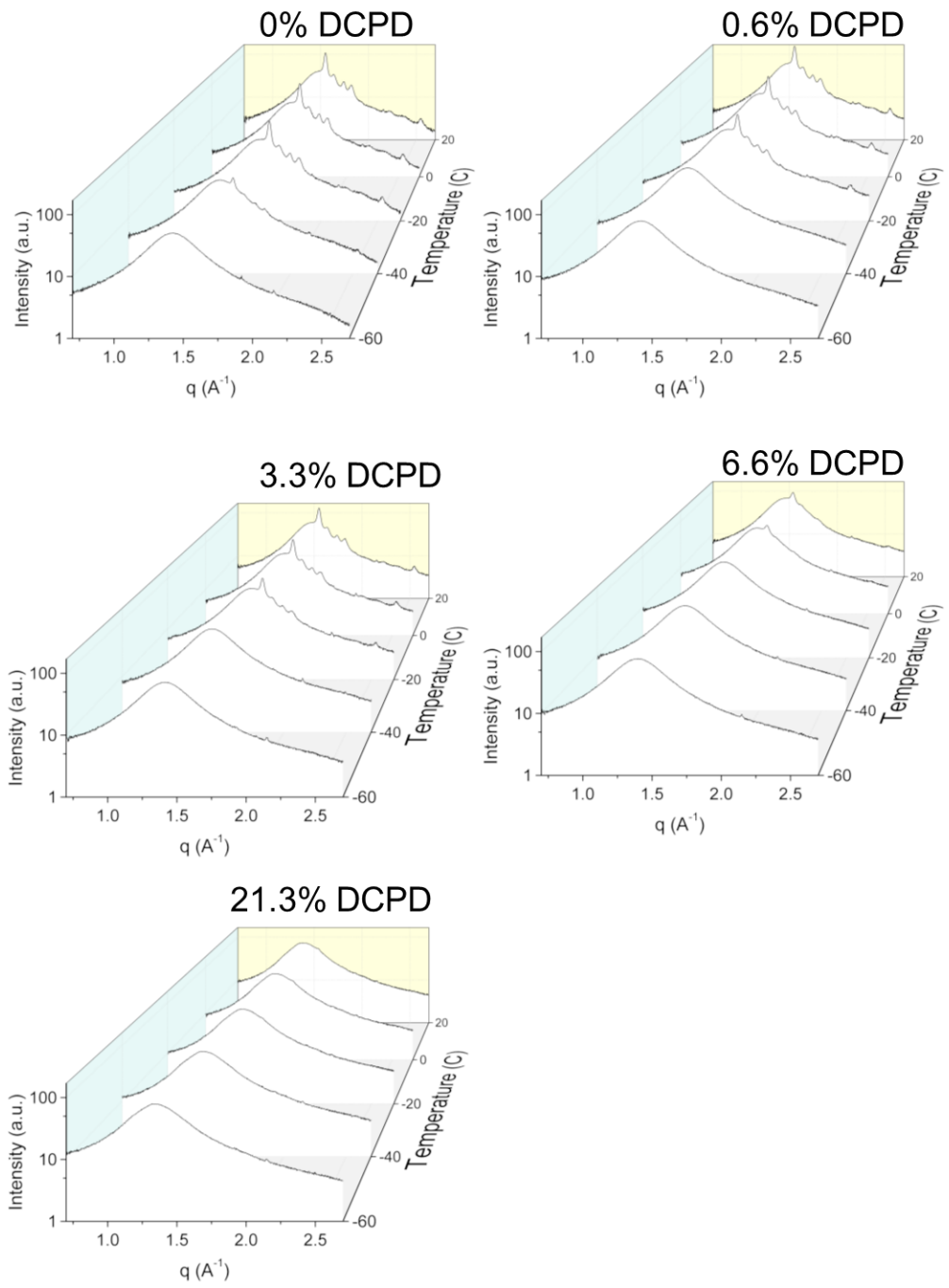

Figure D.5 *WAXS 1D waterfall plots*

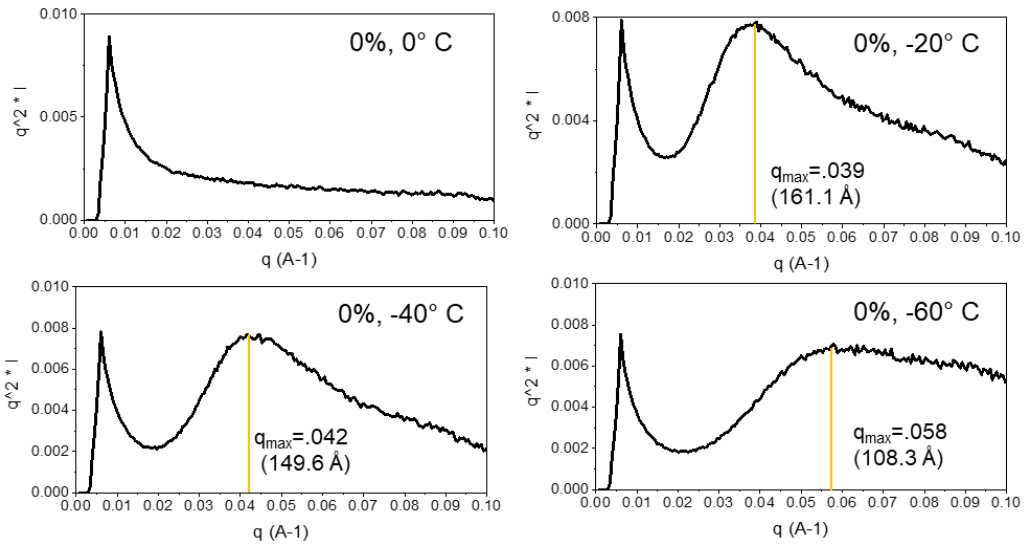

Figure D.6 *Kratkey plots of 0% DCPD polymer at various temperatures*

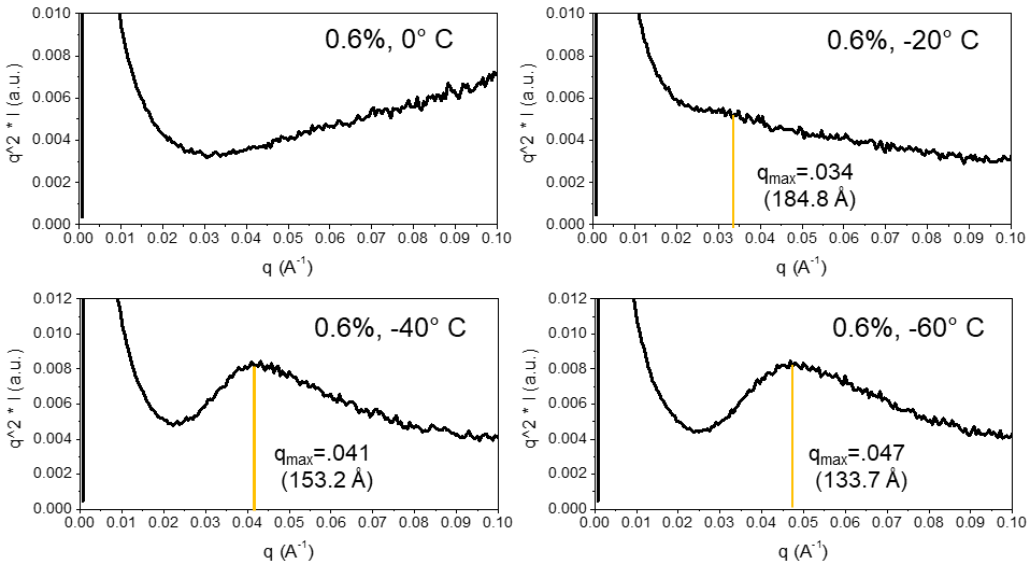

Figure D.7 *Kratkey plots of 0.6% DCPD polymer at various temperatures*

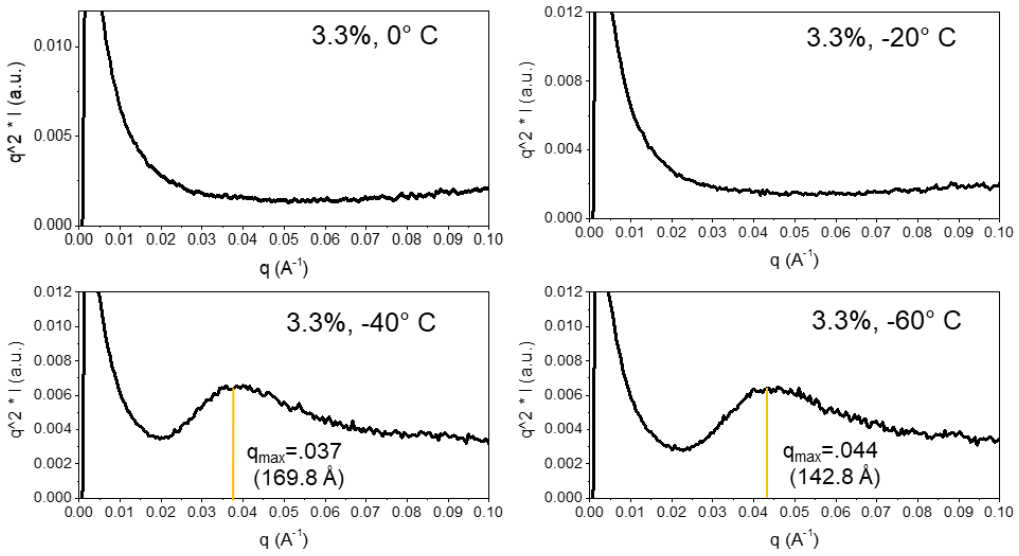

Figure D.8 *Kratkey plots of 3.3% DCPD polymer at various temperatures*

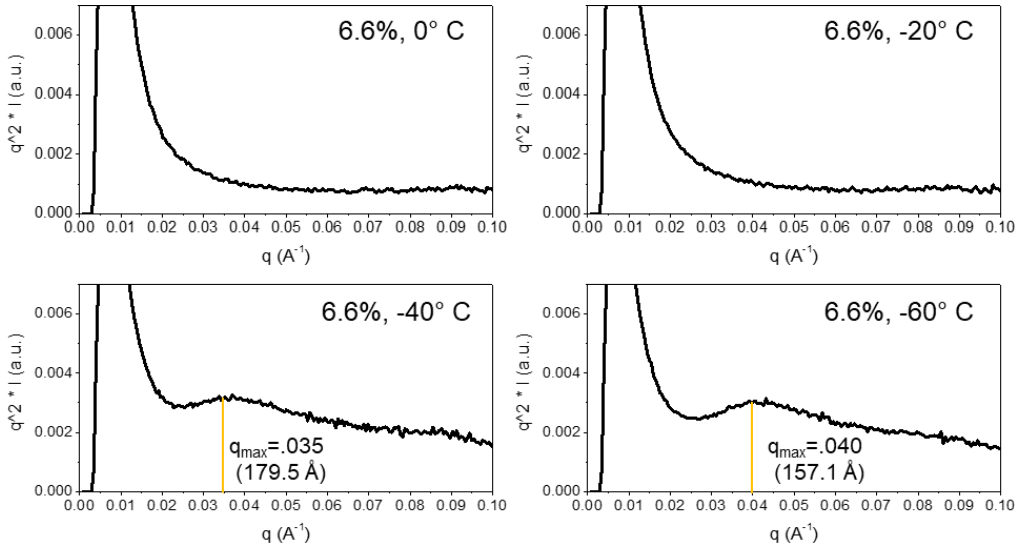

Figure D.9 *Kratkey plots of 6.6% DCPD polymer at various temperatures*

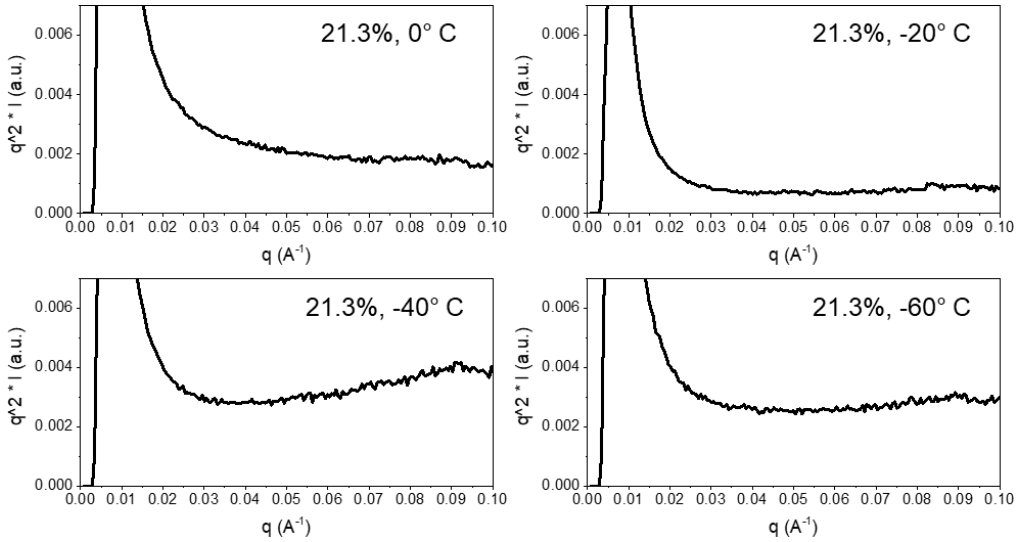

Figure D.10 *Kratkey plots of 21.3% DCPD polymer at various temperatures*

REFERENCES

1. Mayo, F. R. & Walling, C. Copolymerization. **46**, 191–287 (1950).
2. Kenney, J. F. Properties of block versus random copolymers. *Polym. Eng. Sci.* **8**, 216–226 (1968).
3. Moore, J. D. Acrylonitrile-butadiene-styrene (ABS) - a review. *Composites* **4**, 118–130 (1973).
4. Argon, A. S. & Cohen, R. E. Crazing and toughness of block copolymers and blends. *Adv. Polym. Sci.* **91**, 301–351 (1990).
5. Feng, C., Li, Y., Yang, D., Hu, J., Zhang, X. & Huang, X. Well-defined graft copolymers: From controlled synthesis to multipurpose applications. *Chem. Soc. Rev.* **40**, 1282–1295 (2011).
6. Szwarc, M., Levy, M. & Milkovich, R. Polymerization initiated by electron transfer to monomer. A new method of formation of block polymers. *Journal of the American Chemical Society* vol. 78 2656–2657 (1956).
7. Schlick, S. & Levy, M. Block-polymers of styrene and isoprene with variable distribution of monomers along the polymeric chain. Synthesis and properties. *J. Phys. Chem.* **64**, 883–886 (1960).
8. Honeker, C. C. & Thomas, E. L. Impact of morphological orientation in determining mechanical properties in triblock copolymer systems. *Chem. Mater.* **8**, 1702–1714 (1996).
9. Leibler, L. Theory of microphase separation in block copolymers. *Macromolecules* **13**, 1602–1617 (1980).
10. Bates, F. S., Bair, H. E. & Hartney, M. A. Block copolymers near the microphase

separation transition. *Macromolecules* **17**, 2942 (1984).

11. Matsushita, Y. Microphase seperation (of block copolymers). *Encycl. Polym. Nanomater.* 6–11 (2020).
12. Yoshida, H. & Takenaka, M. *Physics of block copolymers from bulk to thin films*. *Directed Self-assembly of Block Copolymers for Nano-manufacturing* (Elsevier Ltd., 2015).
13. Kwak, J., Mishra, A. K., Lee, J., Lee, K. S., Choi, C., Maiti, S., Kim, M. & Kim, J. K. Fabrication of sub-3 nm feature size based on block copolymer self-assembly for next-generation nanolithography. *Macromolecules* **50**, 6813–6818 (2017).
14. Park, M., Harrison, C., Chaikin, P. M., Register, R. A. & Adamson, D. H. Block copolymer lithography: Periodic arrays of ~10^11 holes in 1 square centimeter. *Science (80-.).* **276**, 1401–1404 (1997).
15. Adams, M. L., Lavasanifar, A. & Kwon, G. S. Amphiphilic block copolymers for drug delivery. *J. Pharm. …* **92**, 1343–1355 (2003).
16. Rangou, S., Buhr, K., Filiz, V., Clodt, J. I., Lademann, B., Hahn, J., Jung, A. & Abetz, V. Self-organized isoporous membranes with tailored pore sizes. *J. Memb. Sci.* **451**, 266–275 (2014).
17. Shevate, R., Kumar, M., Cheng, H., Hong, P. Y., Behzad, A. R., Anjum, D. & Peinemann, K. V. Rapid size-based protein discrimination inside hybrid isoporous membranes. *ACS Appl. Mater. Interfaces* **11**, 8507–8516 (2019).
18. Dorin, R. M., Sai, H. & Wiesner, U. Hierarchically porous materials from block copolymers. *Chem. Mater.* **26**, 339–347 (2014).
19. Al Aani, S., Mustafa, T. N. & Hilal, N. Ultrafiltration membranes for wastewater

and water process engineering: A comprehensive statistical review over the past decade. *J. Water Process Eng.* **35**, 101241 (2020).

20. Loeb, S. & Sourirajan, S. Sea water demineralization by means of an osmotic membrane. *Adv. Chem. ACS* **38**, 117–132 (1963).

21. Qiu, X., Yu, H., Karunakaran, M., Pradeep, N., Nunes, S. P. & Peinemann, K. V. Selective separation of similarly sized proteins with tunable nanoporous block copolymer membranes. *ACS Nano* **7**, 768–776 (2013).

22. Zhai, G., Ying, L., Kang, E. T. & Neoh, K. G. Poly(vinylidene fluoride) with grafted 4-vinylpyridine polymer side chains for pH-sensitive microfiltration membranes. *J. Mater. Chem.* **12**, 3508–3515 (2002).

23. Abetz, V. Isoporous block copolymer membranes. *Macromol. Rapid Commun.* **36**, 10–22 (2015).

24. Phillip, W. A., O'neill, B., Rodwogin, M., Hillmyer, M. A. & Cussler, E. L. Self-assembled block copolymer thin films as water filtration membranes. *ACS Appl. Mater. Interfaces* **2**, 847–853 (2010).

25. Yang, H., Wang, Z., Lan, Q. & Wang, Y. Antifouling ultrafiltration membranes by selective swelling of polystyrene/poly(ethylene oxide) block copolymers. *J. Memb. Sci.* **542**, 226–232 (2017).

26. Brüning, K. *In-situ structure characterization of elastomers during deformation and fracture. Springer Theses* (2014).

27. Legge, N. R. Thermoplastic elastomers. *Rubber Chemistry and Technology* vol. 60 (1987).

28. Drobny, J. G. *Introduction*. *Handbook of Thermoplastic Elastomers* vol. 1 (2014).

29. Davey, J. & Schäfer, A. I. Ultrafiltration to supply drinking water in international development: A review of opportunities. in *Appropriate Technologies for Environmental Protection in the Developing World* 151–168 (2009).

30. Malato, S., Fernández-Ibáñez, P., Maldonado, M. I., Blanco, J. & Gernjak, W. Decontamination and disinfection of water by solar photocatalysis: Recent overview and trends. *Catal. Today* **147**, 1–59 (2009).

31. Ahmad, A. & Azam, T. Water purification technologies. in *Bottled and Packaged Water* 83–120 (Elsevier Inc., 2019).

32. Jackson, E. A., Lee, Y. & Hillmyer, M. A. ABAC tetrablock terpolymers for tough nanoporous filtration membranes. *Macromolecules* **46**, 1484–1491 (2013).

33. Yang, S. Y., Ryu, I., Kim, H. Y., Kim, J. K., Jang, S. K. & Russell, T. P. Nanoporous membranes with ultrahigh selectivity and flux for the filtration of viruses. *Adv. Mater.* **18**, 709–712 (2006).

34. Nunes, S. P., Behzad, A. R. & Peinemann, K.-V. Self-assembled block copolymer membranes: From basic research to large-scale manufacturing. *J. Mater. Res.* **28**, 2661–2665 (2013).

35. Jung, A., Filiz, V., Rangou, S., Buhr, K., Merten, P., Hahn, J., Clodt, J., Abetz, C. & Abetz, V. Formation of integral asymmetric membranes of AB diblock and ABC triblock copolymers by phase inversion. *Macromol. Rapid Commun.* **34**, 610–615 (2013).

36. Jackson, E. A. & Hillmyer, M. A. Nanoporous membranes derived from block copolymers: From drug delivery to water filtration. *ACS Nano* **4**, 3548–3553 (2010).

37. Peinemann, K. V., Abetz, V. & Simon, P. F. W. Asymmetric superstructure formed in a block copolymer via phase separation. *Nat. Mater.* **6**, 992–996 (2007).

38. Querelle, S. E., Jackson, E. A., Cussler, E. L. & Hillmyer, M. A. Ultrafiltration membranes with a thin poly(styrene)- b -poly(isoprene) selective layer. *ACS Appl. Mater. Interfaces* **5**, 5044–5050 (2013).

39. Yin, J., Yao, X., Liou, J. Y., Sun, W., Sun, Y. Sen & Wang, Y. Membranes with highly ordered straight nanopores by selective swelling of fast perpendicularly aligned block copolymers. *ACS Nano* **7**, 9961–9974 (2013).

40. Yao, X., Guo, L., Chen, X., Huang, J., Steinhart, M. & Wang, Y. Filtration-based synthesis of micelle-derived composite membranes for high-flux ultrafiltration. *ACS Appl. Mater. Interfaces* **7**, 6974–6981 (2015).

41. Yao, X., Wang, Z., Yang, Z. & Wang, Y. Energy-saving, responsive membranes with sharp selectivity assembled from micellar nanofibers of amphiphilic block copolymers. *J. Mater. Chem. A* **1**, 7100–7110 (2013).

42. Wang, Z., Yao, X. & Wang, Y. Swelling-induced mesoporous block copolymer membranes with intrinsically active surfaces for size-selective separation. *J. Mater. Chem.* **22**, 20542–20548 (2012).

43. Shi, X., Wang, Z. & Wang, Y. Highly permeable nanoporous block copolymer membranes by machine-casting on nonwoven supports: An upscalable route. *J. Memb. Sci.* **533**, 201–209 (2017).

44. Wang, Z. & Wang, Y. Highly Permeable and Robust Responsive Nanoporous Membranes by Selective Swelling of Triblock Terpolymers with a Rubbery Block. *Macromolecules* **49**, 182–191 (2016).

45. Wang, Z., Guo, L. & Wang, Y. Isoporous membranes with gradient porosity by selective swelling of UV-crosslinked block copolymers. *J. Memb. Sci.* **476**, 449–456 (2015).

46. Kellenberger, C. R., Hess, S. C., Schumacher, C. M., Loepfe, M., Nussbaumer, J. E., Grass, R. N. & Stark, W. J. Roll-to-roll preparation of mesoporous membranes by nanoparticle template removal. *Ind. Eng. Chem. Res.* **53**, 9214–9220 (2014).

47. Bucher, T., Filiz, V., Abetz, C. & Abetz, V. Formation of thin, isoporous block copolymer membranes by an upscalable profile roller coating process—a promising way to save block copolymer. *Membranes (Basel).* **8**, 57 (2018).

48. Weller, D. W., Galuska, L., Wang, W., Ehlenburg, D., Hong, K. & Gu, X. Roll-to-Roll Scalable Production of Ordered Microdomains through Nonvolatile Additive Solvent Annealing of Block Copolymers. *Macromolecules* **52**, 5026–5032 (2019).

49. Bang, J., Kim, S. H., Drockenmuller, E., Misner, M. J., Russell, T. P. & Hawker, C. J. Defect-free nanoporous thin films from ABC triblock copolymers. *J. Am. Chem. Soc.* **128**, 7622–7629 (2006).

50. Zhao, H., Gu, W., Kakuchi, R., Sun, Z., Sterner, E., Russell, T. P., Coughlin, E. B. & Theato, P. Photocleavable triblock copolymers featuring an activated ester middle block: ‘one-step’ synthesis and application as locally reactive nanoporous thin films. *ACS Macro Lett.* **2**, 966–969 (2013).

51. Xu, T., Stevens, J., Villa, J. A., Goldbach, J. T., Guarini, K. W., Black, C. T., Hawker, C. J. & Russell, T. P. Block copolymer surface reconstruction: A reversible route to nanoporous films. *Adv. Funct. Mater.* **13**, 698–702 (2003).

52. Wang, Y. & Li, F. An emerging pore-making strategy: Confined swelling-induced

pore generation in block copolymer materials. *Adv. Mater.* **23**, 2134–2148 (2011).

53. Wang, Y., He, C., Xing, W., Li, F., Tong, L., Chen, Z., Liao, X. & Steinhart, M. Nanoporous metal membranes with bicontinuous morphology from recyclable block-copolymer templates. *Adv. Mater.* **22**, 2068–2072 (2010).

54. Nunes, S. P. Block Copolymer Membranes for Aqueous Solution Applications. *Macromolecules* **49**, 2905–2916 (2016).

55. Radjabian, M. & Abetz, V. Advanced porous polymer membranes from self-assembling block copolymers. *Prog. Polym. Sci.* **102**, 101219 (2020).

56. Pispas, S. Double hydrophilic block copolymers of sodium(2-sulfamate-3-carboxylate)isoprene and ethylene oxide. *J. Polym. Sci. Part A Polym. Chem.* **44**, 606–613 (2006).

57. Ntetsikas, K., Alzahrany, Y., Polymeropoulos, G., Bilalis, P., Gnanou, Y. & Hadjichristidis, N. Anionic polymerization of styrene and 1,3-butadiene in the presence of phosphazene superbases. *Polymers (Basel).* **9**, 1–14 (2017).

58. Zhang, S., Ocheje, M. U., Luo, S., Ehlenberg, D., Appleby, B., Weller, D., Zhou, D., Rondeau-Gagné, S. & Gu, X. Probing the viscoelastic property of pseudo free-standing conjugated polymeric thin films. *Macromol. Rapid Commun.* **39**, 1–8 (2018).

59. Darling, S. B. Directing the self-assembly of block copolymers. *Prog. Polym. Sci.* **32**, 1152–1204 (2007).

60. Huinink, H. P., Brokken-Zijp, J. C. M., Van Dijk, M. A. & Sevink, G. J. A. Asymmetric block copolymers confined in a thin film. *J. Chem. Phys.* **112**, 2452–2462 (2000).

61. Suh, K. Y., Kim, Y. S. & Lee, H. H. Parallel and vertical morphologies in block copolymers of cylindrical domain. *J. Chem. Phys.* **108**, 1253–1256 (1998).

62. Ho, R. M., Tseng, W. H., Fan, H. W., Chiang, Y. W., Lin, C. C., Ko, B. T. & Huang, B. H. Solvent-induced microdomain orientation in polystyrene-b-poly(l-lactide) diblock copolymer thin films for nanopatterning. *Polymer (Guildf).* **46**, 9362–9377 (2005).

63. Lin, Z. Q., Kim, D. H., Wu, X. D., Boosahda, L., Stone, D., LaRose, L. & Russell, T. P. A rapid route to arrays of nanostructures in thin films. *Adv. Mater.* **14**, 1373–1376 (2002).

64. Fasolka, M. J. & Mayes, A. M. Block copolymer thin films: Physics and applications. *Annu. Rev. Mater. Sci.* **31**, 323–355 (2001).

65. Mansky, P., Liu, Y., Huang, E., Russell, T. P. & Hawker, C. Controlling polymer-surface interactions with random copolymer brushes. *Science (80-.).* **275**, 1458–1460 (1997).

66. Mansky, P., haikin, P. & Thomas, E. L. Monolayer films of diblock copolymer microdomains for nanolithographic applications. *J. Mater. Sci.* **30**, 1987–1992 (1995).

67. Hanks, P. L., Forschner, C. A. & Lloyd, D. R. Sieve mechanism estimations for microfiltration membranes with elliptical pores. *J. Memb. Sci.* **322**, 91–97 (2008).

68. Bromley, A. J., Holdich, R. G. & Cumming, I. W. Particulate fouling of surface microfilters with slotted and circular pore geometry. *J. Memb. Sci.* **196**, 27–37 (2002).

69. Ullah, A., Starov, V. M., Naeem, M., Holdich, R. G. & Semenov, S. Filtration of

suspensions using slit pore membranes. *Sep. Purif. Technol.* **103**, 180–186 (2013).

70. Fissell, W. H., Dubnisheva, A., Eldridge, A. N., Fleischman, A. J., Zydney, A. L. & Roy, S. High-performance silicon nanopore hemofiltration membranes. *J. Memb. Sci.* **326**, 58–63 (2009).

71. Guo, L., Wang, L. & Wang, Y. Stretched homoporous composite membranes with elliptic nanopores for external-energy-free ultrafiltration. *Chem. Commun.* **52**, 6899–6902 (2016).

72. Kramer, E. J. & Berger, L. L. Fundamental processes of craze growth and fracture. *Adv. Polym. Sci.* **91/92**, (1990).

73. Donald, A. M. & Kramer, E. J. Effect of molecular entanglements on craze microstructure in glassy polymers. *J. Polym. Sci. Part A-2, Polym. Phys.* **20**, 899–909 (1982).

74. Galuska, L. A., McNutt, W. W., Qian, Z., Zhang, S., Weller, D. W., Dhakal, S., King, E. R., Morgan, S. E., Azoulay, J. D., Mei, J. & Gu, X. Impact of backbone rigidity on the thermomechanical properties of semiconducting polymers with conjugation break spacers. *Macromolecules* **53**, 6032–6042 (2020).

75. Forrest, J. A., Dalnoki-Veress, K., Stevens, J. R. & Dutcher, J. R. Effect of free surfaces on the glass transition temperature of thin polymer films. *Phys. Rev. Lett.* **77**, 2002–2005 (1996).

76. Zhang, S., Koizumi, M., Cao, Z., Mao, K. S., Qian, Z., Galuska, L. A., Jin, L. & Gu, X. Directly probing the fracture behavior of ultrathin polymeric films. *ACS Polym. Au* (2021).

77. Guo, Y., Chen, J., Hao, X., Zhang, J., Feng, X. & Zhang, H. A novel process for

preparing expanded Polytetrafluoroethylene(ePTFE) micro-porous membrane through ePTFE/ePTFE co-stretching technique. *J. Mater. Sci.* 2081–2085 (2006).

78. Baker, R. W. *Membrane technology and applications*. *Membrane Technology* (1996). doi:10.1016/s0958-2118(96)90133-0.

79. Sun, W., Wang, Z., Yao, X., Guo, L., Chen, X. & Wang, Y. Surface-active isoporous membranes nondestructively derived from perpendicularly aligned block copolymers for size-selective separation. *J. Memb. Sci.* **466**, 229–237 (2014).

80. Ma, D., Zhou, J., Wang, Z. & Wang, Y. Block copolymer ultrafiltration membranes by spray coating coupled with selective swelling. *J. Memb. Sci.* **598**, 117656 (2020).

81. Mehta, A. & Zydney, A. L. Permeability and selectivity analysis for ultrafiltration membranes. *J. Memb. Sci.* **249**, 245–249 (2005).

82. Jachimska, B., Wasilewska, M. & Adamczyk, Z. Characterization of globular protein solutions by dynamic light scattering, electrophoretic mobility, and viscosity measurements. *Langmuir* **24**, 6867–6872 (2008).

83. Bates, F. S. & Fredrickson, G. H. Block copolymer thermodynamics: Theory and experiment. *Annu. Rev. Phys. Chem.* **41**, 525–557 (1990).

84. Hawker, C. J. & Russell, T. P. Block copolymer lithography: Merging ‘bottom-up’ with ‘top-down’ processes. *MRS Bull.* **30**, 952–966 (2005).

85. Bang, J., Jeong, U., Ryu, D. Y., Russell, T. P. & J Hawker, C. Block copolymer nanolithography: Translation of molecular level control to nanoscale patterns. *Adv. Mater.* **21**, 4769–4792 (2009).

86. Gu, X., Gunkelk, I. & Russell, T. P. Pattern transfer using block copolymers.

Philos. Trans. R. Soc. A Math. Phys. Eng. Sci. **371**, (2013).

87. Bates, C. M. & Bates, F. S. 50th anniversary perspective: Block polymers-pure potential. *Macromolecules* **50**, 3–22 (2017).

88. Gu, X., Shaw, L., Gu, K., Toney, M. F. & Bao, Z. The meniscus-guided deposition of semiconducting polymers. *Nat. Commun.* **9**, (2018).

89. Majewski, P. W. & Yager, K. G. Rapid ordering of block copolymer thin films. *J. Phys. Condens. Matter* **28**, 403002 (2016).

90. Jin, C., Murphy, J. N., Harris, K. D. & Buriak, J. M. Deconvoluting the mechanism of microwave annealing of block copolymer thin films. *ACS Nano* **8**, 3979–3991 (2014).

91. Zhang, X., Murphy, J. N., Wu, N. L. Y., Harris, K. D. & Buriak, J. M. Rapid assembly of nanolines with precisely controlled spacing from binary blends of block copolymers. *Macromolecules* **44**, 9752–9757 (2011).

92. Zhang, X., Harris, K. D., Wu, N. L. Y., Murphy, J. N. & Buriak, J. M. Fast assembly of ordered block copolymer nanostructures through microwave annealing. *ACS Nano* **4**, 7021–7029 (2010).

93. Jin, H. M., Park, D. Y., Jeong, S. J., Lee, G. Y., Kim, J. Y., Mun, J. H., Cha, S. K., Lim, J., Kim, J. S., Kim, K. H., Lee, K. J. & Kim, S. O. Flash light millisecond self-assembly of high χ block copolymers for wafer-scale sub-10 nm nanopatterning. *Adv. Mater.* **29**, 1–7 (2017).

94. Majewski, P. W. & Yager, K. G. Millisecond ordering of block copolymer films via photothermal gradients. *ACS Nano* **9**, 3896–3906 (2015).

95. Jin, H. M., Lee, S. H., Kim, J. Y., Son, S. W., Kim, B. H., Lee, H. K., Mun, J. H.,

Cha, S. K., Kim, J. S., Nealey, P. F., Lee, K. J. & Kim, S. O. Laser writing block copolymer self-assembly on graphene light-absorbing layer. *ACS Nano* **10**, 3435–3442 (2016).

96. Majewski, P. W., Rahman, A., Black, C. T. & Yager, K. G. Arbitrary lattice symmetries via block copolymer nanomeshes. *Nat. Commun.* **6**, (2015).

97. Majewski, P. W. & Yager, K. G. Block copolymer response to photothermal stress fields. *Macromolecules* **48**, 4591–4598 (2015).

98. Kim, S. H., Misner, M. J., Xu, T., Kimura, M. & Russell, T. P. Highly oriented and ordered arrays from block copolymers via solvent evaporation. *Adv. Mater.* **16**, 226–231 (2004).

99. Gotrik, K. W. & Ross, C. A. Solvothermal annealing of block copolymer thin films. *Nano Lett.* **13**, 5117–5122 (2013).

100. Sinturel, C., Vayer, M., Morris, M. & Hillmyer, M. A. Solvent vapor annealing of block polymer thin films. *Macromolecules* **46**, 5399–5415 (2013).

101. Gu, X., Gunkel, I., Hexemer, A., Gu, W. & Russell, T. P. An in situ grazing incidence X-ray scattering study of block copolymer thin films during solvent vapor annealing. *Adv. Mater.* **26**, 273–281 (2014).

102. Cha, S. K., Mun, J. H., Chang, T., Kim, S. Y., Kim, J. Y., Jin, H. M., Lee, J. Y., Shin, J., Kim, K. H. & Kim, S. O. Au-ag core-shell nanoparticle array by block copolymer lithography for synergistic broadband plasmonic properties. *ACS Nano* **9**, 5536–5543 (2015).

103. Jin, C., Olsen, B. C., Luber, E. J. & Buriak, J. M. Nanopatterning via solvent vapor annealing of block copolymer thin films. *Chem. Mater.* **29**, 176–188 (2017).

104. Kao, J., Thorkelsson, K., Bai, P., Zhang, Z., Sun, C. & Xu, T. Rapid fabrication of hierarchically structured supramolecular nanocomposite thin films in one minute. *Nat. Commun.* **5**, 1–8 (2014).

105. Singh, G., Batra, S., Zhang, R., Yuan, H., Yager, K. G., Cakmak, M., Berry, B. & Karim, A. Large-scale roll-to-roll fabrication of vertically oriented block copolymer thin films. *ACS Nano* **7**, 5291–5299 (2013).

106. Quirk, R. P., Kim, J., Kausch, C. & Chun, M. Butyllithium-initiated anionic synthesis of well-defined poly(styrene-block-ethylene oxide) block copolymers with potassium salt additives. *Polym. Int.* **39**, 3–10 (1996).

107. Ilavsky, J. Nika: Software for two-dimensional data reduction. *J. Appl. Crystallogr.* **45**, 324–328 (2012).

108. Gu, X., Yan, H., Kurosawa, T., Schroeder, B. C., Gu, K. L., Zhou, Y., To, J. W. F., Oosterhout, S. D., Savikhin, V., Molina-Lopez, F., Tassone, C. J., Mannsfeld, S. C. B., Wang, C., Toney, M. F. & Bao, Z. Comparison of the morphology development of polymer–fullerene and polymer–polymer solar cells during solution-shearing blade coating. *Adv. Energy Mater.* **6**, 1–12 (2016).

109. Xu, T., Stevens, J., Villa, J. A., Goldbach, J. T., Guarini, K. W., Black, C. T., Hawker, C. J. & Russell, T. P. Block copolymer surface reconstruction: A reversible route to nanoporous films. *Adv. Funct. Mater.* **13**, 698–702 (2003).

110. Gu, X., Liu, Z., Gunkel, I., Chourou, S. T., Hong, S. W., Olynick, D. L. & Russell, T. P. High aspect ratio sub-15 nm Silicon Trenches from Block Copolymer Templates. *Adv. Mater.* **24**, 5688–5694 (2012).

111. Smilgies, D. M., Li, R., Giri, G., Chou, K. W., Diao, Y., Bao, Z. & Amassian, A.

Look fast: Crystallization of conjugated molecules during solution shearing probed in-situ and in real time by X-ray scattering. *Phys. Status Solidi - Rapid Res. Lett.* **7**, 177–179 (2013).

112. Gu, X., Reinspach, J., Worfolk, B. J., Diao, Y., Zhou, Y., Yan, H., Gu, K., Mannsfeld, S., Toney, M. F. & Bao, Z. Compact roll-to-roll coater for in situ X-ray diffraction characterization of organic electronics printing. *ACS Appl. Mater. Interfaces* **8**, 1687–1694 (2016).

113. Cornish, K. Similarities and differences in rubber biochemistry among plant species. *Phytochemistry* **57**, 1123–1134 (2001).

114. James, M., Ngai, K., Graessley, W., Mandelkern, L., Samulski, E., Koenig, J. & Wignall, G. *Physical Properties of Polymers*. (Cambridge University Press, 2004).

115. Amnuaypornsri, S., Sakdapipanich, J., Toki, S., Hsiao, B. S., Ichikawa, N. & Tanaka, Y. Strain-induced crystallization of natural rubber: Effect of proteins and phospholipids. *Rubber Chem. Technol.* **81**, 753–766 (2008).

116. Toki, S., Sics, I., Ran, S., Liu, L., Hsiao, B. S., Murakami, S., Tosaka, M., Kohjiya, S., Poompradub, S., Ikeda, Y. & Tsou, A. H. Strain-induced molecular orientation and crystallization in natural and synthetic rubbers under uniaxial deformation by in-situ synchrotron X-ray study. *Rubber Chem. Technol.* **77**, 317–335 (2004).

117. Natta, G., Dall'Asta, G. & Mazzanti, G. Stereospecific homopolymerization of cyclopentene. *Angew. Chemie Int. Ed. English* **3**, 723–729 (1964).

118. Haas, F., Nuetzel, K., Pampus, G. & Theisen, D. Properties of a trans-1,5-polypentenamer produced by polymerization through ring cleavage of

cyclopentene. *Rubber Chem. Technol.* **43**, 1116–1128 (1970).

119. Kraus, G. & Gruver, J. T. Kinetics of strain-induced crystallization of a trans-polypentenamer. *J. Polym. Sci.* **10**, 2009–2024 (1972).

120. Tucker, H., Minchak, R. J. & Macey, J. H. Structure and properties of polypentenamer. *Polym. Eng. Sci.* **15**, 360–366 (1975).

121. Neary, W. J. & Kennemur, J. G. Polypentenamer renaissance: Challenges and opportunities. *ACS Macro Lett.* **8**, 46–56 (2019).

122. Huneau, B. Strain-induced crystallization of natural rubber: A review of X-Ray diffraction investigations. *Rubber Chem. Technol.* **84**, 425–452 (2011).

123. Murakami, S., Senoo, K., Toki, S. & Kohjiya, S. Structural development of natural rubber during uniaxial stretching by in situ wide angle x-ray diffraction using a synchrotron radiation. *Polymer (Guildf).* **43**, 2117–2120 (2002).

124. Brüning, K., Schneider, K., Roth, S. V. & Heinrich, G. Kinetics of strain-induced crystallization in natural rubber studied by WAXD: Dynamic and impact tensile experiments. *Macromolecules* **45**, 7914–7919 (2012).

125. Toki, S. & Hsiao, B. S. Nature of strain-induced structures in natural and synthetic rubbers under stretching. *Macromolecules* **36**, 5915–5917 (2003).

126. Kitamura, Y., Okada, K., Masunaga, H. & Hikosaka, M. Role of strain rate in the strain-induced crystallization (SIC) of natural and synthetic isoprene rubber. *Polym. J.* **51**, 221–226 (2019).

127. López-Barrón, C. R., Rohde, B., Zabula, A. V., Schaefer, J. J. & Throckmorton, J. A. Molecular orientation and strain-induced crystallization in trans-polypentenamer. *Macromolecules* **53**, 1356–1367 (2020).

128. Roovers, J. Progress in the branched architectural state. *Dendrimers Other Dendritic Polym.* **1**, 67–90 (2002).

129. Edam, R. Comprehensive characterization of branched polymers. *UvA-DARE* (2013).

130. Askadskii, A. A. & Kovriga, O. V. Effect of branching on the physical characteristics of polymers. *Polym. Sci. U.S.S.R.* **33**, 1821–1831 (1991).

131. McKee, M. G., Unal, S., Wilkes, G. L. & Long, T. E. Branched polyesters: Recent advances in synthesis and performance. *Prog. Polym. Sci.* **30**, 507–539 (2005).

132. Dounis, P., James Feast, W. & Kenwright, A. M. Ring-opening metathesis polymerization of monocyclic alkenes using molybdenum and tungsten alkylidene (Schrock-type) initiators and 13C nuclear magnetic resonance studies of the resulting polyalkenamers. *Polymer (Guildf).* **36**, 2787–2796 (1995).

133. Dragutan, V., Demonceau, A., Dragutan, I. & Finkelshtein, E. S. *Green metathesis chemistry: Great challenges in synthesis, catalysis and nanotechnology*. *NATO Science for Peace and Security Series A: Chemistry and Biology* (Springer, 2010).

134. Martinez, N. F., Patil, S., Lozano, J. R. & Garcia, R. Enhanced compositional sensitivity in atomic force microscopy by the excitation of the first two flexural modes. *Appl. Phys. Lett.* **89**, 1–4 (2006).

135. Garcia, R. & Proksch, R. Nanomechanical mapping of soft matter by bimodal force microscopy. *Eur. Polym. J.* **49**, 1897–1906 (2013).

136. Walker, L. M. & Wagner, N. J. SANS analysis of the molecular order in poly(γ-benzyl L-glutamate)/deuterated dimethylformamide (PBLG/d-DMF) under shear and during relaxation. *Macromolecules* **29**, 2298–2301 (1996).

137. Brant, P., Ruff, C. J. & Sun, T. Effect of tacticity on the dilute solution coil dimensions of poly(α-olefin)s. *Macromolecules* **38**, 7181–7183 (2005).

138. Trinkle, S., Walter, P. & Friedrich, C. Van Gurp-Palmen plot II - Classification of long chain branched polymers by their topology. *Rheol. Acta* **41**, 103–113 (2002).

139. Treloar, L. R. G. & Montgomery, D. J. *The physics of rubber elasticity*. *Physics Today* vol. 12 (Oxford University Press, 1959).

140. Guth, E. & James, H. M. Elastic and thermoelastic properties of rubberlike materials. A statistical theory. *Rubber Chem. Technol.* **14**, 596–605 (1941).

141. Boyce, M. C. & Arruda, E. M. Constitutive models of rubber elasticity: A review. *Rubber Chem. Technol.* **73**, 504–523 (2000).

142. Flory, P. J. Thermodynamics of crystallization in high polymers. I. Crystallization induced by stretching. *J. Chem. Phys.* **15**, 397–408 (1947).

143. Mark, J. E. The effect of strain-induced crystallization on the ultimate properties of an elastomeric polymer network. *Polym. Eng. Sci.* **19**, 409–413 (1979).

144. Hamed, G. R., Kim, H. J. & Gent, A. N. Cut growth in vulcanizates of natural rubber, cis-polybutadiene, and a 50/50 blend during single and repeated extension. *Rubber Chem. Technol.* **69**, 807–818 (1996).

145. Maiti, M., Bhattacharya, M. & Bhowmick, A. K. Elastomer nanocomposites. *Rubber Chem. Technol.* **81**, 384–469 (2008).

146. Torre, M., Mulhearn, W. D. & Register, R. A. Ring-opening metathesis copolymerization of cyclopentene above and below Its equilibrium monomer concentration. *Macromol. Chem. Phys.* **219**, 1–8 (2018).

147. Treloar, L. R. G. *The physics of rubber elasticity*. (Oxford University Press, 1975).

148. Mark, J. E. & Erman, B. *Rubberlike elasticity: A molecular primer*. (Cambridge University Press, 2007).

149. Urayama, K., Kawamura, T. & Kohjiya, S. Structure-mechanical property correlations of model siloxane elastomers with controlled network topology. *Polymer (Guildf).* **50**, 347–356 (2009).

150. Sousa Eletterio, H. Polymerization of cyclic olefins. 74–76 (1963).

151. Mackley, M. *Handbook of Polyolefins*. *The Chemical Engineering Journal and the Biochemical Engineering Journal* vol. 60 (1995).

152. Gino Dall'Asta. Preparation and Properties of Polyalkenamers. *Rubber Chemistry and Technology* vol. 47 511–596 (1974).

153. Goodall, B. L., Kroenke, W. J., Minchak, R. J. & Rhodes, L. F. Novel catalysts for the ring-opening metathesis polymerization of norbornene-type monomers. *J. Appl. Polym. Sci.* **47**, 607–617 (1993).

154. Weller, D. W., Halbach, R., Rohde, B., Kang, S., Dwivedi, S., Mehringer, K. D., Shankar, R., Storey, R. F., Morgan, S. E., Zabula, A. V., Gu, X. & López-Barrón, C. R. Long-chain branched polypentenamer rubber: Topological impact on tensile properties, chain dynamics, and strain-induced crystallization. *ACS Appl. Polym. Mater.* **3**, 2498–2506 (2021).

155. Popli, R. & Mandelkern, L. Influence of structural and morphological factors on the mechanical properties of the polyethylenes. *J. Polym. Sci. Part B Polym. Phys.* **25**, 441–483 (1987).

156. Crist, B., Fisher, C. J. & Howard, P. R. Mechanical properties of model polyethylenes: tensile elastic modulus and yield stress. *Macromolecules* **22**, 1709–

1718 (1989).

157. Guth, B. E. Theory of filler reinforcement. *J. Appl. Phys.* **16**, 1945 (2011).

158. Fröhlich, J., Niedermeier, W. & Luginsland, H. D. The effect of filler-filler and filler-elastomer interaction on rubber reinforcement. *Compos. Part A Appl. Sci. Manuf.* **36**, 449–460 (2005).

159. Roland, C. M. Reinforcement of elastomers. *Ref. Modul. Mater. Sci. Mater. Eng.* 1–9 (2016).

160. Spontak, R. J. & Patel, N. P. Thermoplastic elastomers: Fundamentals and applications. *Curr. Opin. Colloid Interface Sci.* **5**, 333–340 (2000).

161. Halbach, R., Dupper, T., Lopex-Barron, C., Kang, S., Mattler, S., Luo, L. & Zabula, A. Synthesis, structural studies and ring-opening metathesis polymerization activity for aluminum aryloxides. *Macromolecules* **submitted**, (2021).

162. Zhang, F., Ilavsky, J., Long, G. G., Quintana, J. P. G., Allen, A. J. & Jemian, P. R. Glassy carbon as an absolute intensity calibration standard for small-angle scattering. *Metall. Mater. Trans. A Phys. Metall. Mater. Sci.* **41**, 1151–1158 (2010).

163. Matsuba, G., Ito, C., Zhao, Y., Inoue, R., Nishida, K. & Kanaya, T. In situ small-angle X-ray and neutron scattering measurements on a blend of deuterated and hydrogenated polyethylenes during uniaxial drawing. *Polym. J.* **45**, 293–299 (2013).

164. Perkins, W. G., Capiati, N. J. & Porter, R. S. The effect of molecular weight on the physical and mechanical properties of ultra-drawn high density polyethylene.

Polym. Eng. Sci. **16**, 200–203 (1976).

165. Chen, Y. Y., Lodge, T. P. & Bates, F. S. Entropically driven phase separation of highly branched/linear polyolefin blends. *J. Polym. Sci. Part B Polym. Phys.* **38**, 2965–2975 (2000).

166. Tanaka, H. Viscoelastic phase separation. *J. Phys. Condens. Matter* **12**, (2000).

167. Kasehagen, L. J., Macosko, C. W., Trowbridge, D. & Magnus, F. Rheology of long-chain randomly branched polybutadiene. *J. Rheol. (N. Y. N. Y).* **40**, 689–709 (1996).

168. Graessley, W. W., Masuda, T., Hoovers, E. L. & Hadjichristidis, N. Rheological properties of linear and branched polyisoprene. *Macromolecules* **9**, 127–141 (1976).

169. Arras, M. M. L., He, B. & Jandt, K. D. High molar mass amphiphilic block copolymer enables alignment and dispersion of unfunctionalized carbon nanotubes in melt-drawn thin-films. *Polymer (Guildf).* **127**, 15–27 (2017).

170. Özdemir, C. & Güner, A. Solubility profiles of poly(ethylene glycol)/solvent systems, I: Qualitative comparison of solubility parameter approaches. *Eur. Polym. J.* **43**, 3068–3093 (2007).